ANL-78-6

MATERIALS TECHNOLOGY FOR COAL-CONVERSION PROCESSES

Twelfth Report,

July–December 1977

ARGONNE NATIONAL LABORATORY, ARGONNE, ILLINOIS

Prepared for the Office of Fossil Energy,
U. S. DEPARTMENT OF ENERGY
under Contract W-31-109-Eng-38

The facilities of Argonne National Laboratory are owned by the United States Government. Under the terms of a contract (W-31-109-Eng-38) between the U. S. Department of Energy, Argonne Universities Association and The University of Chicago, the University employs the staff and operates the Laboratory in accordance with policies and programs formulated, approved and reviewed by the Association.

MEMBERS OF ARGONNE UNIVERSITIES ASSOCIATION

The University of Arizona	Kansas State University	The Ohio State University
Carnegie-Mellon University	The University of Kansas	Ohio University
Case Western Reserve University	Loyola University	The Pennsylvania State University
The University of Chicago	Marquette University	Purdue University
University of Cincinnati	Michigan State University	Saint Louis University
Illinois Institute of Technology	The University of Michigan	Southern Illinois University
University of Illinois	University of Minnesota	The University of Texas at Austin
Indiana University	University of Missouri	Washington University
Iowa State University	Northwestern University	Wayne State University
The University of Iowa	University of Notre Dame	The University of Wisconsin

Printed in the United States of America
Available from
National Technical Information Service
U. S. Department of Commerce
5285 Port Royal Road
Springfield, Virginia 22161
Price: Printed Copy $6.50; Microfiche $3.00

Distribution Category:
Coal Conversion and Utilization—
Coal Gasification (UC-90c)

ANL-78-6

ARGONNE NATIONAL LABORATORY
9700 South Cass Avenue
Argonne, Illinois 60439

MATERIALS TECHNOLOGY FOR COAL-CONVERSION PROCESSES

Twelfth Report,
July—December 1977

W. A. Ellingson
Project Leader

Materials Science Division

Previous reports in this series

ANL-76-7	July—September 1975
ANL-76-22	October—December 1975
ANL-76-60	January—March 1976
ANL-76-111	April—June 1976
ANL-76-125	July—September 1976
ANL-77-5	October—December 1976
ANL-77-41	January—March 1977
ANL-77-62	April—June 1977

TABLE OF CONTENTS

TABLE OF CONTENTS (Contd.)

LIST OF FIGURES

LIST OF FIGURES (Contd.)

LIST OF FIGURES (Contd.)

LIST OF FIGURES (Contd.)

LIST OF TABLES

MATERIALS TECHNOLOGY FOR COAL-CONVERSION PROCESSES: TWELFTH REPORT, JULY-DECEMBER 1977

HIGHLIGHTS

Task A -- Evaluation of Ceramic Refractories for Slagging Gasifiers *(C. R. Kennedy, R. J. Fousek, D. J. Jones, and R. B. Poeppel)*

The preliminary measurements reported for the relative corrosion resistance of the magnesia-chromia refractories tested in Run 5 have been revised. Bricks 19, 20, and 29 exhibited similar resistances to dissolution (6-8 mm for the full-size bricks). Brick 35 was markedly sensitive to a temperature excursion that occurred early in the run. Significant slag penetration (40-50 mm) was observed for all bricks in Run 5. Run 6 was terminated after 305 h due to an over-temperature (estimated at ∿1700 to 1800°C) that caused the insulating refractory wall of the furnace to slump. Brick 38, a fused-cast alumina-chromia spinel, exhibited good corrosion resistance (∿8 mm) under the extreme conditions in Run 6. Run 7 with alumina-chromia and alumina-silica refractories has been completed.

Task C -- Application and Development of Nondestructive Evaluation Methods for Coal-conversion Processes *(W. A. Ellingson, W. J. Shack, and C. A. Youngdahl)*

A second-generation coal-feed-line elbow instrumented for erosive wear detection was installed in the Synthane Pilot Plant, and the first-generation elbow has been examined after exposure to 2.2 x 10^6 kg (∿2400 tons) of crushed coal conveyed. At the Bi-Gas Pilot Plant, repairs of weather damage to the erosive-wear monitoring system on the main coal feed line were made, reliable wall-thickness data were obtained, and a fourth monitoring site was completed.

Acoustic amplitude distribution data were obtained on three continuous firings of mechanically unloaded refractory specimens. The value of the exponent, b, in the power relationship $R(a) = (a/a_o)^{-b}$ has been shown to be consistent with published values for brittle materials. This parameter, with another acoustic-emission (AE) parameter, may be a useful combination for establishing the status of the refractory. Additionally, a relationship appears to exist between the AE data and the linear expansion characteristic of refractory concretes during heating. Also a reasonable agreement exists with the modulus of rupture values, i.e., more total counts correlates with a lower modulus of rupture.

Laboratory and theoretical results suggest that a quantitative acoustic leak-detection system may be possible if the leakage flow is "choked," i.e., the exit velocity from the leakage channel is sonic. This

is likely to be the case for the relatively large leaks of interest in high-pressure lockhopper applications.

Task D -- Corrosion Behavior of Materials in Coal-conversion Processes *(K. Natesan)*

Oxidation-sulfidation studies of Fe-Cr-8 wt % Ni alloys with 4, 12, and 22 wt % Cr were conducted at 750 and 875°C in multicomponent gas mixtures that contained CO, CO_2, CH_4, H_2, and H_2S. The reaction processes resulted in parabolic kinetics. A chromium concentration in the range of 0-12 wt % in the alloy had a negligible effect on the parabolic rate constant; however, the rate constant for the alloy with 22 wt % Cr was significantly lower. For a given sulfur partial pressure, the oxygen partial pressures required for the formation of a continuous oxide layer in an Fe-22 wt % Cr-8 wt % Ni alloy were $\sim 10^2$ and 10^3 times those calculated for Cr-Cr_2O_3 equilibrium at temperatures of 875 and 750°C, respectively.

Task E -- Erosion Behavior of Materials in Coal-conversion Processes *(W. J. Shack and J. Y. Park)*

The erosion testing apparatus built by Solar Corporation under a subcontract from ANL has been received. Substantial repairs and modifications are necessary before the testing program can be undertaken, and these are currently under way.

Task F -- Component Performance and Failure Analysis *(S. Danyluk and G. N. Dragel)*

Failed components from the HYGAS Pilot Plant (welded "Tee" fitting from the char carrier line and tubing from various water lines) and the IGT Steam-Iron Process as well as the Synthane Pilot Plant (shaft and capscrew failures from the water pump and a thermowell) were examined in this quarter.

MATERIALS TECHNOLOGY FOR COAL-CONVERSION PROCESSES: TWELFTH REPORT, JULY-DECEMBER 1977

ABSTRACT

This broad-base materials engineering program, begun in 1974, includes studies on refractory concretes and metallic materials presently being used or intended for use in coal-conversion processes. The program entails studies of erosive wear, nondestructive testing, corrosion, chemical degradation, and failure analysis. Appropriate laboratory and field experiments are integrated such that the results have impact on present pilot-plant and proposed demonstration-plant designs. This report, for the period July-December 1977, presents the technical accomplishments of the program.

INTRODUCTION

The economical conversion of coal into clean and usable fuels will be advanced through the use of durable materials systems. The technical information base required for materials selection in plant design for the operating environments of various coal-conversion processes is extremely limited. Hence, reliable selection and life-time prediction methods of materials under these conditions are not available. This project is designed to provide part of the materials information necessary for successful operation of coal-conversion systems. The present report is the twelfth progress report submitted by ANL to the Division of Coal Conversion/DOE Office of Fossil Energy under project Number 7106, "Materials Technology for Coal Conversion Processes."

The project includes five tasks: (A) evaluation of commercial refractories exposed to coal slag under conditions typical of those encountered in slagging gasification processes; (C) development, evaluation, and application of nondestructive evaluation methods applicable to coal-conversion systems; (D) evaluation of the corrosion behavior of commercial alloys; (E) development of analytical models to predict the erosive-wear behavior of materials used in coal-conversion plants; and (F) analysis of failed coal-conversion plant components.

Task A — Evaluation of Ceramic Refractories for Slagging Gasifiers

(C. R. Kennedy, R. J. Pousek, D. J. Jones, and R. B. Poeppel)

The magnesia-chromia refractories tested in Run 5 have been sectioned, and the microstructural examination is under way. The preliminary results of the relative corrosion resistance of these bricks

reported in the previous quarterly[1] have been revised and are presented in Table I. Posttest photographs of the partial sections of the full-length bricks are shown in Fig. 1. For each brick, the vertical side opposite the ruler was exposed to the slag and two lines of slag attack are evident, corresponding to the two additions of slag made during the test. The slag used was a simulated Montana Rosebud with a base-to-acid (B/A) ratio that was constant at ∿0.6 throughout the entire test; however, a temperature excursion to ∿1600°C (plenum temperature) occurred just before the second slag addition. Thus, the bottom line of attack corresponds to an exposure of ∿70 h to the slag at a plenum temperature of 1500-1600°C, whereas the top line of attack was the result of ∿430 h of exposure at a plenum temperature of 1500°C.

Bricks 19, 20, and 29 exhibited similar resistance to corrosion (as measured by the depth of removal), whereas brick 35 showed a marked sensitivity to the temperature excursion. In addition to the bulk removal of the refractory material, a zone that was obviously penetrated by the slag and a zone in which the microstructure had been altered were evident (Fig. 1). Brick 29 had slightly better resistance to penetration and alteration than the other three. Although the effect of length on the depth of removal and obvious penetration was small for bricks 19, 20, and 29, the 1/2-length brick 35 performed distinctly better than the full- or 3/4-length brick of the same composition. Also, the depth of alteration decreased as the length decreased for all bricks tested. To determine whether the alterations in the microstructures were a result of penetration by slag, samples were core drilled and examined with the SEM using x-ray dispersive analysis. The relative intensities of the Mg, Al, Si, Cr, and Fe peaks were compared in the slag, slag-refractory interface, obviously penetrated refractory, and the zone of microstructural alteration ∿40 mm from the hot face. Evidence for slag penetration was most clear-cut in brick 35, somewhat less so in bricks 19 and 20, and inconclusive in brick 29.

Run 6 was designed to evaluate the corrosion resistance of three fused-cast and one high-density sintered brick to the simulated Montana Rosebud slag (B/A = 0.6). A detailed chemical analysis of the slag as a function of time during the test will be presented in the next report. The compositions of the bricks tested are listed in Table II. Refractory number 2 is an electrically fused-cast alpha-alumina within a beta-alumina matrix. Refractory number 38 is an electrically fused-cast solid solution of alumina-chromia within a complex chromia-alumina spinel matrix. Refractory number 39 is a fused-cast magnesia-chromia composition, whereas number 40 is of similar composition but is a direct-bonded, high-density brick.

The furnace plenum temperature and the temperatures 38.1 mm (1.5 in.) from the hot face of the 3/4-length bricks are shown in Fig. 2. At 305 h into the run, a temperature excursion, which occurred as a result of a thermocouple failure, caused the bubble-Al_2O_3 insulating

wall to slump (Fig. 3), and the test had to be terminated due to the resultant hot spot on the shell. It is estimated that the plenum temperature reached ∿1700 to 1800°C overnight during the excursion. Temperature profiles for the bricks on August 18, 1977 are shown in Fig. 4. The relative resistance to corrosion of the refractories in Run 6 is presented in Table II, and cut sections of the brick are shown in Fig. 5. Only one line of attack is evident upon examination, despite the fact that slag was added three times during the test. Indications are the corrosion that resulted during the temperature excursion was sufficient to eradicate the lower lines of attack. A comparison of the attack on refractory 39 in this test with the attack on refractories 19 and 20 (similar composition and structure) in test 5 indicates that the conditions in Run 6 were quite severe. In light of this severity, the corrosion resistance of the fused-cast alumina-chromia brick (number 38) may be quite good at 1500°C, and therefore it will be retested in the future. As evident from the posttest photographs, bricks 2 and 39 contained substantial porosity, which provided an easy avenue for penetration and corrosion. This type of porosity may be atypical for brick 2 and therefore other bricks of this composition will be sectioned and examined. Also evident are numerous thermal-shock cracks that occurred in the three fused-cast refractories (numbers 2, 38, and 39). No such cracks were found in the sintered brick (number 40). Microstructural evaluation of these bricks is in progress.

Test Run 7 with alumina-chromia and alumina-silica refractories was completed as of October 20, 1977, and the results will be presented in the next report. Test Run 8 will evaluate four ramming mixes; two alumina-silica, an alumina-chromia, and a chromia-alumina.

TABLE I. Relative Resistance of Refractories Exposed to Slag Attack in Run 5

Composition	No.	Attack Line	Maximum Depth of Removal,[a] mm			Depth of Obvious Penetration,[a] mm			Depth of Microstructural Alteration,[a] mm		
			Full-length	3/4-length	1/2-length	Full-length	3/4-length	1/2-length	Full-length	3/4-length	1/2-length
$MgO(53)-Cr_2O_3(20)-Al_2O_3(17)-Fe_2O_3(8)-SiO_2(2)-CaO(1)$	19	Top	7	8	7	9	9	9	52	41	37
		Bottom	7	7	8	9	11	11	47	35	33
$MgO(59)-Cr_2O_3(19)-Al_2O_3(13)-Fe_2O_3(7)-SiO_2(1.5)-CaO(0.5)$	20	Top	7	6	5	11	7	6	52	41	31
		Bottom	8	6	4	10	8	9	43	36	31
$MgO(63)-Cr_2O_3(18)-Al_2O_3(5)-Fe_2O_3(12)-SiO_2(1)-CaO(1)$	29	Top	7	8	5	8	9	6	44	32	28
		Bottom	6	7	6	7	9	6	36	28	26
$MgO(60)-Cr_2O_3(15.5)-Al_2O_3(15)-Fe_2O_3(7)-SiO_2(1.5)-CaO(1)$	35	Top	9	9	4	9	10	5	53	37	32
		Bottom	16	17	9	20	21	14	53	39	32

[a]Measured from the original hot face.

TABLE II. Relative Resistance of Refractories Exposed to Slag Attack in Run 6 (Preliminary Results for 3/4-length Bricks)

Composition	No.	Depth of Removal,[a] mm	Depth of Penetration,[a] mm
Al_2O_3(99.3)-Na_2O(0.4)-CaO(0.1)	2	18[b]	50[b]
Al_2O_3(60.4)-Cr_2O_3(27.3)-Fe_2O_3(4.2)-SiO_2(1.8)	38	8	10
MgO(56.5)-Cr_2O_3(20.0)-FeO(10.5)-Al_2O_3(8.0)-SiO_2(2.5)-TiO_2(1.5)-CaO(0.5)	39	28	32
MgO(60.8)-Cr_2O_3(18.6)-Fe_2O_3(11.0)-Al_2O_3(6.6)-CaO(1.9)-SiO_2(1.1)	40	27	32

[a]Measured from the original hot face.

[b]Measurement possibly atypical.

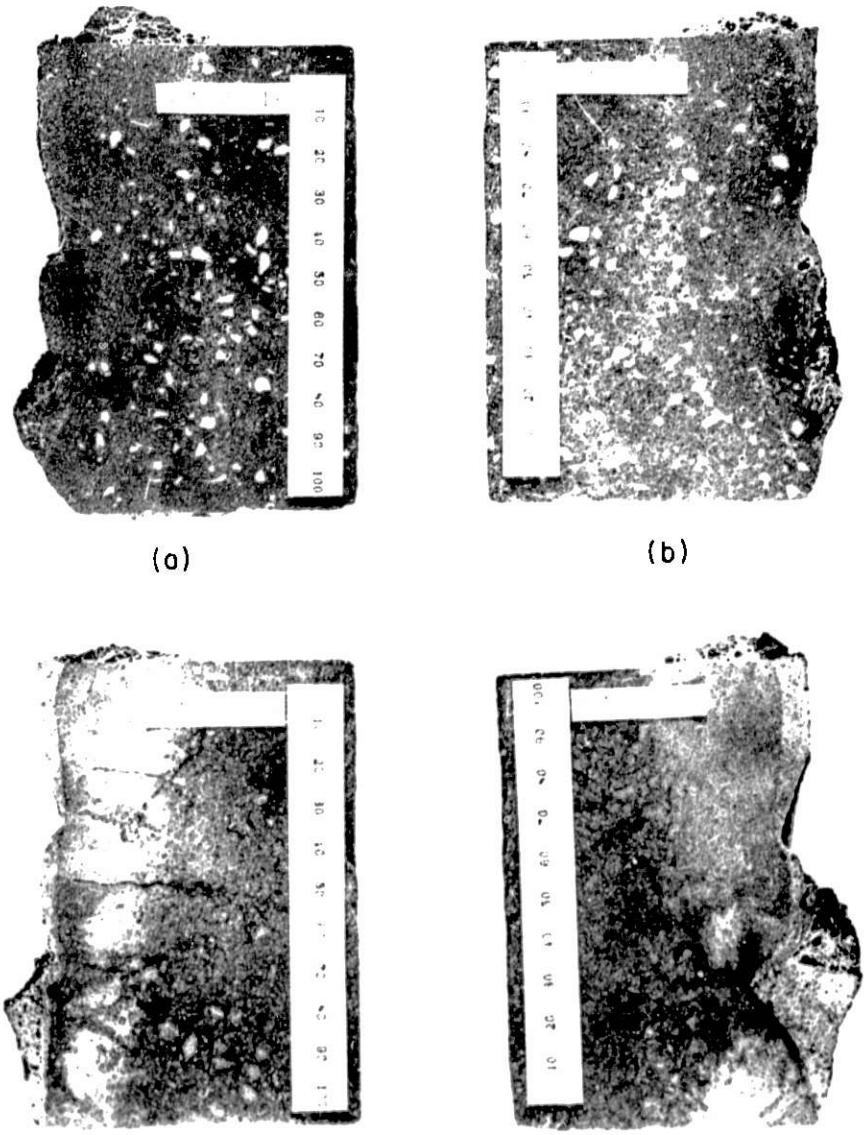

Fig. 1. Cut Sections of Refractories Exposed to Slag Attack In Run 5. (a) Number 19, (b) number 20, (c) number 29, and (d) number 35. Note that the vertical face opposite the ruler was exposed to the slag. Also note that two lines of attack are present which correspond to the two levels of slag during the test. ANL Neg. No. 306-73-94.

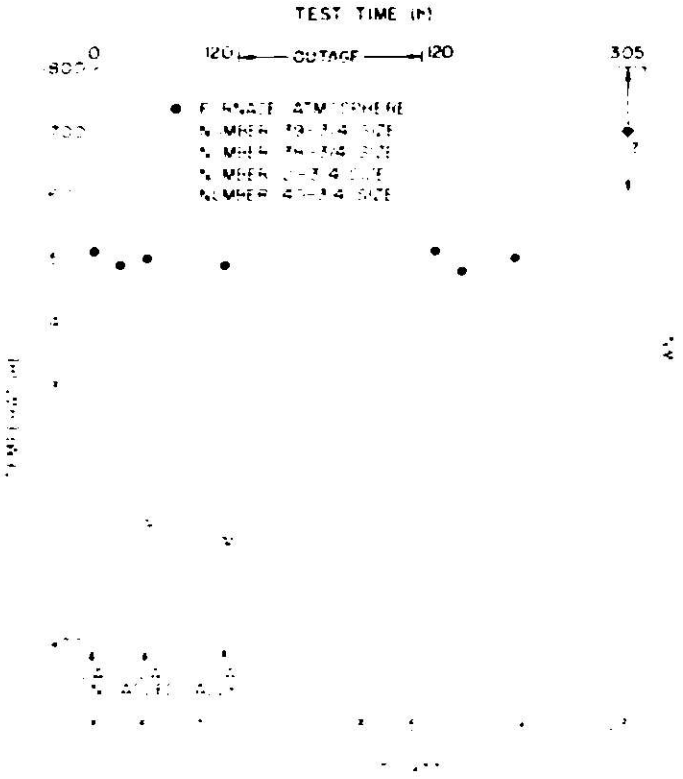

Fig. 2. Furnace Plenum Temperature and Brick Temperatures 38.1 mm (1.5 in.) from the Hot Face of Each Composition during Test Run 6. ANL Neg. No. 120-75-45.

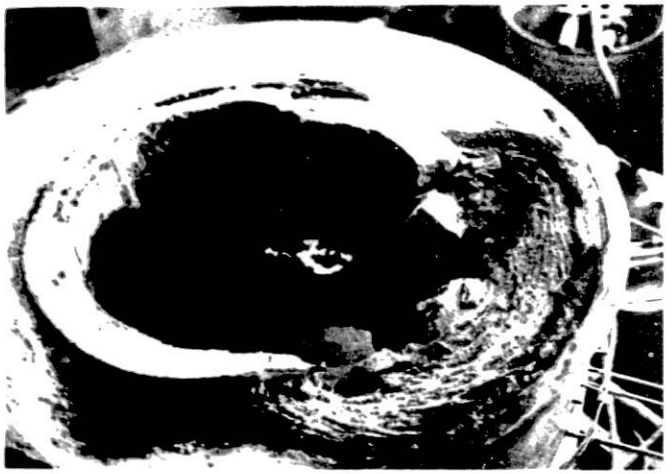

Fig. 3. Bottom Section of the Furnace after Shutdown in Run 6 Showing the Slumped Insulating Refractory Wall.

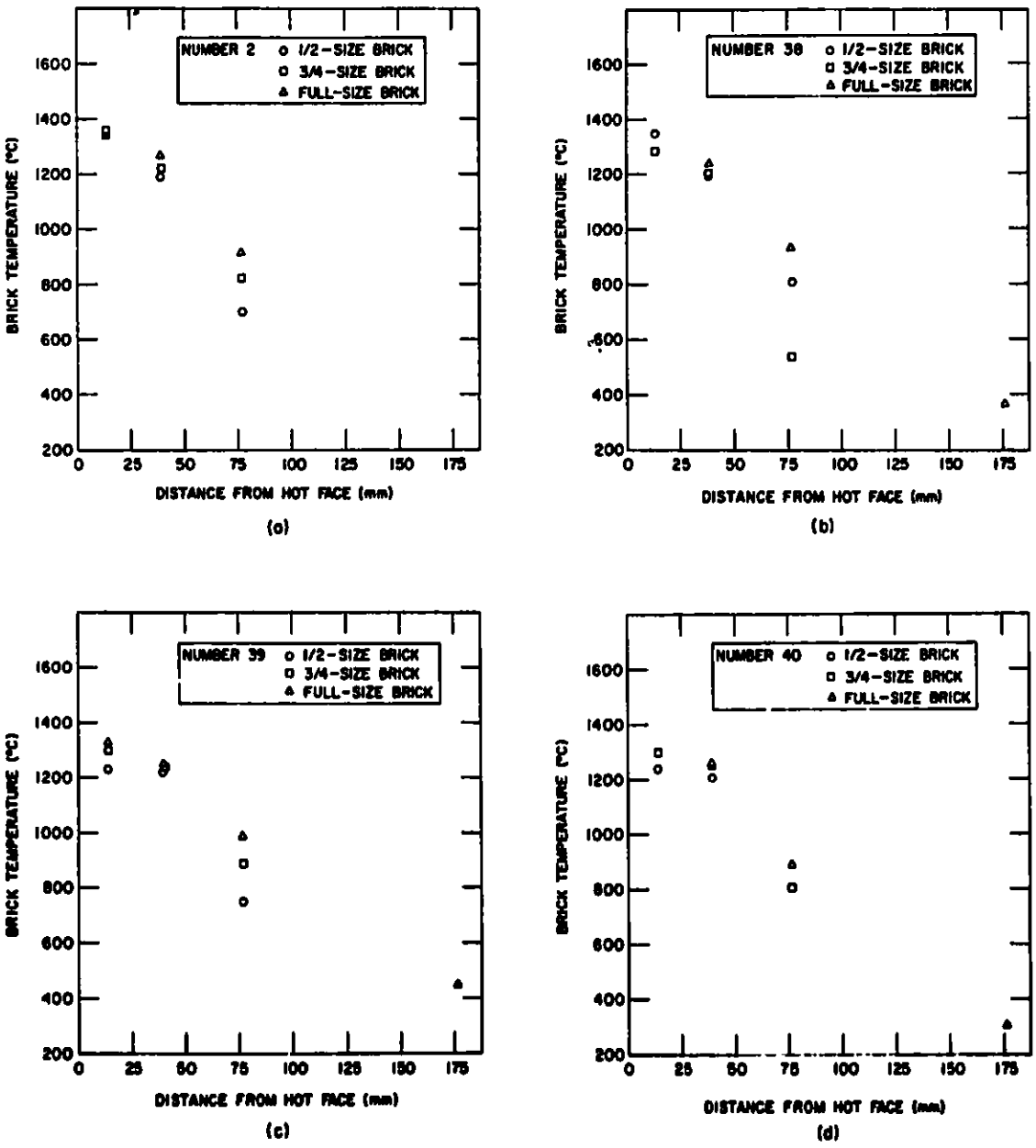

Fig. 4. Temperatures in Bricks during Test Run 6 at Four Locations in Full-length Bricks and Three Locations in 3/4- and 1/2-length Bricks. (Lack of data points indicates thermocouple failed.) (a) Fused-cast alumina (number 2), (b) fused-cast alumina-chromia (number 38), (c) fused-cast magnesia-chromia (number 39), and (d) compacted direct-bonded magnesia-chromia (number 40). ANL Neg. No. 306-78-40.

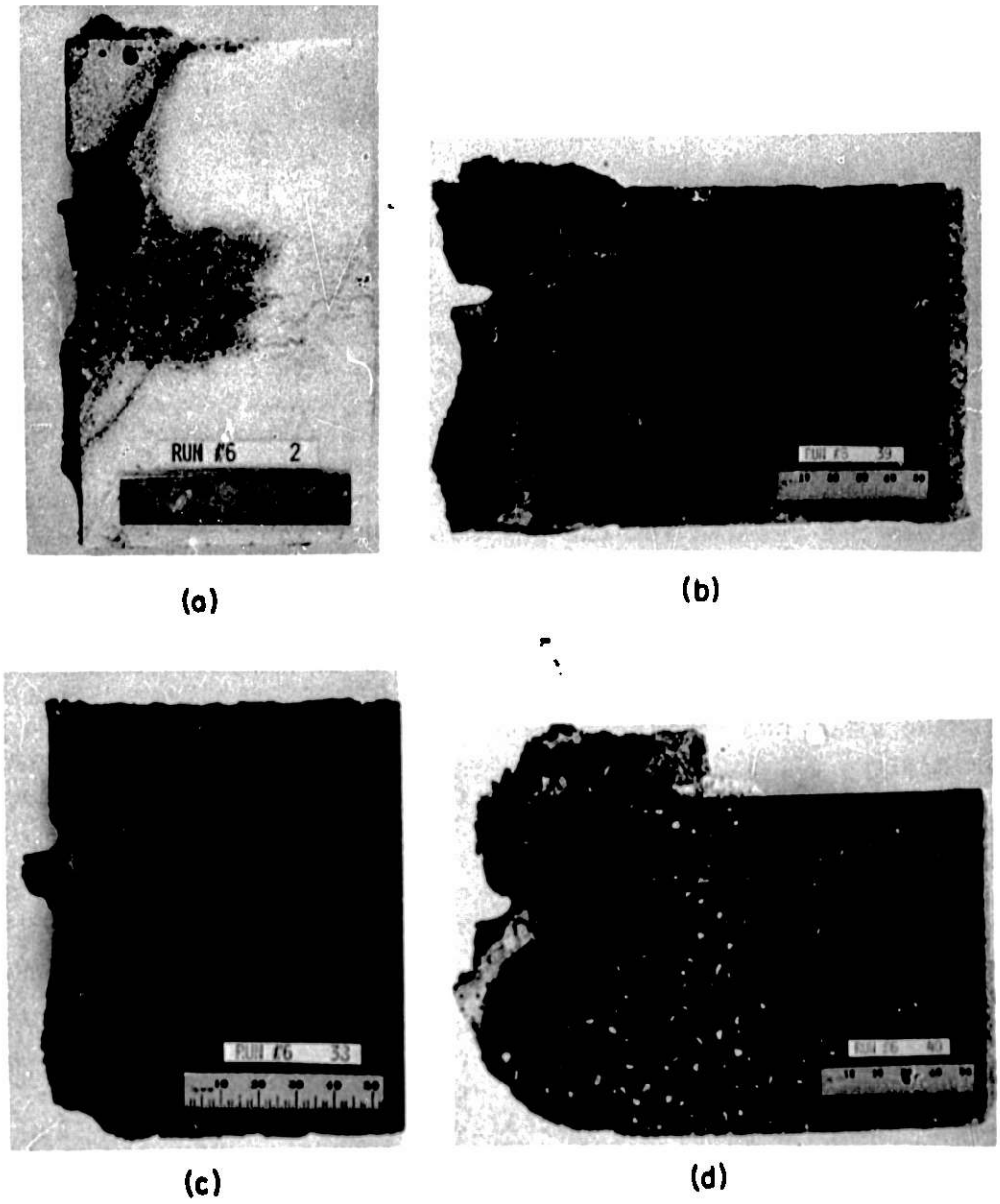

Fig. 5. Cut Sections of the Refractories Exposed to Slag Attack in Run 6. (a) Number 2, (b) number 39, (c) number 38, and (d) number 40. Note that the vertical face on the left-hand side of each brick was exposed to the slag. ANL Neg. No. 306-78-93.

Task B -- Evaluation of Ceramic Coatings for Coal-conversion Plants
This task has been discontinued.

Task C -- Application and Development of Nondestructive Evaluation Methods for Coal-conversion Processes *(W. A. Ellingson, W. J. Shack, and C. A. Youngdahl)*

1. Erosive-wear Detection and Monitoring

a. Metallic Transfer Lines

(1) Ultrasonic Studies. Development of nondestructive, in-situ, erosive-wear detection methods for metallic lines and fittings has continued with emphasis on the improvement of the field installations at the Synthane and Bi-Gas coal-gasification pilot plants. Changes in wall thickness are being monitored with experimental ultrasonic pulse-echo instrumentation on elevated-temperature components subject to erosion by two-phase (particulate-gas) mixtures in the process piping of the plants. The measurement systems have been discussed in previous quarterly reports.[2-6] The present report describes the progress and results for the period July-December 1977.

A second-generation elbow, instrumented with improved acoustic waveguides and a simpler design for in-situ monitoring of erosive wall thinning, was installed at the Synthane Plant in the main coal-feed line during a planned shutdown in August. The 90°, 0.3-m (12-in.) centerline radius elbow was fabricated from 1-in., Schedule 80, Type 304 stainless steel pipe. Eleven newly designed waveguides were attached at 9° intervals along the extrados of the elbow by means of an electric-arc stud-welding process. A 7.5-MHz, 3/8-in. diameter ultrasonic transducer was acoustically and mechanically coupled to the end of each waveguide by epoxy cement. The bond was reinforced by a bolted clamp on each waveguide. The instrumented elbow is shown in Fig. 6.

The transducers were connected to the plant-located scanner, which is connected via ∿61 m (200 ft) of RG58 coaxial cable to the pulser-receiver in the control room. Base-line measurements of the distances between the waveguide shoulders and the inner surface of the pipe were then obtained ultrasonically.

Subsequently, the measurement survey was repeated on 11/29/77, after initial operation of the elbow in the plant system. The exposure[7] of the second-generation elbow was reported by DOE personnel at the plant: 32.7×10^3 kg (36 tons) of Illinois No. 6 coal were transferred at a temperature of ∿120°C and a nominal gas flow rate of 6.1 m/s (20 ft/s); temperatures of ∿290°C were measured when only gas (CO_2 and steam) was present in the line. (Increased temperature and flow rate and the addition of oxygen in the line are contemplated for future process experiments.) The ultrasonic survey indicated losses in wall thickness of only 0-0.13 mm. An error limit of 0.13 mm is considered applicable to each field measurement of shoulder-to-inner surface distance.

The scanner control system was modified for more reliable operation at subfreezing temperatures. Decoder and inverter integrated circuits, conforming to military specifications, were substituted for the commercial units in the scanner.

The first-generation elbow was removed from the plant in August after being in service for 14 months and was returned to ANL for examination. The outer protective sleeve of the elbow assembly was removed, and the waveguides were sheared free at the relatively brittle braze joint at the outer surface of the inner pipe. The 1-in. Schedule 80, Type 304 stainless steel inner pipe was then sectioned and inspected.

Surface undulations were observed on the bore extrados; the waves were, in general, oriented laterally to the flow direction as shown in Fig. 7. The inner surface of the pipe in the affected region was observed to be polished smooth, whereas the opposite side of the inner surface appeared to be similar to the as-received condition. Conditions of erosive exposure[7] are given in Table III.

Dimensional data for the pipe sections are given in Tables III and IV, and Figs. 8 and 9 display a portion of these data in graphic form. Lack of perfect initial concentricity (before bending) should be considered when interpreting the results. Data from the relatively unaffected, straight sections at the ends of the elbow provide a basis for interpolation of this error at various positions along the bend. In addition, the 90° bending of the pipe to form the elbow would be expected to cause a change in wall thickness of 0.1-0.15 mm (4-6 mils) at the inner and outer curves of the bend.

When the foregoing corrections are made to the data of Fig. 3, the net amount of wall thinning at the extrados was ∿0.076-0.76 mm (3-30 mils) from 9 to 90° into the bend; the wall-thickness minima were distributed along the bend, as described above and in Table IV and Fig. 9.

Mechanisms that may be responsible for the results, particularly the surface waves, are being considered. One aspect of the consideration is the possible influence of the fabrication history of the elbow on the posttest condition of the inner surface of the elbow.

The installation of ten Type 304 stainless steel waveguides on the stainless steel blocked tee in the off-gas line[6] at the Bi-Gas pilot-plant was completed. The appearance of the tee with waveguides in place is shown in Fig. 10. (Thermal insulation on the tee was subsequently replaced.)

Waveguides were welded in place by means of an electric-arc stud-welding technique by Nelson Stud Welding Service of Lorain, Ohio, using welding parameters optimized in cooperation with ANL.

Preliminary work at ANL had demonstrated the suitability of a modified design for the fabrication of stainless steel waveguides. To reduce signal attenuation, the distance from the transducer face to the waveguide shoulder was changed from the 171 mm (6-3/4 in.) length used previously for carbon steel waveguides to 111 mm (4-3/8 in.). It was also determined that stainless steel waveguides fabricated from as-received (wrought) stock were superior to those made of solution-annealed material, with respect to signal-attenuation properties.

A set of 7.5-MHz ultrasonic transducers has been installed on the waveguides at the stainless steel tee. The transducers were epoxy coupled and mechanically clamped to the waveguides. The use of 7.5 MHz, rather than the previous 5-MHz frequency, is in accordance with current activity at ANL where interpretation of the roughness of acoustic reflecting surfaces by echo analysis is being developed.

The 5-MHz transducers at the carbon steel elbows and blocked tee in the main coal-feed line were removed to repair the acoustic couplant bonds to the waveguides. The Eastman 910 couplant material, which had been degraded by weather, was removed, and an epoxy couplant was employed as the transducers were replaced. The bonds were additionally protected with Scotchkote and a fillet of RTV silicone rubber. A small sheet-metal roof was also provided for the tee.

The erosive-wear measurement system was prepared for reliable operation at subfreezing temperatures. The console was insulated and provided with a thermostatic heater. The remote scanner modules were equipped with decoder and inverter integrated circuits that conform to military specifications (-55°C) as a replacement for the commercial (0°C) units formerly used.

Selected areas on the outer surface of the main coal-feed-line tee were cleaned and used for direct-contact ultrasonic wall-thickness determinations. The measurements were made on September 8, 1977 at sites located 25.4 mm (1 in.) outboard of each waveguide site. The results are given in Table V. Figure 11 shows the location of the waveguides on this tee. The wall-thickness values may be compared with the nominal starting values for the tee and connecting line. The wall thickness of the tee is greater than the nominal starting value; however, ASTM specifications allow up to 12.5% variation from nominal values.

Waveguide shoulder-to-pipe outer surface distances were determined ultrasonically with the pulser-receiver, which was temporarily taken to the roof location of the subject tee for the previously mentioned direct wall-contact measurements. Measurements of shoulder-to-inner surface distances were made with the calibration transducer coupled sequentially to the waveguides. The direct wall-contact results were then subtracted out to yield the shoulder-to-outer surface distances. An attempt was made in November to verify the latter results by making molded rubber impressions of these sites and measuring the distances directly from the impressions. Agreement was within 0.7 mm (27 mils). The check may be

repeated when the weather is more conducive to making accurate replicas with the dental impression material.

These ultrasonically determined shoulder-to-outer surface data were subtracted from shoulder-to-inner surface data taken from the Bi-Gas 8th floor console on September 9, 1977, after the assembly at the main coal-feed-line blocked tee had been repaired. These differences are shown in Table V for comparison with the direct-contact wall-thickness results. The two sets of data are generally consistent when the 25.4 mm (1-in.) offset of sites is considered. The consistency shows that the measurements are essentially independent of the effects of specific transducers and long lengths of cable.

The overall erosive-wear data from the main coal-feed-line tee between September 10, 1976, and September 11, 1977 indicate, after temperature corrections, a net reduction of 1.32-1.83 mm (52-72 mils) in the tee wall and ∿1.07 mm (∿42 mils) in the downstream pipe wall. The data, however, show interim trends that are not given credance at this time. The direct readings of 9/77 provide a firmer basis of confidence. It is concluded that the actual erosive wear was relatively small and that back-extrapolation of subsequent wear should be used to confirm or modify the previous wear results.

At the upper elbow of the main coal-feed line, data for sites 17, 19, and 20 showed overall erosive wear of 0.051, 0.127, and 0.178 mm (2, 5, and 7 mils), respectively, as of 9/9/77. The waveguide attachment at site 16 is unsatisfactory; and site 18, a "noisy" site, displayed an anomalous, apparent gain. Again, interim trends were exhibited that are subject to clarification as additional wear is experienced. At the lower elbow, no erosive wear was detected during the same period. Direct wall readings will be obtained along this zone to correlate to waveguide data.

The erosive conditions[8] applicable to the main coal-feed line were reported to ANL by Phillips Petroleum personnel at the Bi-Gas Plant. In summary, the cumulative coal throughput was as follows: 9/9/77, 237 x 10^3 kg (261 tons); 10/14/77, 373 x 10^3 kg (411 tons); and 12/1/77, 564 x 10^3 kg (622 tons). The maximum feed rate of the Rosebud coal was 2.72 x 10^3 kg/h (3 tons/h). Typical gas-flow velocity was 12 m/s (40 ft/s) with line temperatures near 290°C (554°F) and a pressure of ∿5.5 MPa (800 psi). Gas composition was primarily H_2, CO, CO_2, H_2O, and N_2 with 4-8% CH_4 and <1% H_2S.

Results of ultrasonic surveys at the Bi-Gas Plant on 10/14 and 12/1/77 will be discussed in the next quarterly report.

The participation of plant personnel in assembly and repair activities at the Bi-Gas and Synthane plants is gratefully acknowledged.

TABLE III. Synthane Instrumented Elbow I Posttest[a] Wall-thickness Data. Mechanically Determined at Sites Unaffected by Braze Residues. Units, Mils (1 mil = 0.001 in. = 0.0254 mm)

Bend Angle, deg	Angular Position on Pipe Cross Section, deg							
	0 (Extrados)	45	90	135	180	225	270	315
Inlet	183	179	179	182	188	187	185	184
0	178	175	182	181	187	185	190	-
2	177	-	178	-	188	-	188	-
9	171	170	185	186	188	187	182	-
23	150	182	183	185	185	165	164	-
24	160	-	182	183	185	185	165	164
27	164	169	181	186	185	184	185	-
36	163	-	-	-	-	-	-	-
41	149	-	178	189	187	185	181	174
42	160	-	-	178	186	184	184	176
44	170	-	-	-	-	-	-	-
51	167	-	-	186	186	186	170	169
63	168	168	176	181	186	186	185	-
71	163	-	-	-	-	-	-	-
72	172	169	182	184	189	181	178	-
86	171	169	182	-	189	-	173	-
89	166	181	184	-	184	-	182	-
Outlet	178	174	174	182	184	180	181	180

[a]Erosive exposure history:[7] cumulative coal (Montana Rosebud) throughput $2.18 \times 10^6 \pm 136 \times 10^3$ kg (2400 ±150 tons) dry weight; coal feed rate 1.36×10^3–2.72×10^3 kg/h [1.5–3 tons/h (2 to 2-1/2 typ.)]; gas flow velocity ~6 m/s (~20 ft/s), temperature ~80°C, and pressure 4.1 MPa (600 psi); conveying gas CO_2.

TABLE IV. Synthane Instrumented Elbow I Posttest[a] Bore Undulation Data. Depth of wave trough below adjacent wave crests in mils (1 Mil = 0.001 in. = 0.0254 mm)

Bend Angle, deg	Angular Position on Pipe Cross Section, deg					
	330	345	0	15	20	27-30
4.1	-	-	-	-	-	2.2
4.7	-	-	1.6	-	-	-
6.9	-	-	-	-	-	0.2
10.0	-	-	0.6	-	-	-
10.2	-	-	-	-	-	4.8
12.6	-	-	6.6	-	-	-
14.2	-	-	-	-	-	15.2
14.4	-	-	4.1	-	-	-
17.1	-	-	3.0	-	-	-
18.4	-	-	-	-	-	10.8
19.2	-	-	3.2	-	-	-
22.2	-	-	7.1	-	-	-
22.5	-	8.0	-	-	-	-
23.8	-	-	3.5	-	-	-
24.6	-	2.0	2.9	-	-	-
27.4	-	5.9	-	-	-	-
27.5	-	-	2.7	-	-	-
31.0	-	-	7.5	-	-	-
31.1	-	6.2	-	-	-	-
33.2	-	4.3	-	-	-	-
33.3	-	-	(-2)	-	-	-
36.3	-	5.9	-	-	-	-
36.7	-	-	11.5	-	-	-
40.3	-	25.3	-	-	-	-
40.7	-	-	27.8	-	-	-
43.6	-	-	3.3	-	-	-
45.5	-	8.2	-	-	-	-
46.2	-	-	5.4	-	-	-
48.6	-	-	-	8.6	-	-
49.3	9.2	14.6	14.4	-	-	8.6
51.3	-	1.7	-	-	-	-
51.5	1.7	-	-	-	-	-
52.5	-	-	-	-	-	7.5
52.7	-	-	7.8	-	-	-
52.9	-	-	-	8.3	-	-
53.4	-	7.6	-	-	-	-
53.6	5.1	-	-	-	-	-
55.6	-	-	3.0	-	-	-
55.7	-	1.3	-	-	-	-
56.0	3.8	-	-	-	-	-
56.6	-	-	-	-	-	8.4
56.7	-	-	-	6.6	-	-
57.9	-	-	7.3	-	-	-
58.2	-	7.8	-	-	-	-

TABLE IV (Contd.)

Bend Angle, deg	Angular Position on Pipe Cross Section, deg					
	330	345	0	15	20	27-30
58.5	7.5	-	-	-	-	-
58.9	-	-	-	3.8	-	-
59.0	-	-	-	-	-	4.3
60.3	0.9	-	-	-	-	-
61.4	-	4.0	-	-	-	-
61.5	-	-	7.0	6.9	-	-
61.8	-	-	-	-	-	2.2
63.4	2.9	-	-	-	-	-
64.1	-	5.4	4.0	0.7	-	-
64.6	-	-	-	-	-	1.7
66.8	-	-	3.4	-	1.4	-
70.3	-	-	9.5	-	12.1	-
73.1	-	-	4.0	-	-	-
74.0	-	-	-	-	3.3	-
75.6	-	-	7.1	-	-	-
77.0	-	-	0.6	-	-	-
78.9	-	-	4.1	-	8.3	-
81.1	-	-	12.9	-	-	-
81.2	-	-	-	-	(-0.9)	-
86.5	-	6.1	10.8	-	-	-

[a]Erosive exposure conditions are listed in the footnote to Table III.

Note: Undulation profile data were obtained from molded plastic impressions by means of an optical comparator. All data have been corrected for bend curvature. Bore surface finish posttest (all bend angles): extrados 5 μin., intrados 40 μin.

Table V. Wall Thickness Data from Bi-Gas Main Coal Feed Line Blocked Tee, September 9, 1977

Waveguide Number	Component	Wall Thickness from Console Sh-BW Minus UT Sh-FW[a]		Wall Thickness Direct Contact UT, 25.4mm(1 in.) Offset[a]	
		mm	mils	mm.	mils
21	Pipe	20.04	789	20.04	789
22	Pipe	19.81	780	19.89	783
23	Pipe	20.17	794	20.14	793
24	Pipe			20.12	792
25	Pipe (Weld)			24.4	962
26	Tee	32.8	1291	32.7	1287
27	Tee	32.8	1290	32.6	1285
28	Tee	33.3	1310	33.2	1307
29	Tee	32.6	1285	33.0	1298
30	Tee	33.4	1316	33.3	1311
31	Tee (Weld)	34.0	1338	34.0	1337

[a]Sh-BW: distance from waveguide shoulder to ultrasonically reflecting back wall (inner surface of pipe wall). Sh-FW: distance from waveguide shoulder to front wall (outer surface of pipe). Additional explanation in text.

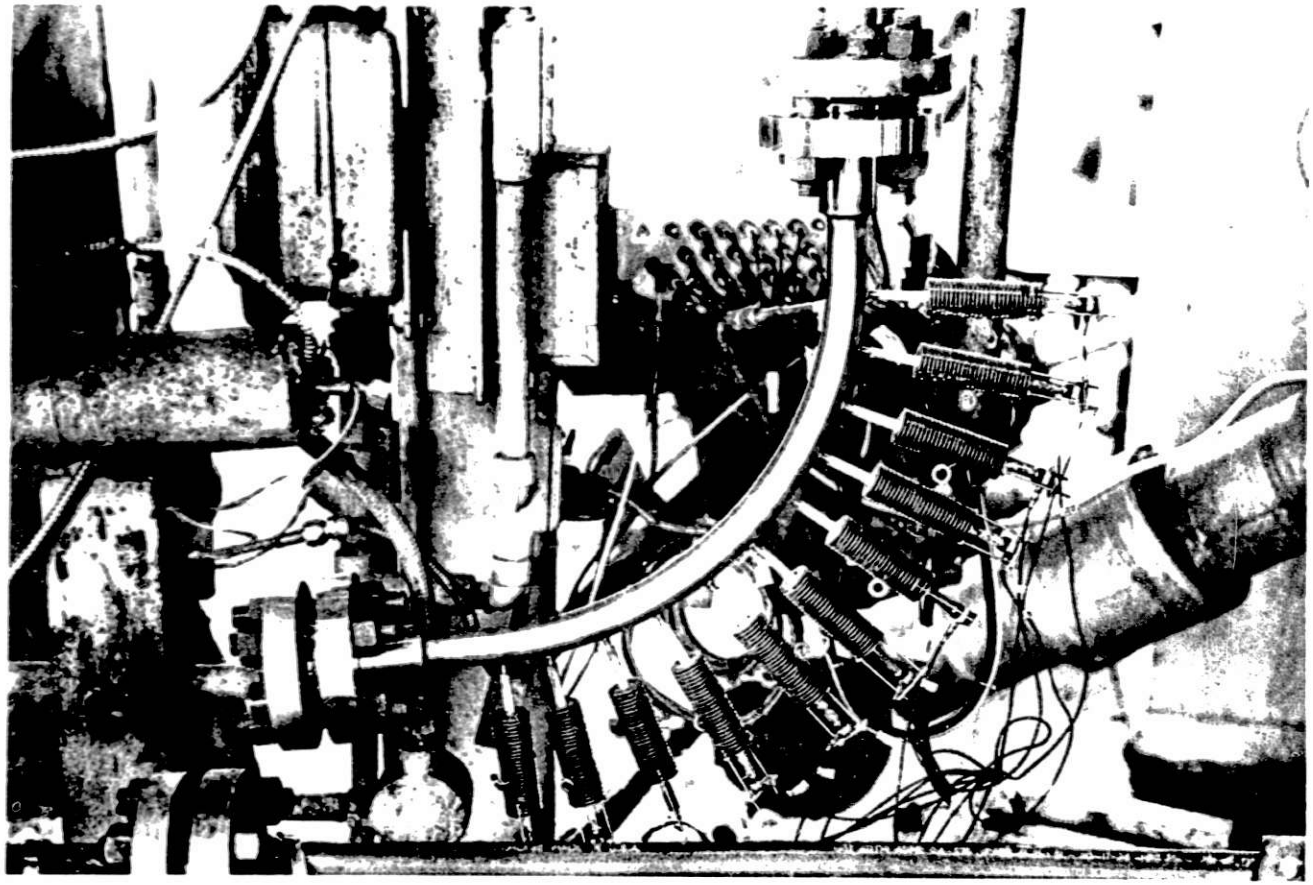

Fig. 6. New Coal-feed-line Elbow during Installation at the Synthane Pilot Plant, Instrumented for Erosion Monitoring.

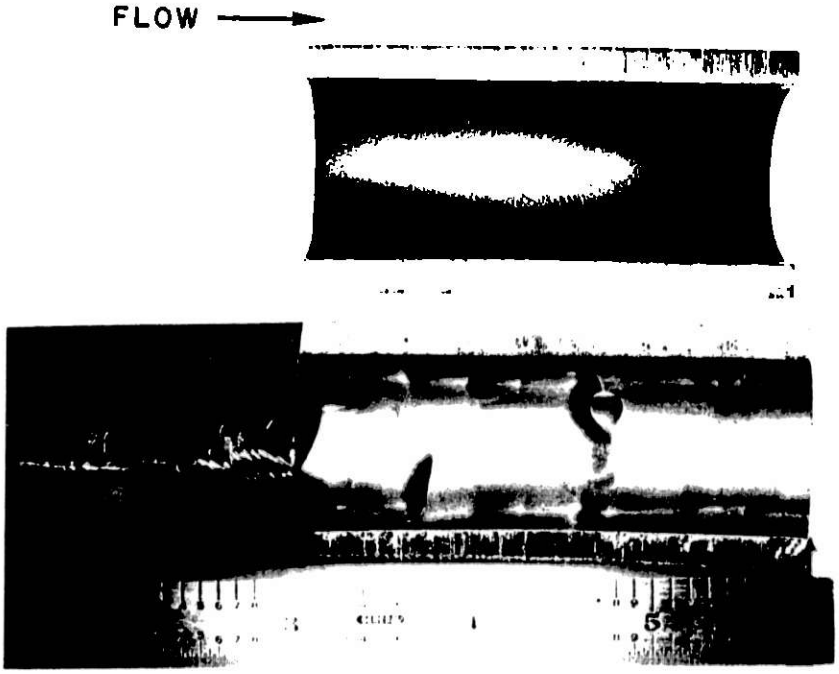

Fig. 7. Metal Surface Undulations in Extrados Region of Bore in Section of Synthane Instrumented Elbow I. ANL Neg. No. 306-78-115.

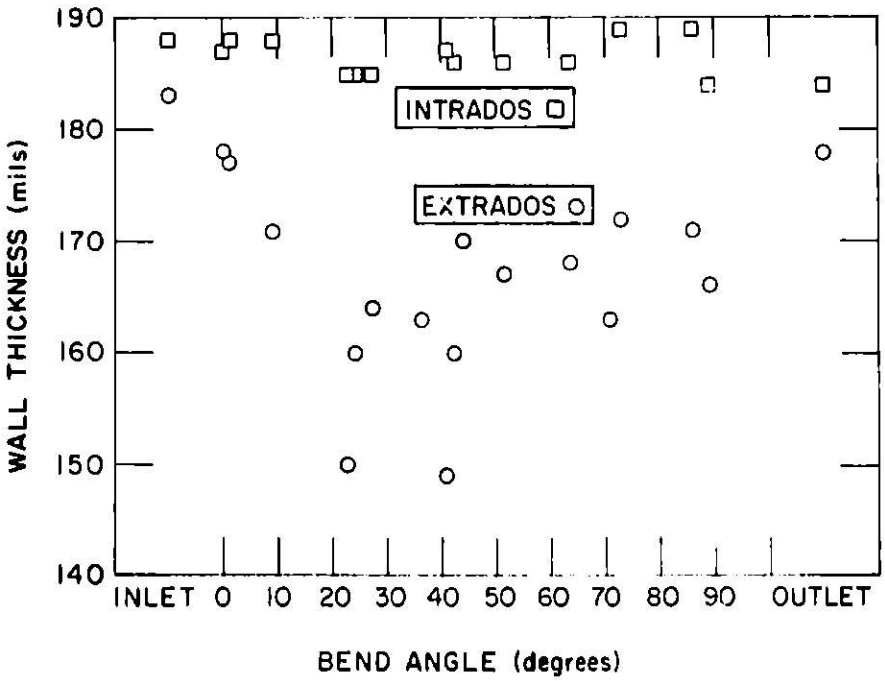

Fig. 8. Synthane Main Coal-feed-line Elbow I Posttest Wall Thickness vs Bend Angle. ANL Neg. No. 306-78-116.

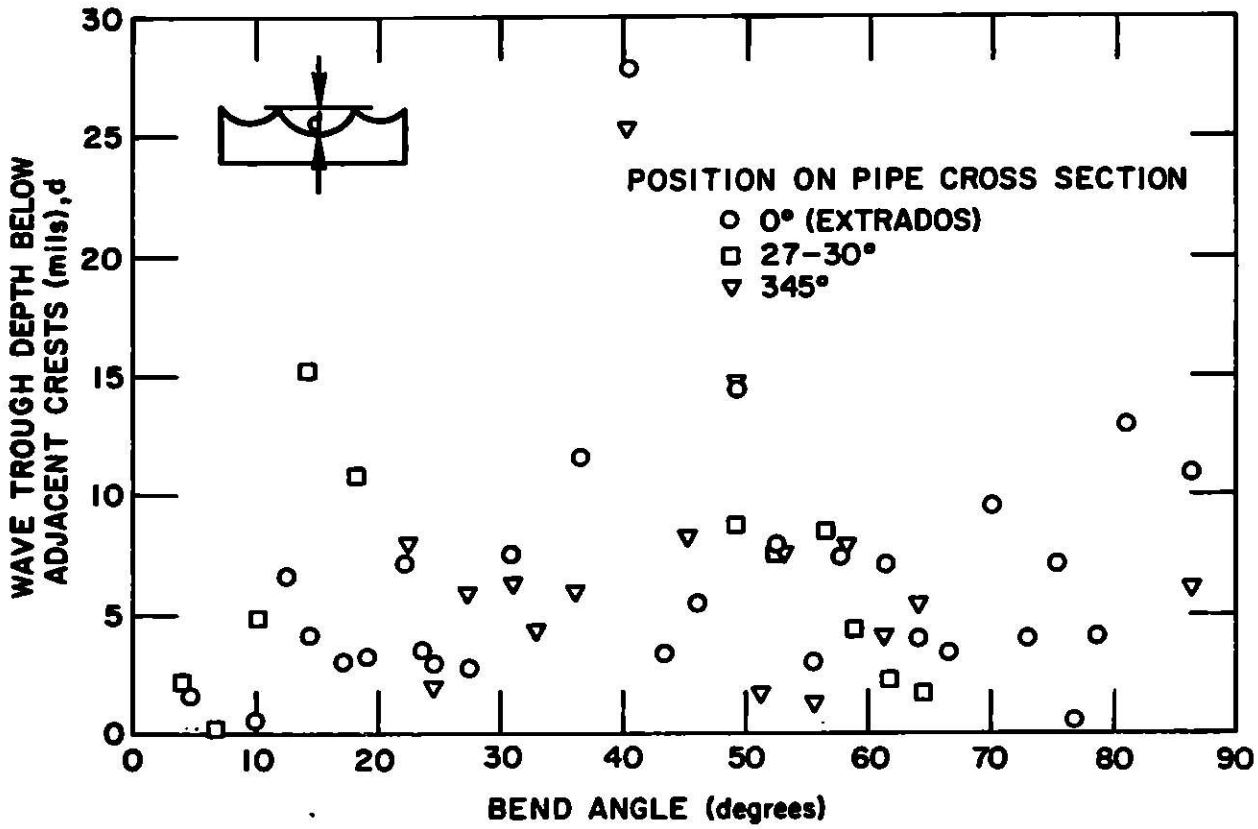

Fig. 9. Synthane Instrumented Elbow I Posttest Bore Undulation Data from Table IV. ANL Neg. No. 306-78-117.

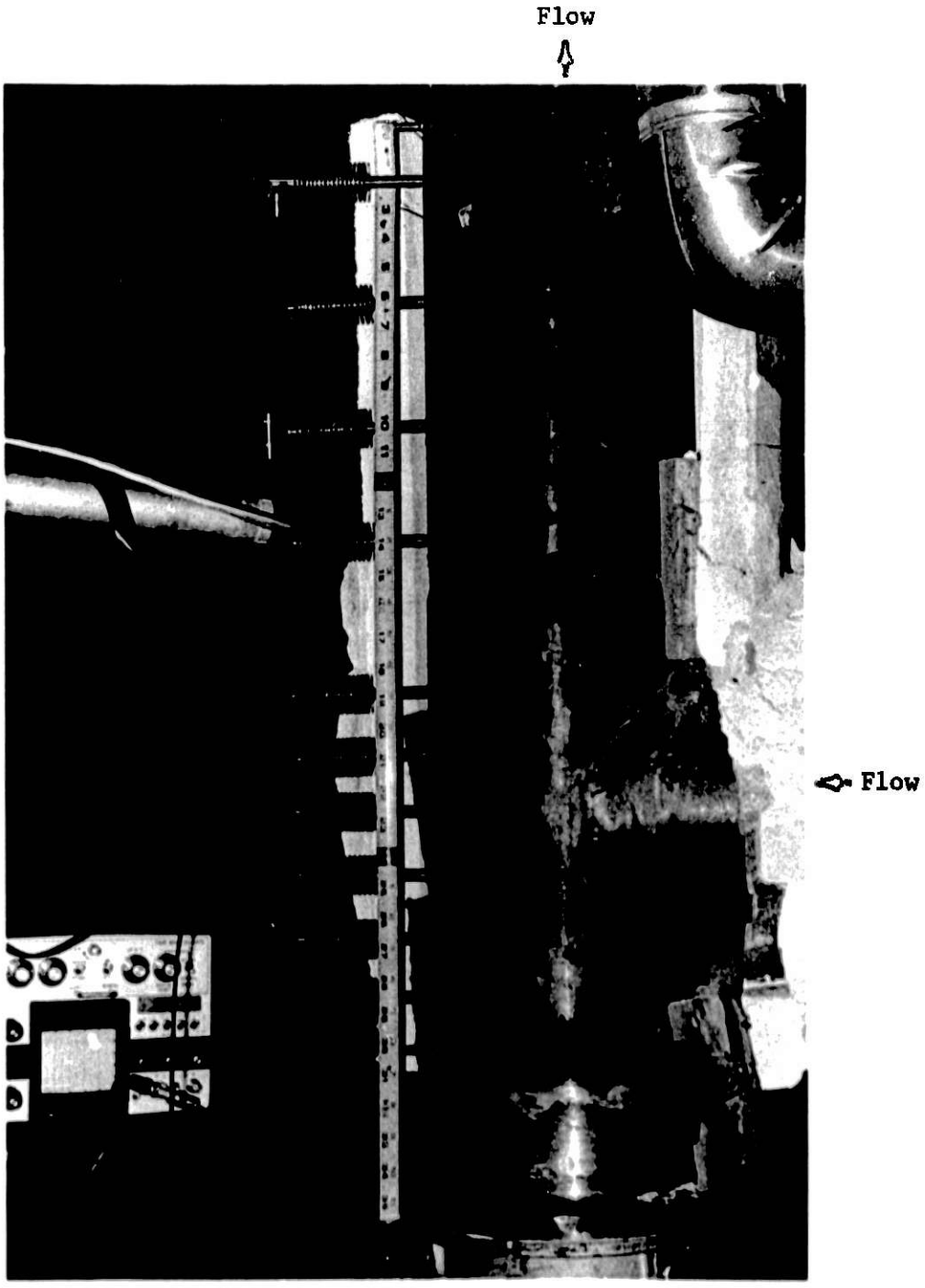

Fig. 10. Waveguides Installed on Bi-Gas Plant Off-gas Line Blocked Tee.

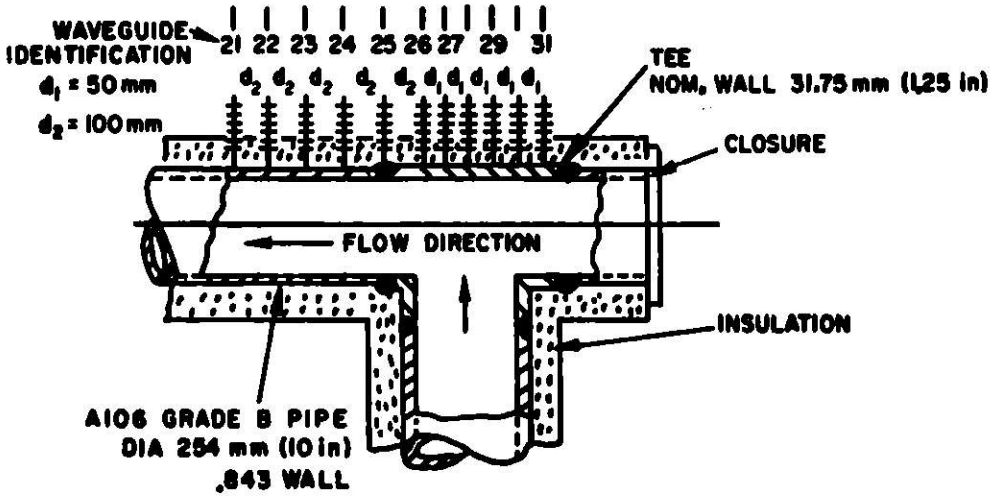

Fig. 11. Schematic of Waveguide Placement on Carbon Steel Blocked Tee in Bi-Gas Main Coal-feed Line. ANL Neg. No. 306-78-118.

b. Refractory-lined Transfer Lines

(1) Infrared. A final report on phase I of the application of infrared imaging for quantitatively determining the erosive-wear cavity from surface-temperature patterns has been completed. This report is presently being prepared for release.

(2) Gamma Radiography. A field study of the lining of the pressure vessel at the Babcock and Wilcox Research Center was made this quarter. These results are being analyzed and will be reported next quarter. A final report on the findings of the gamma-radiography study is being prepared, and a first draft has been completed. This will be issued in final form within the next six months.

2. Refractory Installation Practices

a. Detection of Thermally Induced Acoustics from Refractory Materials

Work has continued this quarter on the use of acoustic emission as a means to control the firing schedule of thick castable refractory concrete linings of the type envisioned for the main process vessels in coal-gasification, liquefaction, and fluidized bed plants. Previous work[1] on this program has shown that a "Kaiser-" type effect is acoustically detected if mechanically unloaded samples are thermally cycled. This is consistent with the results reported by Schuldies[9] for mechanically loaded high-density structural ceramic specimens. Also, previous data obtained in this program indicated that, for thermally cycled, uniformly heated samples under no mechanical load, most of the acoustic activity during initial heating occurred at temperatures below 500-600°C. Although data have also shown that different cool-down schedules significantly affect the acoustic-emission output, to date these data have not been correlated with a damage-indicating factor. These results are in qualitative agreement with industrial observations[10] that show significantly more macrocracking occurs if cool-down is not controlled and also agrees with data obtained on a large monolithic (1.5 x 2 x 0.25 m) panel, which was fired using a continuous-firing schedule.

To compare the characteristics of acoustic emission of small samples with the large panel tests, samples similar to those used in the thermal-cyclying experiments were continuously fired. The depth of embedment of the fused silica acoustic waveguide was reduced to 6 mm from the previous 12 mm, since acoustic coupling was satisfactory at this depth. The refractory concrete materials KAOTAB, Castolast-G, and Lightweight-26 castables were reexamined. The acoustic-emission data obtained from the continuous firing of the 95 and 60% Al_2O_3 materials are shown in Figs. 12 and 13. Note the dual spikes in the count-rate curves. These are in agreement with the data previously obtained and reported.[1] The temperatures at which the two spikes occur is interesting from the standpoint of shrinkage. Initially, Crowley[11] looked at shrinkage of insulating refractory concretes and noted the occurrence of a significant shrinkage reversal. In recent studies,[12,13] this

shrinkage reversal has been determined for specific refractory concretes of interest to coal conversion. The shrinkage reversal sets up internal stresses in the material.[14] These internal stresses are the result of differences in the thermal expansion coefficient between the aggregate and the cement. These highly localized stresses will be sufficiently large to cause microcracking,[15] and thus the total detected acoustic activity will undoubtedly be increased during the period when the stress levels are such that fracturing of low-strength bonds occurs.

Recently, two shrinkage curves were determined for the same insulating refractory concrete (Lite-cast 75-28) by two independent laboratories. A comparison of these curves is shown in Fig. 14. A comparison of the shrinkage curve for Lite-cast 75-28 with acoustic-emission data for Lightweight-26 is interesting from a trend point of view. In Fig. 15, acoustic-emission data for Lightweight-26 and Lite-cast 75-28 show the same high level of acoustic activity in the temperature region where shrinkage recovery is taking place. The significance of this recovery is greater when taking into account the thermal gradient that will exist in a full-scale design, i.e., the major portion of the insulating refractory concrete thickness would be in the critical temperature zone between 150 and 500°C. Related work on a heat-transfer program at Battelle[12] has shown a typical thermal profile on a dual-component lining. The experimentally determined profile is reproduced in Fig. 16, which shows 60% of the thickness of the insulating concrete is in the critical temperature region where shrinkage reversal is occurring and significant acoustic activity would probably be evident. Thus, significant acoustic activity could be expected from such a lining when steady-state conditions at the hot face are such that the majority of the insulating concrete is in the critical region. Because of the significant acoustic activity generated during shrinkage reversal, the separation of acoustic-emission signatures of hot face and insulating concretes is a necessity. This will be examined in more detail in this test program.

Samples of various refractory concrete materials, which had been acoustically monitored during thermal cycling, were subjected to four-point-bend tests to determine the modulus of rupture. The 2.5 x 2.5 x 26 cm samples were placed in a four-point-bend fixture in an Instron tensile machine and run at a crosshead speed of 0.125 cm/s. Table VI shows the results of the tests. These results were then compared with acoustic parameters to ascertain if a correlation existed between an acoustic-emission parameter and a modulus of rupture. Table VII shows the relation between the modulus of rupture and the total ringdown counts. It is interesting to note that the higher the total number of ringdown counts the lower the modulus of rupture value. This suggests that the detected acoustic activity is a form of mechanical degradation such as microcracking.

As an additional study of the sensitivity of acoustic-emission degradation, runs made this quarter with continuous firing were analyzed using amplitude distribution analysis. Also, the acoustic-emission

signature obtained directly from the preamplifier was recorded on a broadband magnetic tape recorder. Data were automatically recorded for 90 s every 90 min. Analysis of the magnetic-tape data has shown that the acoustic-emission activity is quite continuous and has an overlap of individual bursts, and thus separation of individual bursts is difficult.

An acoustic-emission parameter indicative of the nature of the cracking being detected was first reported by Pollock.[16] Pollock indicated that, if the peak burst amplitudes are selectively recorded in individual recording channels (such as a multichannel analyzer), the number of detected events, n(a), with peak amplitudes larger than a_o may be fitted to a power law relation of the general form

$$n(a) = \left(\frac{a_i}{a_o}\right)^{-b}, \qquad (1)$$

where a_o is the lowest detectable threshold amplitude (voltage), a_i is the peak voltage in selected channels, and b is an empirically derived constant. The information to be obtained is the value of the exponent b, which has been shown to be indicative of the nature of the cracking being detected in brittle as well as ductile materials. The reported values of b[16,17] range between 0.4 and 2.0. The lower values are indicative[17] of failure processes preceded by a small number of large events, and the higher values are indicative of failure processes preceded by a large number of small events. Also, the utility of the b value is greater because the value of b does not change, if all emissions are changed by the same factor.[17]

Figures 17-19 show amplitude distributions for different temperature ranges during the heating cycle. These data were obtained by summing the amplitude distribution at the end of critical temperature zones determined on previous runs. In general, all data show maximum event counts during the 100-500°C heatup period and again during the 500-100°C period on cool-down. All plots show lower channel voltage threshold values. The value for a_o was 13.82 mV, thus channel one, which accepts voltage levels between 11 and 19.9 mV, has a partial counting.

Analysis of the amplitude distribution data has been completed by summing the amplitude distributions over the entire firing schedule and then plotting $\log_{10} n(a)$ versus $\log_{10} \left(\frac{a}{a_o}\right)$ to obtain the b values. These plots are shown in Figs. 20-22. Note that the values of b are in the expected range from 1.5 to 1.9. Additionally, Figs. 21 and 22 are, respectively, the plots for a 175-kHz transducer and a broadband transducer (200 kHz-1.5 MHz). These data agree with the Stone and Dingwall[17] analysis that equal attenuation of all values does not change the "b" value. It is to be noted however that these values of b are for the lumped channels, as noted, and thus are not to be taken as absolute values. The interesting point to be made is that, in addition to other parameters such as count rate, time-dependent amplitude distribution analysis may hold the potential as a second parameter which can be used to predict large crack formation. During the next quarter, a panel test

will be conducted that will include thermal gradient and fast heating to develop large cracks. Both count rate and amplitude distribution will be examined as precursers to crack development.

TABLE VI. Four-point Modulus-of-rupture Data for Various Refractory Concretes

Refractory	Modulus of Rupture for Linear Cooling, MPa	Modulus of Rupture for Linear Cooling, psi	Modulus of Rupture for Exponential (Natural Furnace), MPa	Modulus of Rupture for Exponential (Natural Furnace), psi	Manufacturer's Specifications, MPa	Manufacturer's Specifications, psi
KAOTAB	6.129 6.101	889 885	7.025 6.750	1019 979	6.895- 9.653	1000-1400
Castolast G	11.024 11.362	1599 1648	12.265 12.169	1779 1765	11.720-15.860	1700-2300
Lightweight-26	0.916 0.945	133 137	1.227 1.269	178 184	0.620- 1.034	90- 150

TABLE VII. Relation between Modulus of Rupture and Total Ringdown Counts

Refractory	Cooling Schedule	Room-temperature Modulus of Rupture, MPa (psi)	Run	Total Ringdown Counts at End of 1000°C Cycle
KAOTAB	Linear	6.101-6.129 ±0.206 (885-339 ±30)	9	3932×10^3
	Furnace	6.750-7.025 ±0.413 (979-1019 ±60)	11	2675×10^3
Lightweight 26	Linear	0.916-0.945 ±0.082 (133-137 ±12)	12	262×10^3
	Furnace	0.227-1.269 ±0.089 (178-184 ±10)	13	192×10^3

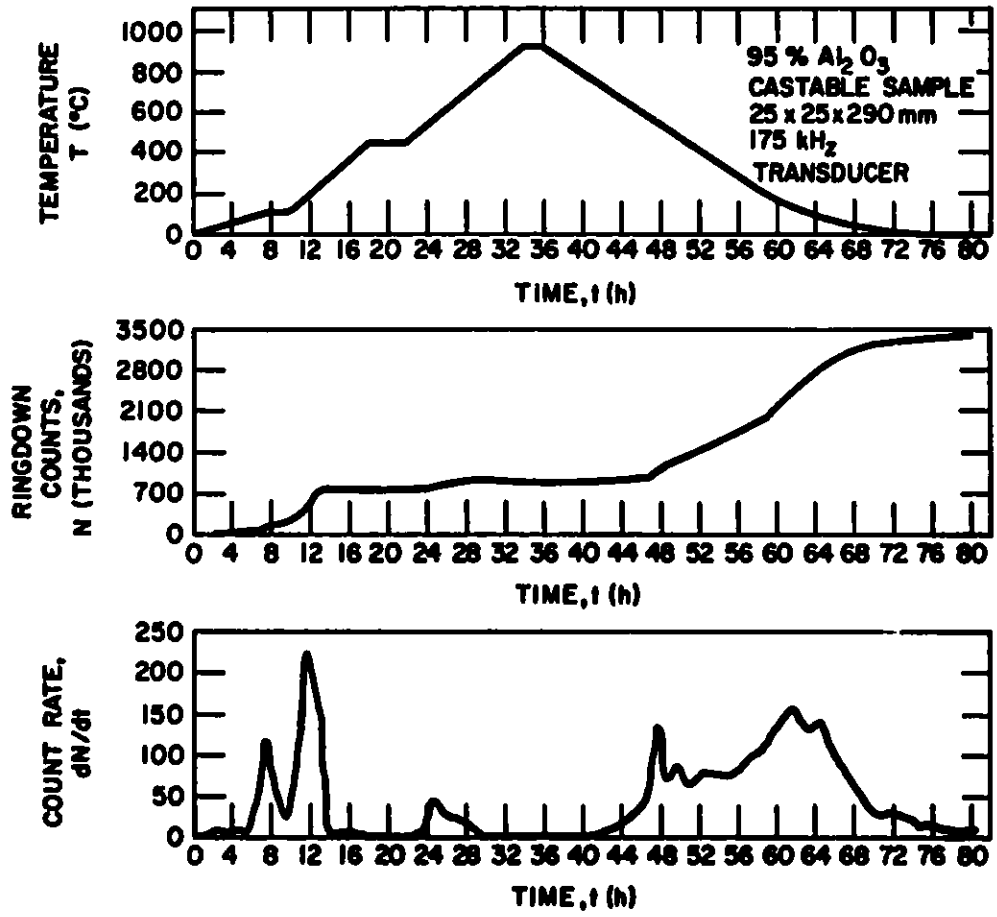

Fig. 12. Characteristic Acoustic Emission of 95% Al_2O_3 Monolithic Refractory Sample under Uniform Heating: (a) Sample Temperature History, (b) Ringdown Counts, and (c) Count Rate. ANL Neg. No. 306-78-56.

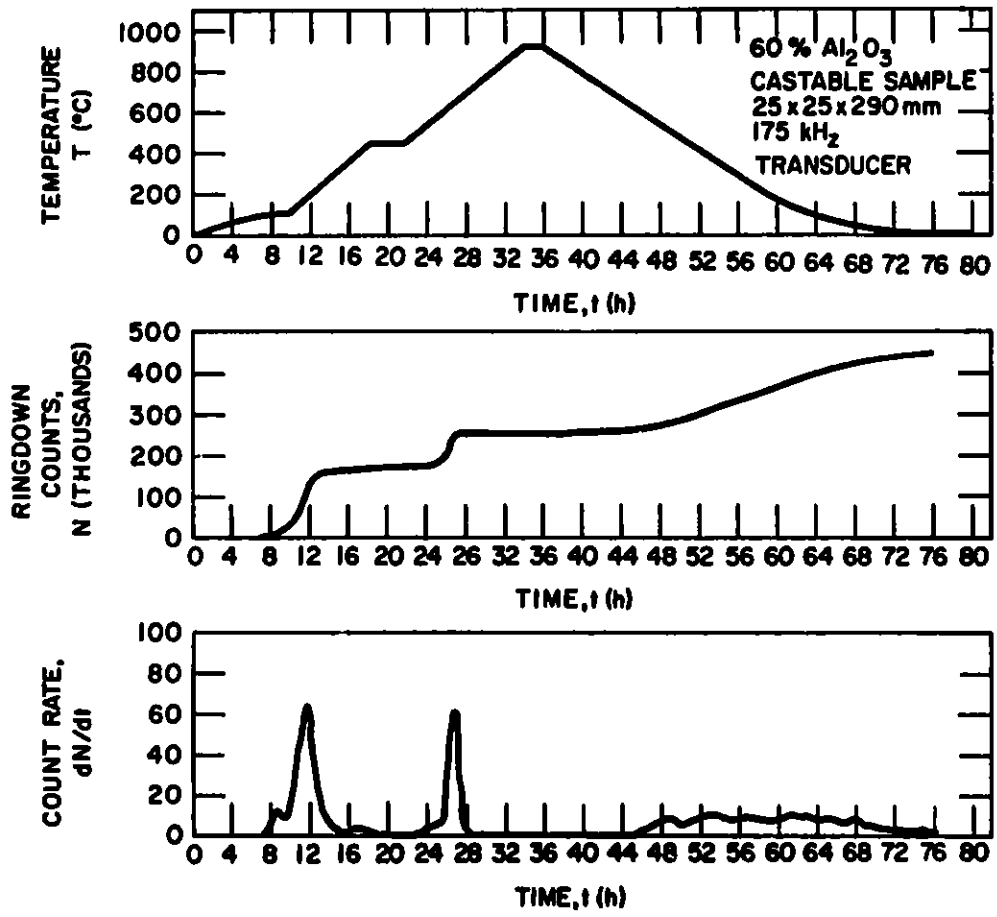

Fig. 13. Characteristic Acoustic Emission of 60% Al_2O_3 Monolithic Refractory Sample under Uniform Heating: (a) Sample Temperature History, (b) Ringdown Counts, (c) Count Rate. ANL Neg. No. 306-78-55.

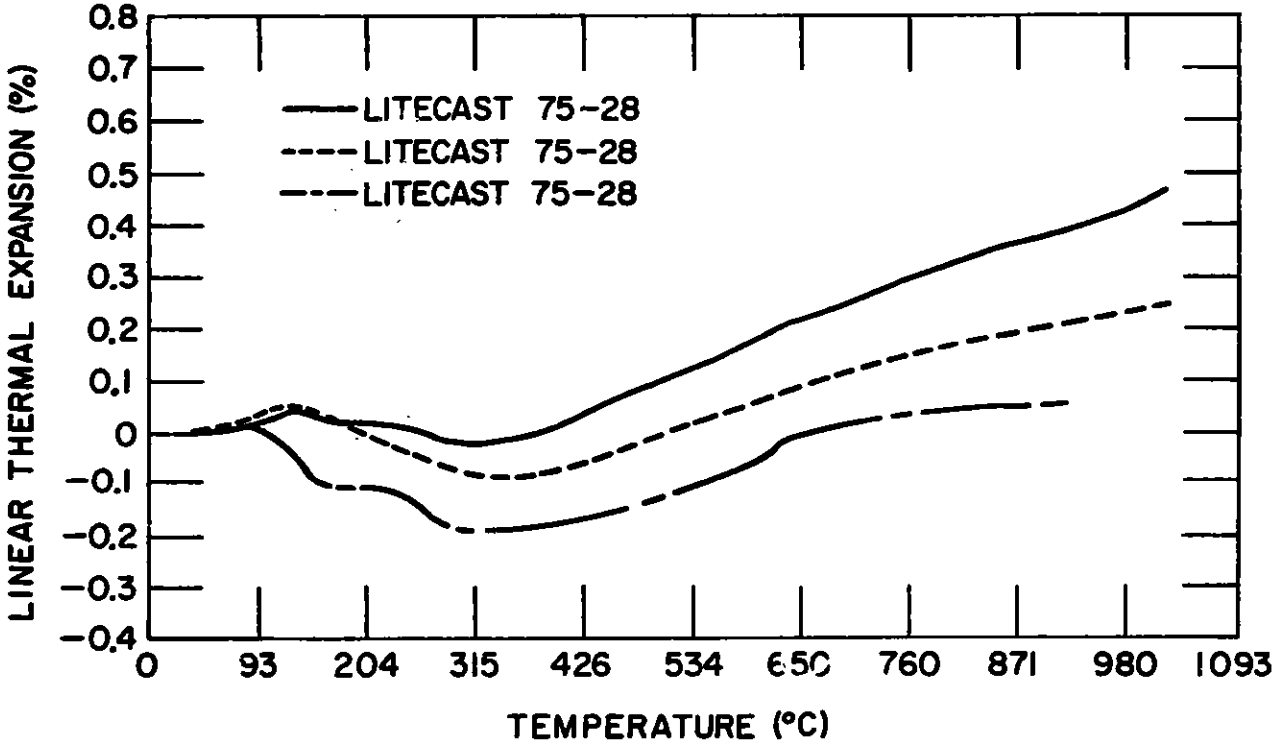

Fig. 14. Characteristic Shrinkage Curves for Lightweight Castable Refractory Concrete as Determined by Two Independent Laboratories. ANL Neg. No. 306-78-53.

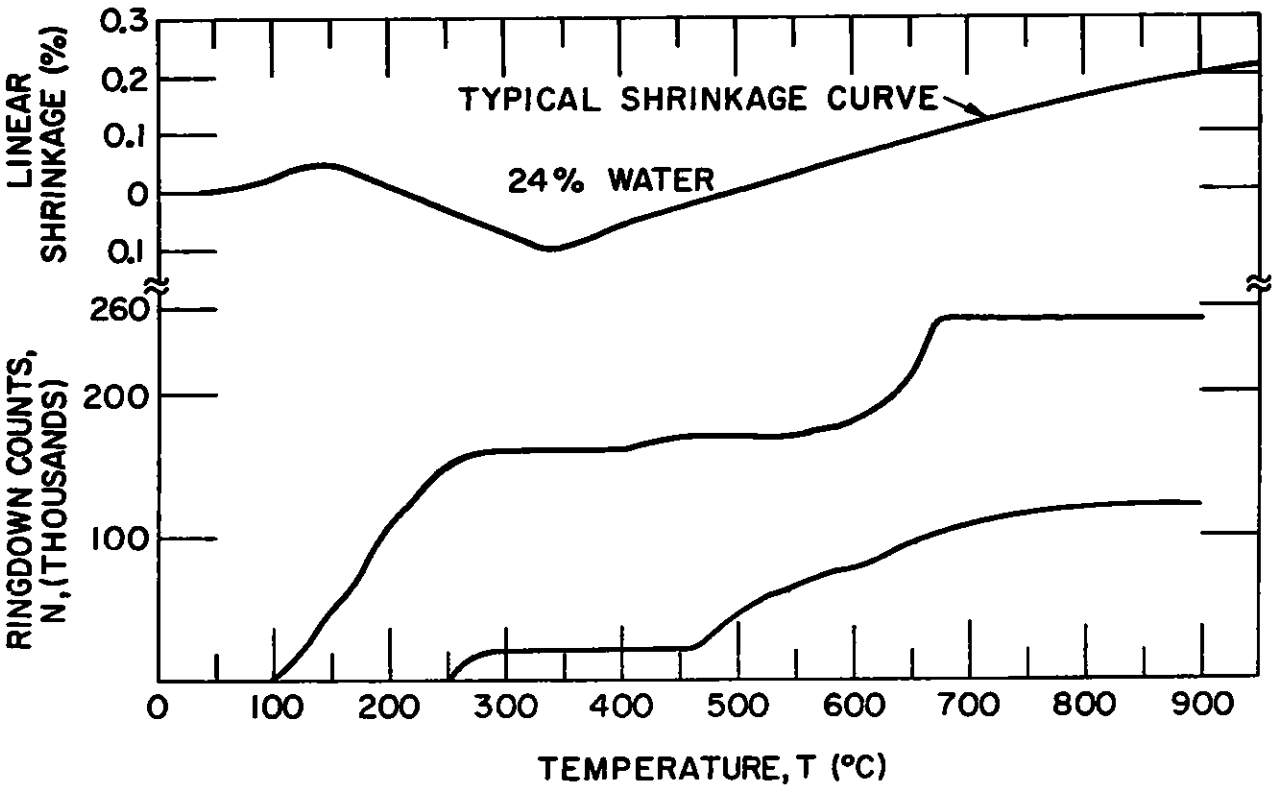

Fig. 15. A Comparison of Acoustic Emission with Refractory Shrinkage. ANL Neg. No. 306-78-52.

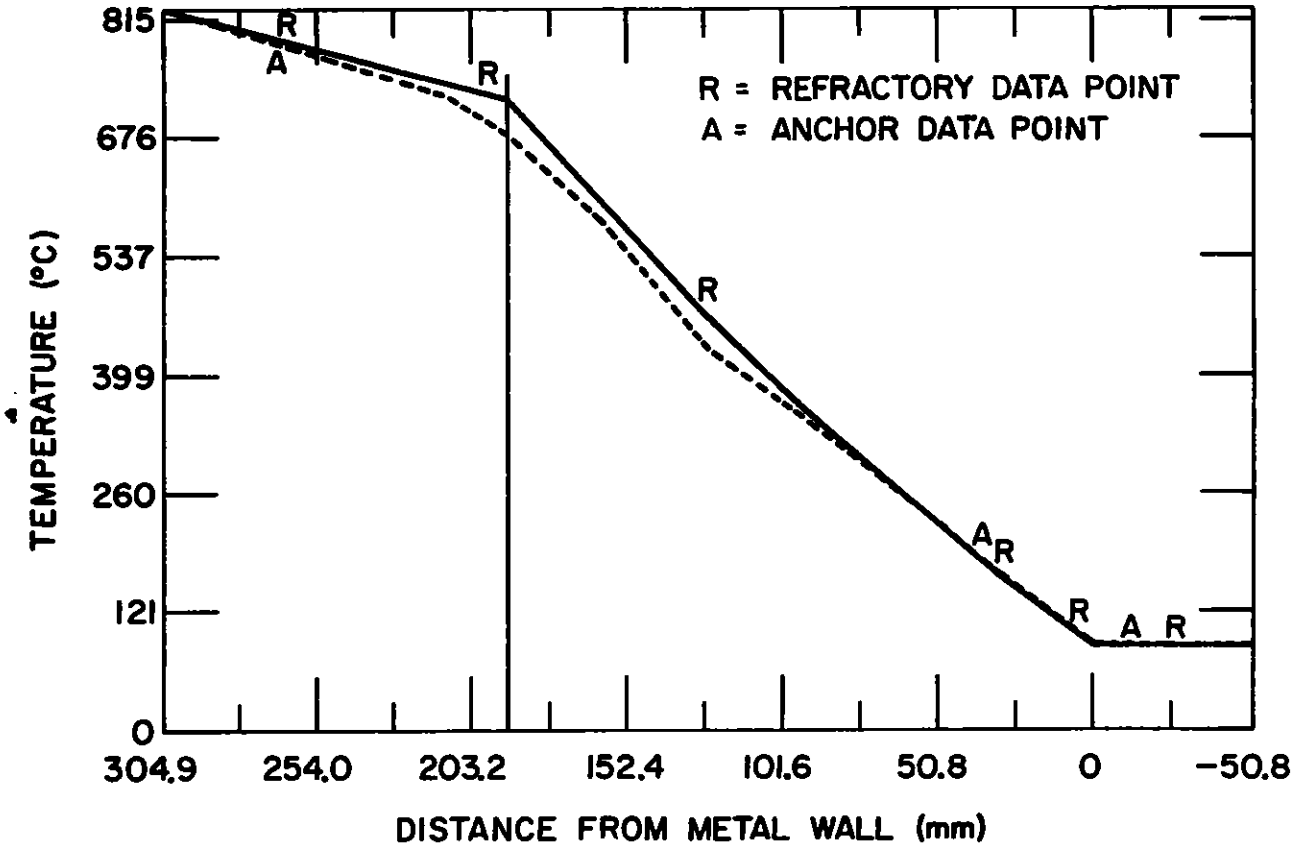

Fig. 16. Thermal Profile of Dual-component Refractory Lining under Steady-state Conditions (from Battelle[12]). ANL Neg. No. 306-78-54 Rev.

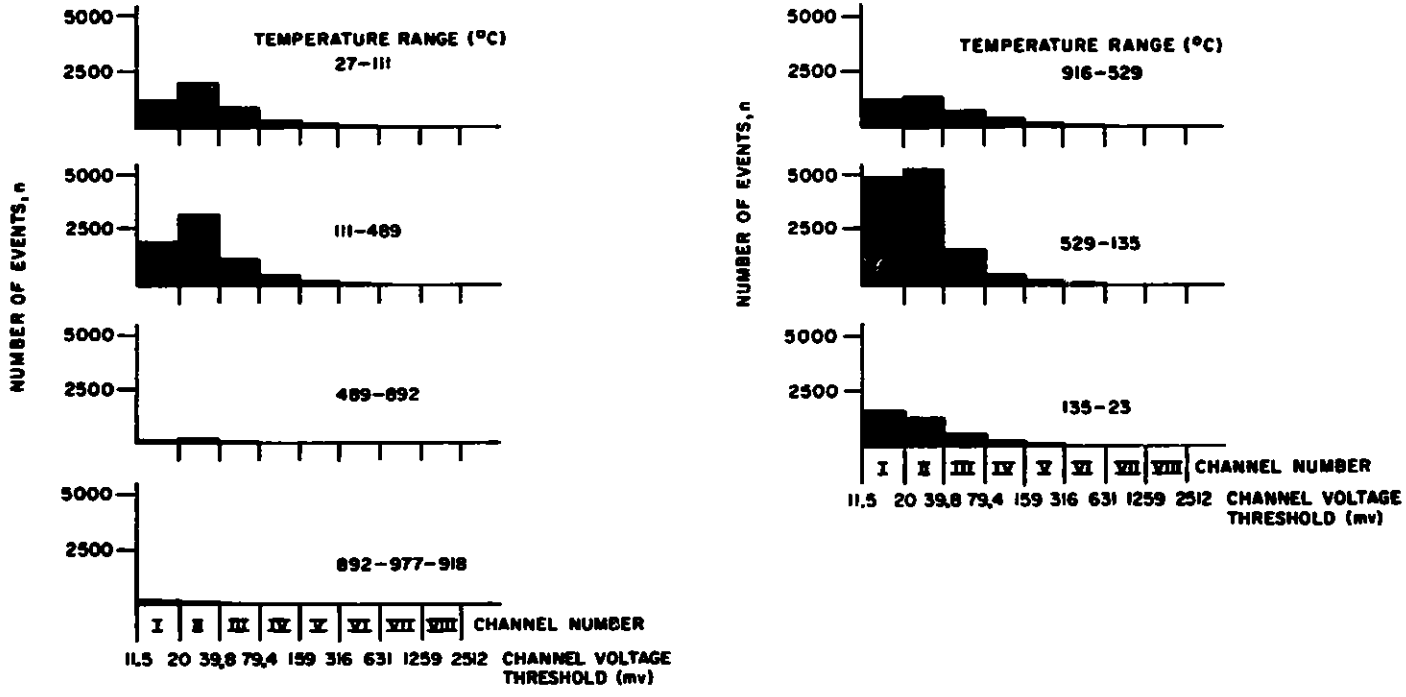

Fig. 17. Amplitude Distribution as a Function of Selected Temperature Ranges for Castolast G (Broadband Transducer). ANL Neg. Nos. 306-78-46 and 306-78-47.

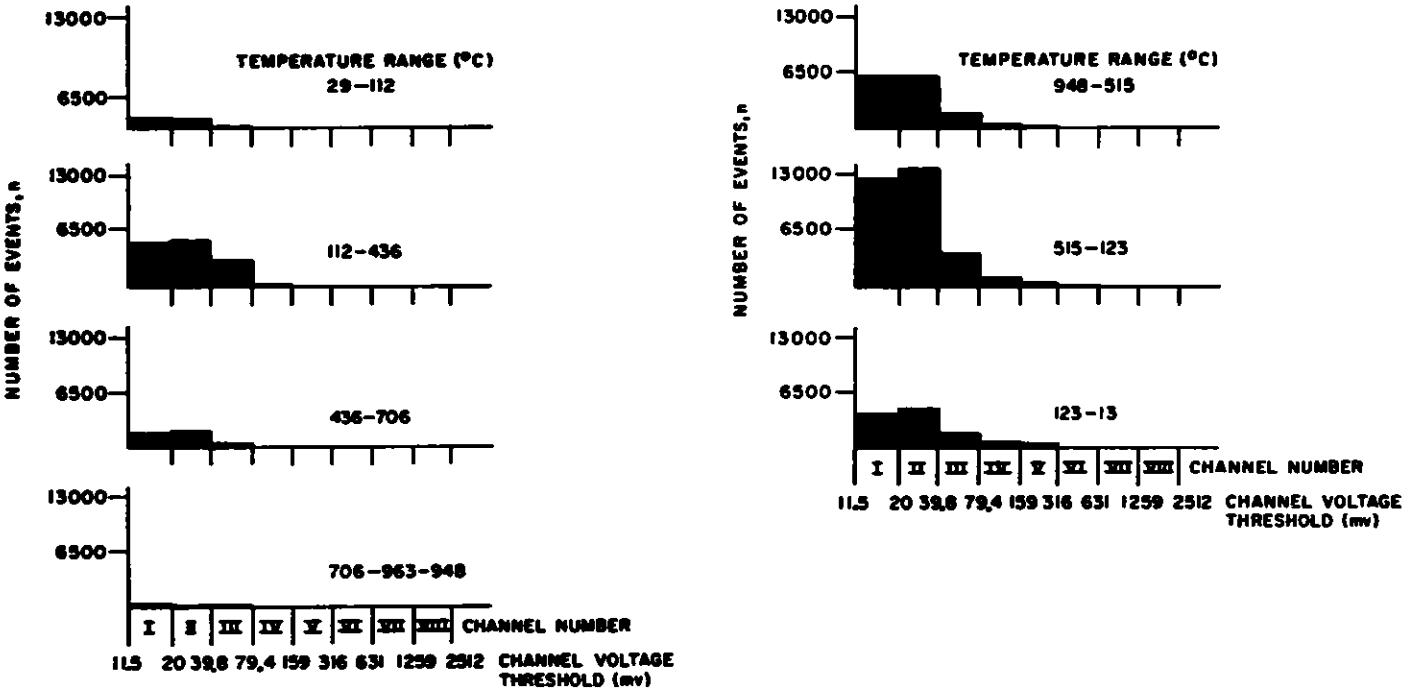

Fig. 18. Amplitude Distribution as a Function of Selected Temperature Ranges for Lightweight-26 (Resonant Transducer -- 175 kHz). ANL Neg. Nos. 306-78-58 and 306-78-59.

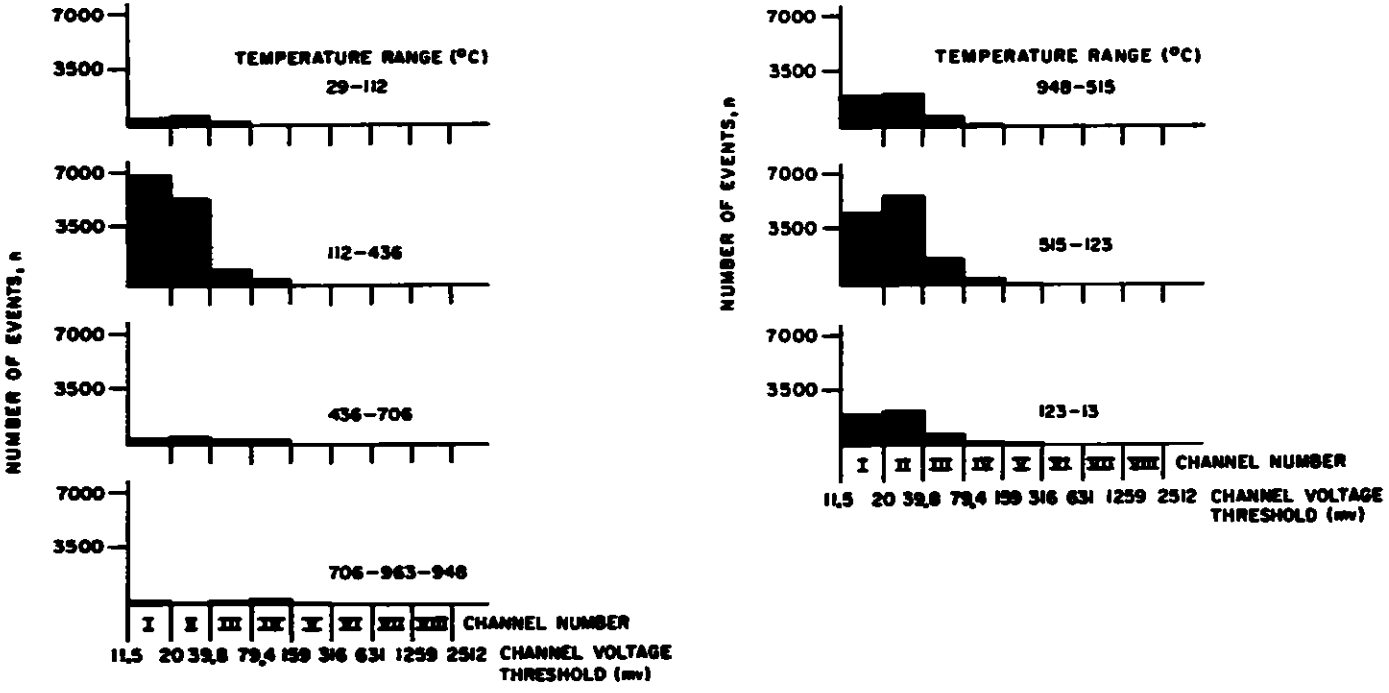

Fig. 19. Amplitude Distribution as a Function of Selected Temperature Ranges for Lightweight-26 (Broadband Transducer). ANL Neg. Nos. 306-78-60 and 306-78-57.

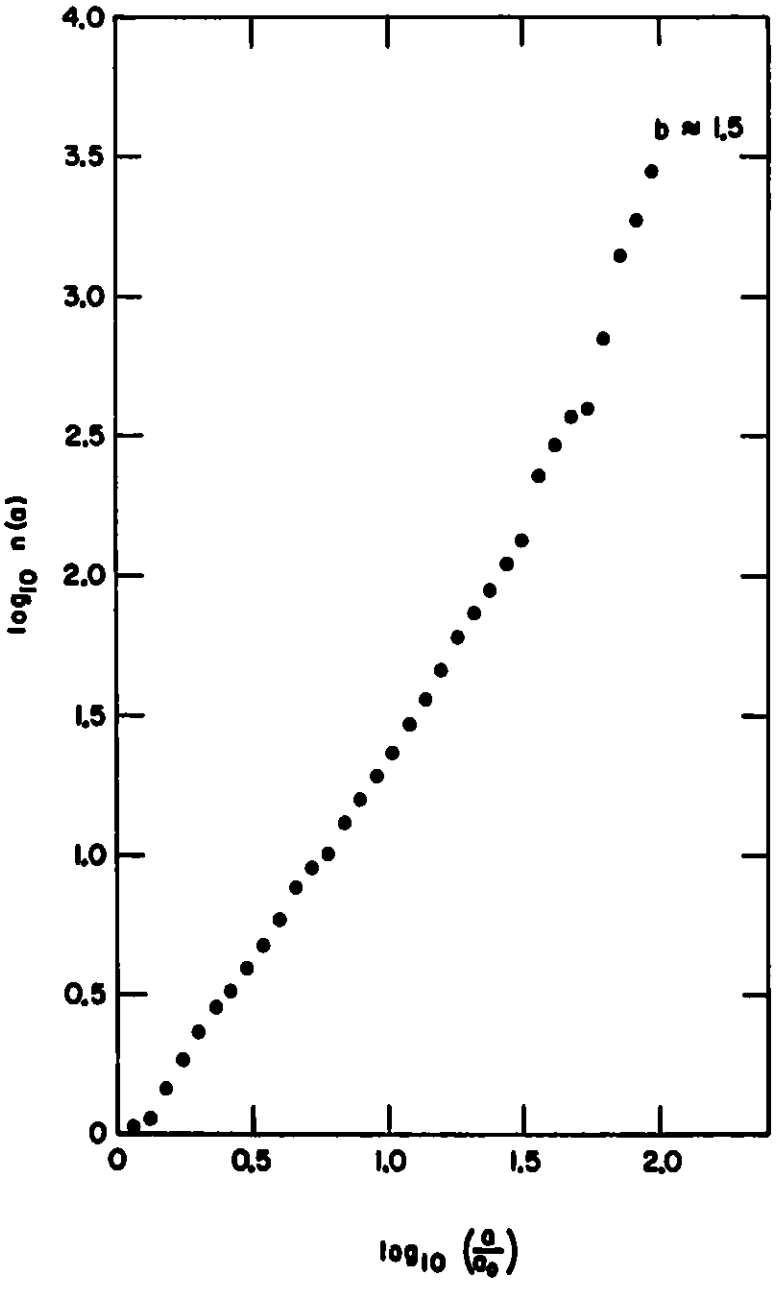

Fig. 20. Determination of Characteristic Exponent for Castolast G (Broadband Transducer). ANL Neg. No. 306-78-51.

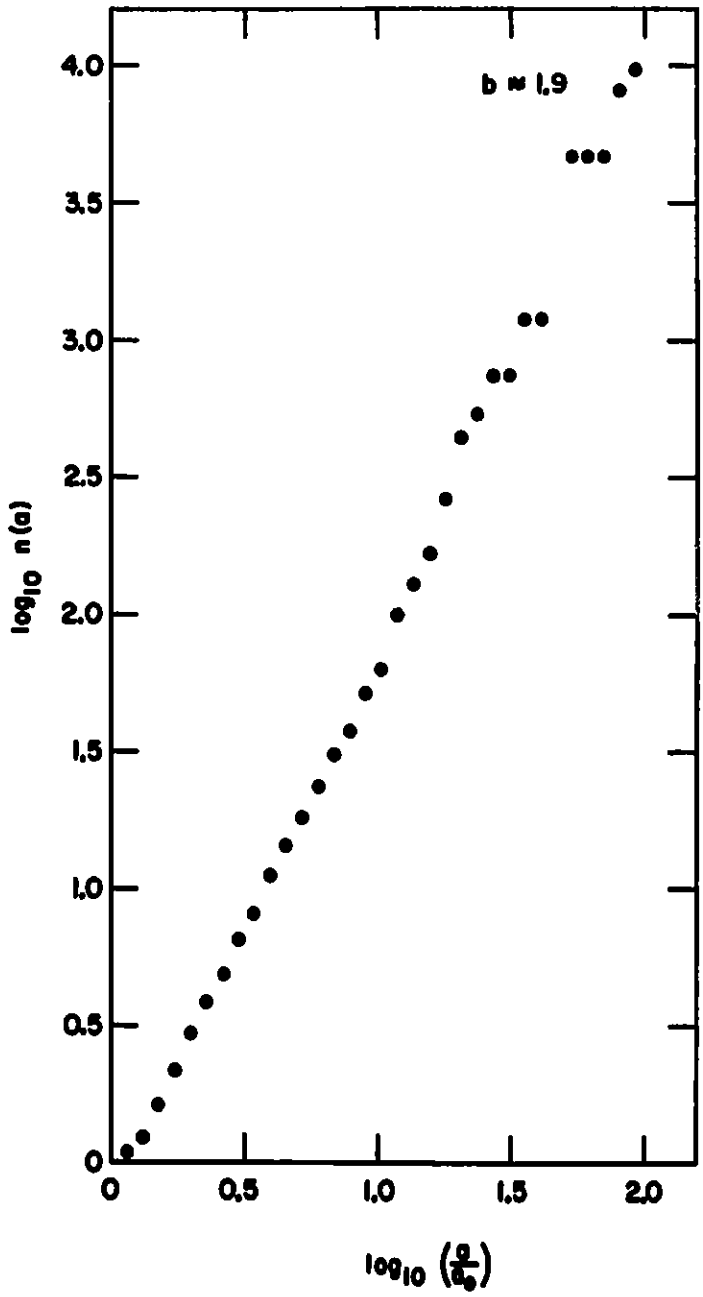

Fig. 21. Determination of Characteristic Exponent for Lightweight-26 (Resonant Transducer -- 175 kHz). ANL Neg. No. 306-78-50.

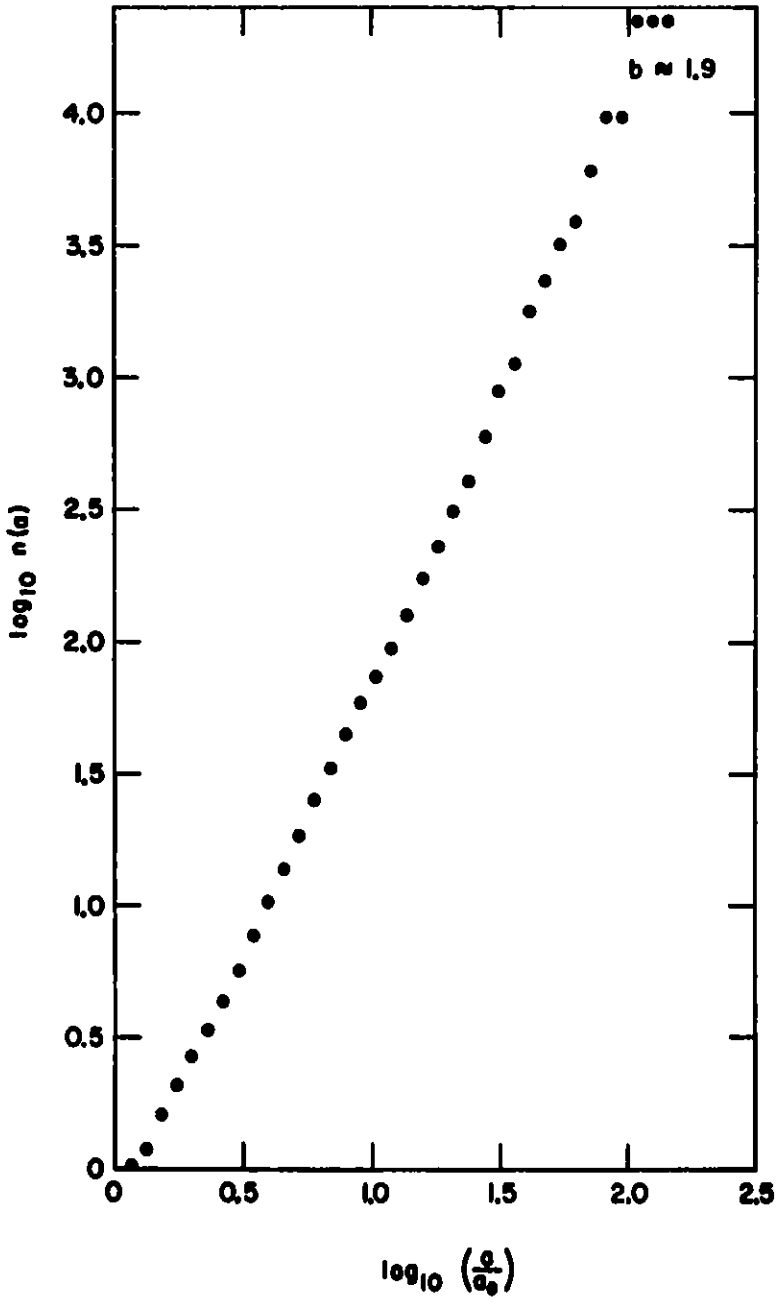

Fig. 22. Determination of Characteristic Exponent for Lightweight-26 (Broadband Transducer). ANL Neg. No. 306-78-49.

3. Component Inspection

a. Acoustic Monitoring of Valves

During this quarter, the theoretical model of Lighthill,[18] which was discussed in an earlier quarterly report,[3] was reexamined and compared with our experimental data. Additional tests were also carried out on a full-size valve at the Morgantown Energy Research Center (MERC) valve test facility.

From the theoretical model of Lighthill it is possible to deduce the following dimensional relationship for the noise generated by a subsonic turbulent jet:

$$S \sim \rho_j U^8 A_j / 2C_o^5, \tag{2}$$

where S is the acoustic power, ρ_j is the density of the gas in the jet, U is the velocity of the jet, A_j is the cross-sectional area of the jet, and C_o is the ambient sonic velocity. The basic validity of the Lighthill model has been well established for free jets discharging into the atmosphere (see, for example, Ribner[19] and Lighthill[20]), and evidence exists that the model is reasonably descriptive of the noise generated by throttling valves (Baumann,[21] Jenvey,[22] and Small[23]). However, it is important to note that Eq. (2) predicts the acoustic power radiated by the jet in the audible frequency spectrum. Its extrapolation to the description of the high-frequency (175-750 kHz) spectrum of interest for valve leak detection is difficult to justify rigorously, but some interesting preliminary results can be obtained from Eq. (2) that can be compared with the experimental data. It is convenient to rewrite Eq. (2) in the form

$$S/Q \sim U^7 / 2C_o^5, \tag{3}$$

where

$$Q = \rho_j U A_j \tag{4}$$

is the mass flow rate through the orifice. Ideally for a leak-detection system,

$$S/Q = \text{constant},$$

i.e., the acoustic output is directly proportional to the mass flow rate and independent of the leak geometry. However, Eq. (3) shows that the relationship between the acoustic output and the flow rate is, in fact, highly dependent on the leak geometry. Ignoring compressibility effects, Eq. (3) suggests that

$$S/Q \sim 1/A^7, \tag{5}$$

where A is the effective cross-sectional area of the leak. Since, in practice, A is unknown, Eq. (5) suggests that attempts to develop a quantitative acoustic leak-detection system are unlikely to be successful for incompressible flows. For gas flows at high pressure where compressibility effects are important, the situation is more encouraging. If the pressure drop across the valve or orifice is sufficiently high, the flow through the orifice will be choked, i.e., the flow at the throat of the orifice will be sonic. In this case, Eq. (3) suggests that

$$S/Q = \text{constant}, \tag{6}$$

which is promising from the viewpoint of developing a leak-detection system.

Tests have been carried out on three orifice plates with right-circular cylindrical orifices and orifice diameters of 1/16, 1/64, and 1/100 in. (∿ 1.6, 0.4, and 0.2 mm). The 1/64-in. (0.4-mm) orifice appears to be a reasonable laboratory model for the volume of leakage expected in practice. The 1/16-in. (1.6-mm) orifice was included to represent the case in which the flow is subsonic everywhere, and the 1/100-in. (0.2-mm) orifice was included to represent the case where the leakage is somewhat less severe than the MERC limit.

It is well known (see, for example, Shapiro[24]) that, when the flow is choked, the mass flow rate Q is linearly proportional to the product of the upstream pressure p and the area of the orifice A

$$Q \sim pA. \tag{7}$$

The experimentally measured flow rate as a function of pA is shown in Fig. 23 for the three orifice plates. The two smaller orifices are choked over the entire pressure range examined (a linear least-squares fit of the data gives a coefficient of correlation r = 0.999). The flow through the 1/16-in. orifice is unchoked over the entire pressure range examined, although at higher pressures it is approaching the choked flow limit.

Equation (3) predicts that, for unchoked flow, the ratio of the acoustic output S to the flow rate Q is proportional to the seventh power of the velocity U at the orifice throat. In our experiments, U can be estimated for low velocities where the flow is nearly incompressible from continuity considerations as

$$U = Q/A, \tag{8}$$

where Q is the flow rate, and A is the cross-sectional area of the orifice. However, for U > 150 m/s, a more complex calculation that incorporates the effect of compressibility is required. Reasonably accurate values for unchoked flows can be obtained from the work of Hall and Orme[25] on the flow of a compressible fluid through a sudden enlargement in a pipe.

The experimental results for the dependence of S/Q on U are shown in Fig. 24. Least-squares fits through the data points give

$S/Q \sim U^{2.5}$ 175-kHz transducer

$S/Q \sim U^{2.6}$ 375-kHz transducer

$S/Q \sim U^{2.2}$ 750-kHz transducer.

The dependence of the acoustic output on the jet velocity is much weaker than predicted by theory. However, the experimental results seem to support the conclusion that quantitative leak measurements for unchoked flows are unlikely because the relation between the acoustic output and the flow rate is dependent on the actual leak geometry (size), which is unknown in practice.

The variation of acoustic output S with flow rate Q for the three orifice sizes examined is shown in Figs. 25-27. For the choked flow case, theory predicts $S \sim Q$. The experimental data points were least-squares fit by curves of the form $S \sim Q^m$. The results of the curve fits are summarized in Table VIII. For the 1/64- and 1/100-in. orifices, which are choked, the exponent m ranges from 1.1 to 2.5, but in most cases it is ≤ 1.5. Additional examination of the data for the choked-flow cases shows that not only is the variation of acoustic output with flow rate similar in both cases, but also the amplitudes of the acoustic output for a given flow rate for the two orifices are sufficiently close to suggest that, although the acoustic output may not be completely independent of orifice size as predicted by theory, the dependence is fairly weak and at least a semi-quantitative correlation may be obtained.

Additional experiments are planned to examine the 1/16-in. orifice in the choked-flow regime and thus extend the range of orifice sizes considered. Also, rectangular slit-type orifices will be examined to investigate the effect of orifice shape on the acoustic output.

The results of the tests on the 6-in. Sigmon ball valve at MERC are summarized in Table IX. For convenience in analyzing the data, the tests have been ordered in terms of increasing plenum pressure. Scatter exists in the data, but the basic agreement is good with a coefficient of correlation $r(S,Q) = 0.802$. A similar analysis can be carried out for the 4-in. Jamesbury ball valve discussed in a previous quarterly.[1] Data for this valve are summarized in Table X. The correlation between the acoustic signal level S and the flow rate Q is not particularly good [$r(S,Q) = 0.541$]. Note, however, that a much better correlation exists between the signal level S and the upstream pressure P [$r(S,P) = 0.856$]. Thus, in these tests, the acoustic signal level seems to be a better measure of the driving pressure than the flow rate. It is our current feeling that a large part of the relatively poor correlation between the acoustic signal level and the observed leakage is due to the relatively low pressures involved. For a leak of fixed

geometry operating in the choked-flow (high pressure) condition, the leakage rate should be proportional to the pressure. However, the correlation between the leak rate and the pressure is poor for the 4-in. valve [r(Q,P) = 0.411], although similar to the correlation between S and Q, it is much better for the 6-in. valve [r(Q,P) = 0.799]. At the higher pressures encountered in practice, Q should be proportional to the pressure, and the situation should be much closer to the orifice flows studied in the laboratory.

TABLE VIII. Variation of Acoustic Output S with Flow Rate Q; $S \sim Q^m$

Orifice Size, in.	Transducer Frequency, kHz	Exponent m	Coefficient of Correlation[a]
1/16	175	3.8	0.979
	375	4.3	0.981
	750	4.0	0.973
1/64	175	1.1	0.828
	375	2.5	0.992
	750	1.4	0.949
1/100	175	1.1	0.991
	375	1.5	0.999
	750	1.4	0.999

[a]The coefficient of correlation r is a measure of the goodness of fit of the assumed form $S = KQ^m$ to the experimental data points; if r = 1 the correlation is exact, if r = 0 the points are uncorrelated.

TABLE IX. Acoustic-emission Testing on a 6-in. Full-port Ball Valve[a]

Test	Signal Level S,mV	Flow Rate Q,$\mu m^3/s$	Pressure P,MPa
1	30	472	0.70
2	70	613	0.99
3	70	566	1.01
4	90	660	1.08
5	140	613	1.09
6	140	707	1.14
7	130	566	1.17
8	150	660	1.21
9	190	755	1.23

[a]All tests were carried out with a 175-kHz resonant-type transducer (AET FC-175).

TABLE X. Acoustic-emission Testing on a 4-in. Full-port Ball Valve[a]

Test	Signal Level S,mV	Flow Rate Q,$\mu m^3/s$	Pressure P,MPa
1	0	406	0.85
2	30	439	0.87
3	0	420	0.88
4	1	401	0.89
5	233	439	0.90
6	230	443	0.91
7	110	424	0.91
8	144	396	0.92
9	415	462	0.94
10	682	434	0.95

[a]All tests were carried out with a 175-kHz resonant-type transducer (AET FC-175).

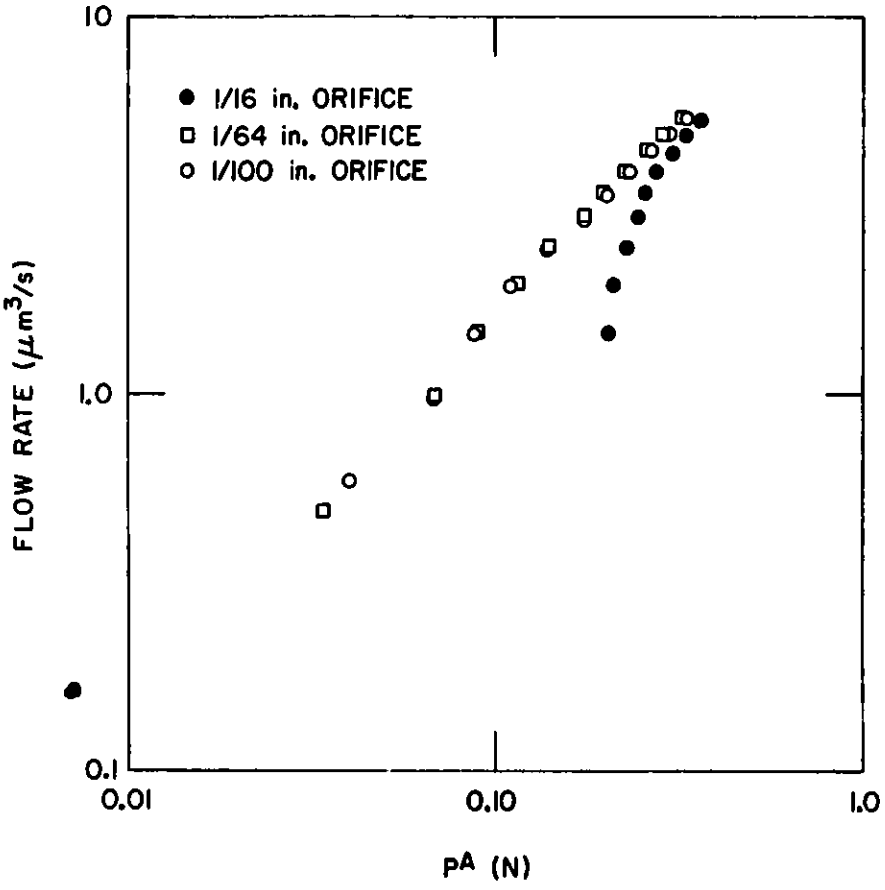

Fig. 23. Flow Rates as Functions of the Product of the Upstream Static Pressure and the Orifice Area. ANL Neg. No. 306-77-589.

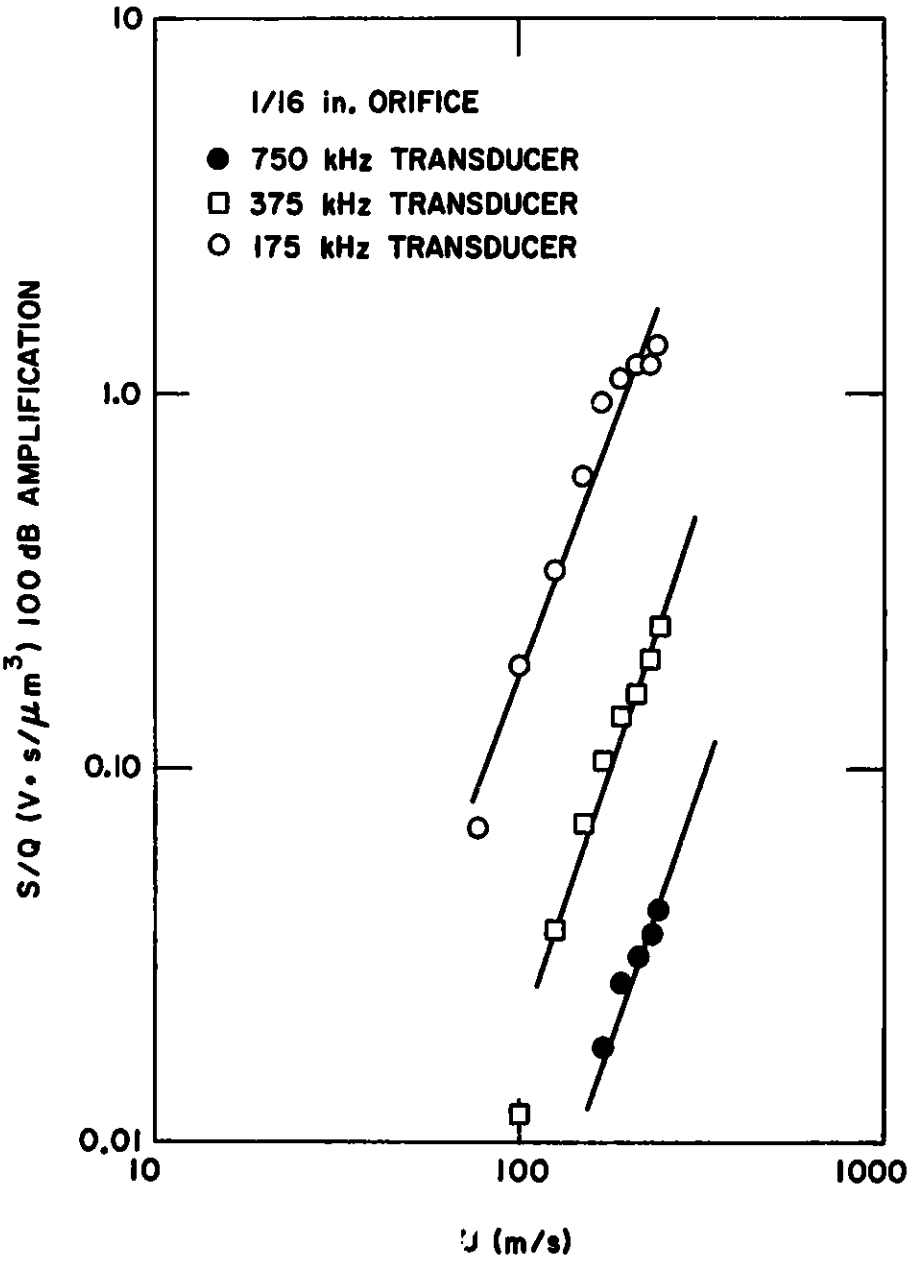

Fig. 24. Ratio (S/Q) of the Acoustic Output to the Flow Rate as a Function of the Orifice Velocity U for Different Transducer Frequencies. ANL Neg. No. 306-77-593.

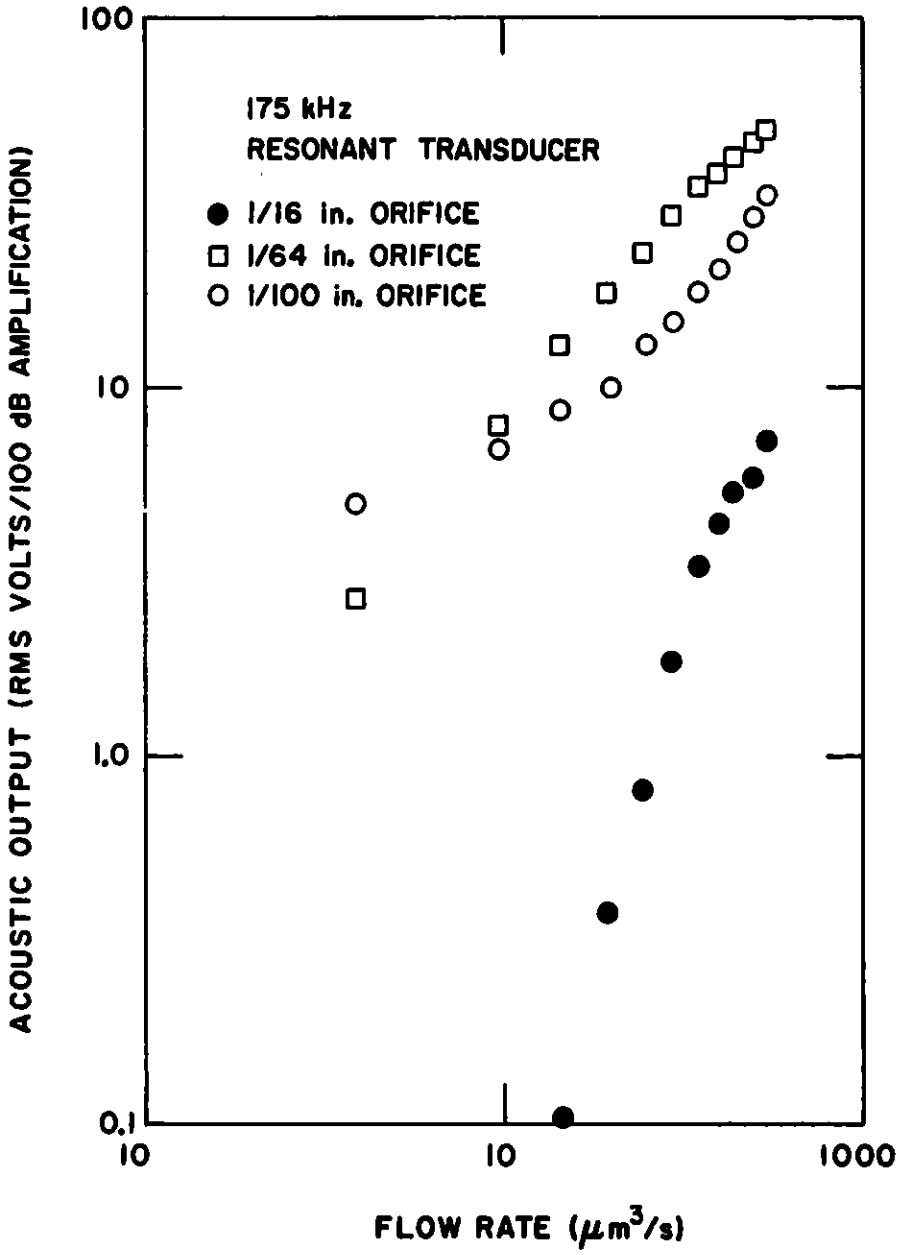

Fig. 25. Acoustic Output of the 175-kHz Transducer as a Function of Flow Rate for Different Transducer Frequencies. ANL Neg. No. 306-77-586.

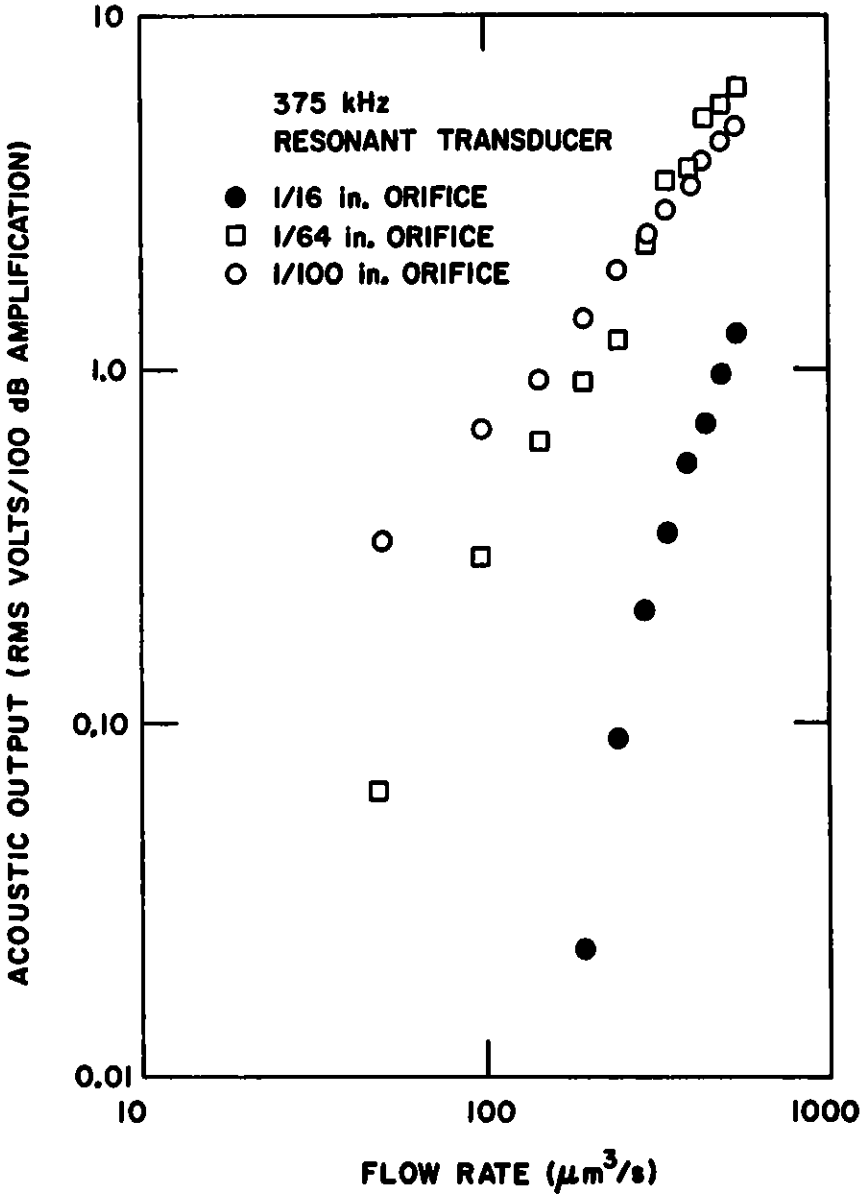

Fig. 26. Acoustic Output of the 375-kHz Transducer as a Function of Flow Rate for Different Transducer Frequencies. ANL Neg. No. 306-77-594.

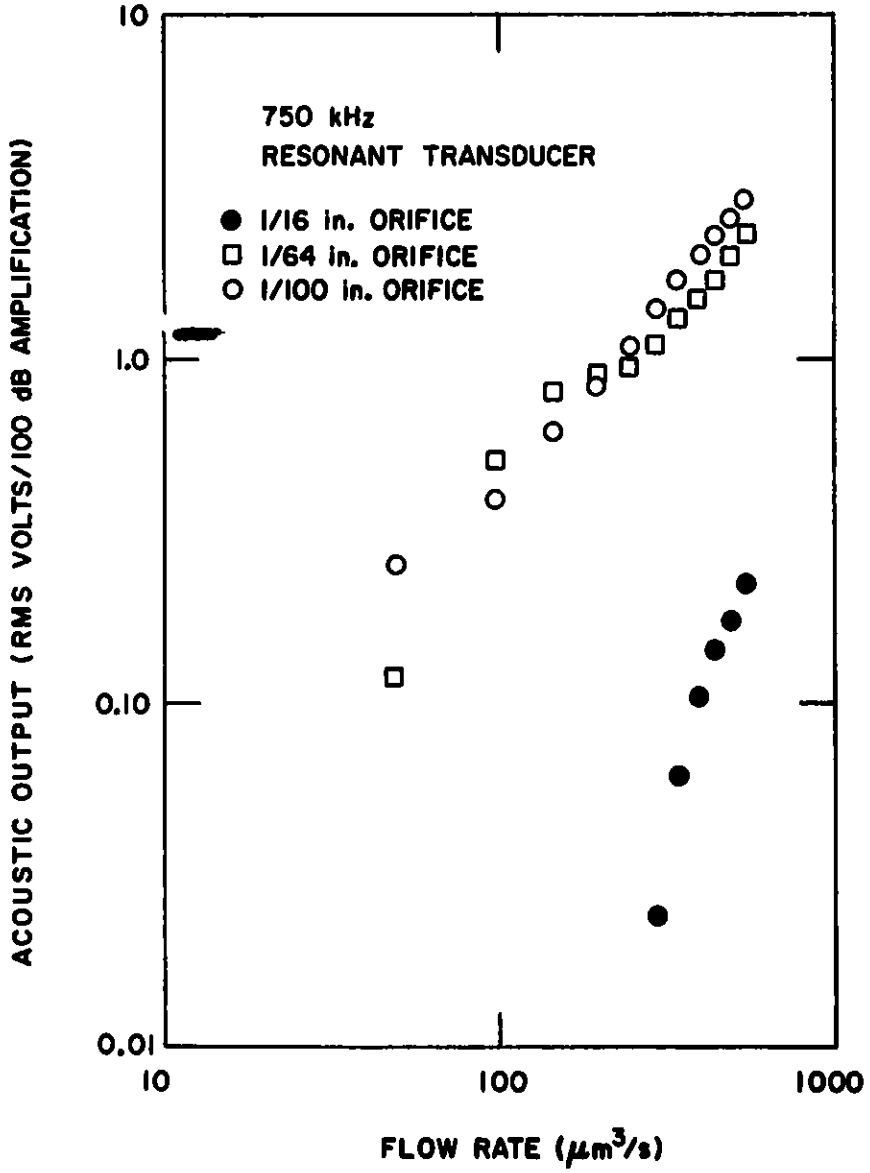

Fig. 27. Acoustic Output of the 750-kHz Transducer as a Function of Flow Rate for Different Transducer Frequencies. ANL Neg. No. 306-77-590.

Task D -- Corrosion Behavior of Materials in Coal-conversion Processes
(K. Natesan)

The objectives of this program are to (1) develop uniaxial tensile data on four selected commercial alloys during exposure to multicomponent gas environments, (2) experimentally evaluate the high-temperature corrosion behavior of iron- and nickel-base alloys in gas environments with a wide range of oxygen, sulfur, and carbon potentials, and (3) develop a systems approach based upon available thermodynamic and kinetic information so that possible corrosion problems in different coal-conversion processes can be evaluated.

1. Uniaxial Tensile Properties

The experimental program that involves the generation of uniaxial tensile data on four iron- and nickel-base alloys during exposure to the multicomponent gas environments has been discussed in detail in an earlier report.[6] Results of the initial corrosion experiments on Type 310 stainless steel, Incoloy 800, Inconel 671, and U. S. Steel Alloy 18-18-2 in the selected gas mixtures were reported earlier.[26] Uniaxial tensile data obtained for the four alloys in the as-received condition at temperatures of 750, 871, and 982°C were reported in the last quarterly report.[1] The 1000-h exposure of corrosion and uniaxial tensile specimens to gas mixture 1A at 750°C has been completed. The scale morphologies in the exposed specimens are being examined by means of scanning electron microscopy. Postexposure tensile tests of the specimens have conducted, and the results will be reported in the next quarterly. At present, the specimens are being exposed to gas mixture 1A at 871°C and to mixture 2A at 750°C. The specimens exposed to gas mixture 1A have accumulated 810 h and those in mixture 2A ∿320 h. The run at 871°C with gas mixture 1A, which was started in early October, is being repeated, since in the earlier run, a malfunction developed in the water-pump operation that resulted in extensive sulfidation of the reactor and specimens.

2. Oxidation-Sulfidation Behavior of Iron-Chromium-Nickel Alloys

The principal materials used in the elevated-temperature regions of coal-gasification and petrochemical processes are iron-base alloys with chromium as a major constituent. The gas environments in these processes are, in general, complex multicomponent mixtures that contain sulfur-bearing gases (H_2S and SO_2) in addition to oxidants (CO_2/CO and H_2O/H_2). The corrosion behavior of iron-base alloys in such complex environments is strongly influenced by the gas composition and temperature.[27,28] The corrosion rates can be significantly different, depending upon the mode of attack, i.e., sulfidation versus oxidation. Since the sulfide layers are, in general, not protective and have growth rates orders of magnitude larger than the oxide layers, it is beneficial to establish relationships between the mode of attack and the alloy composition, temperature, and gas composition.

The objective of the present work is to evaluate the oxidation-sulfidation rates of Fe and Fe-Cr-8Ni* alloys that contain 4, 12, and 22 wt % Cr (Table XI) at temperatures of 750 and 875°C as functions of oxygen and sulfur partial pressures in the gas environment.

3. Kinetic Behavior

The oxidation and sulfidation rates for different alloys were determined from the weight gain of test samples after specified times of exposure to gas mixtures that contained CO, CO_2, CH_4, H_2, and H_2S. The weight-gain data plotted versus the square root of exposure time showed straight-line behavior, which is indicative of parabolic kinetics for the corrosion process in these alloys. The parabolic rate constants k_p were determined for different alloy specimens as a function of exposure environment. Figures 28 and 29 show the variation in the parabolic rate constant as a function of alloy composition at 875 and 750°C, respectively. The figures show that, for a given sulfur potential, an increase in the oxygen partial pressure in the environment causes a decrease in the parabolic rate constant. The reaction rate constant for low-chromium (0-12 wt %) and high-chromium (>15 wt %) alloys can vary by approximately one and three orders of magnitude, respectively, by altering the composition of the gas mixture. These data also show that an increase in the chromium content of the alloy in the range 0-12 wt % increases the reaction rate; however, an additional increase in chromium concentration results in a decrease in the rate.

Figure 30 shows the temperature dependence of parabolic rate constants derived from data in the literature for oxidation[29-32] and sulfidation[33-38] of "pure" chromium. The parabolic rate constant for the oxidation of chromium is dependent upon the partial pressure of oxygen. The k_p value for chromium oxidation increases with an increase in oxygen pressure in the P_{O_2} range of 10^{-19} to 10^{-26} atm.[32] However, the values at low oxygen pressures are greater than those at $P_{O_2} \sim 0.1$ atm. The k_p values for chromium sulfidation vary by factors of 10 and 50 at temperatures of 750 and 875°C, respectively. The k_p values for chromium sulfidation, evaluated from the data of different investigators, do not show any systematic variation with sulfur pressure in the test environment. A range of k_p values can be assigned for chromium oxidation and sulfidation from the data in Fig. 30, and these values are shown in Figs. 28 and 29 for comparison with the rate data on Fe-Cr-8Ni alloys. The results show that the experimentally measured rates for the Fe-22Cr-8Ni alloy are lower than the rates for chromium sulfidation and are somewhat higher than those for chromium oxidation. Additional experimental work is needed to evaluate the effect of chromium content above 22 wt % in the alloy on the resistance to oxidation and sulfidation.

*All compositions are given in weight percent unless specified otherwise.

In general, the rates of oxidation and sulfidation are strongly influenced by the type of external scale (oxide versus sulfide) formed on the alloy, the adhesion of the scale to the base metal, and the internal oxidation or sulfidation of the less-noble elements in the base metal. Alloy additions such as manganese, silicon, and molybdenum diffuse rapidly through the base metal and segregate at the external scale/alloy interface, thus altering the adhesion characteristics of the scales. In the present work, Fe-Cr-Ni alloys with negligible concentration of elements such as Mn, Si, and Mo were used to evaluate the role of major alloying additions on the oxidation-sulfidation behavior of the materials.

4. Microstructural Observations

Figure 31 shows SEM photographs of samples of iron that were exposed to gas mixtures 1 and 3 (Table XII) for 25 h at 750 and 875°C. The x-ray image and the Fe and S distributions in the scale/alloy interface region of the samples were also obtained with an energy-dispersive x-ray analyzer attached to the SEM. The external scales in all samples were predominantly iron sulfide, which indicates that the sulfur potentials established in these experiments were higher than for the Fe/FeS equilibrium. For a 25-h exposure at 750°C, the thickness of the sulfide layer increased from 235 to 370 μm as the oxygen potential in the gas mixture decreased from 2.8×10^{-22} to 3.7×10^{-24} atm. For a 25-h exposure at 875°C, the thickness of the sulfide layer increased from 90 to 410 μm as the oxygen potential in the gas mixture decreased from 7.6×10^{-20} to 2.8×10^{-22} atm.

Figures 32-34 show the SEM photographs of Fe-Cr-8Ni alloy specimens that have been exposed to gas mixtures 1 through 3, respectively, for 5 and 25 h at 750°C. At oxygen and sulfur partial pressures that correspond to gas composition 1, the Fe-4Cr-8Ni and Fe-12Cr-8Ni alloys developed an external iron sulfide scale. The alloys also exhibited (Fe,Cr) sulfide particles in the interior of the specimens, predominantly in the intergranular regions of the specimens. In the same environment, the alloy that contained 22 wt % Cr developed a Cr-rich oxide scale with negligible internal sulfidation. A decrease in oxygen partial pressure in the gas mixture to values that correspond to gas mixtures 2 and 3 results in the formation of an outer scale layer of Fe or (Fe,Cr) sulfide with internal sulfide particles of Cr or (Fe,Cr) along the grain boundaries. In general, the thicknesses of the outer scale and internally affected layers were 30 to 50 times greater for the alloys that exhibited sulfidation when compared with the oxidation mode of interaction.

Figures 35-37 show SEM photographs of the cross sections of different Fe-Cr-8Ni alloy specimens that have been exposed to gas mixtures 1 through 3, respectively, for 5 and 25 h at 875°C. The photographs show that all the alloys, except those containing 22 wt % Cr exposed to mixture 1, developed an external scale of Fe or (Fe,Cr) sulfide and internal sulfide particles in the intergranular regions of the alloy specimens. The alloy with 22 wt % Cr developed a Cr-rich oxide scale upon exposure

to mixture 1. As before, the thicknesses of the external layers and internally affected zones were significantly greater when the alloys exhibited sulfidation rather than oxidation behavior in the gas environment.

Figures 32-37 also show that the effect of carbon activity (a_c) in the range 0.096-0.468 is strongly dependent upon the type of external scale formed in the specimens as well as the chromium content of the base metal. For example, when the alloys develop a Cr-rich oxide scale, as in the Fe-22Cr-8Ni alloy exposed at 750 and 875°C (Figs. 32 and 35), only internal sulfide particles were observed. On the other hand, when the alloys developed sulfide scales, internal carburization was virtually absent in alloys that contained 4 and 12 wt % Cr, and significant carburization in advance of the sulfidation front was observed in the 22 wt % Cr alloy specimens (Fig. 33). As the carbon activity is lowered, i.e., from mixture 1 to mixture 3, the extent of carburization in the 22 wt % Cr alloy specimens decreases, as evidenced by a much smaller volume fraction of carbides in the base metal ahead of the sulfidation front.

5. Discussion

The results obtained on the oxidation-sulfidation of Fe and Fe-Cr-Ni alloys showed that the scales formed during exposure to the mixed-gas environment were strongly adherent to the base metal. Before discussing the corrosion behavior and mechanisms of scale growth in these alloys, it is helpful to consider the thermodynamic conditions and kinetic factors that determine the types of phases which will form on the surfaces of the different alloys during exposure to multicomponent gas mixtures. Thermochemical diagrams, which depict the stability of the condensed phases for a given metal as functions of the thermodynamic activities of oxygen and sulfur in the gas mixture, can be used to examine the types of phases formed on the specimens in the present experiments. Figures 38 and 39 show the oxygen-sulfur thermochemical diagrams at 750 and 875°C, respectively, for Fe-Cr-8Ni alloys with chromium concentrations of 4, 12, and 22 wt %. The diagrams were developed from recent thermodynamic data for chromium oxide,[39] chromium sulfides,[35] and iron sulfide.[40] Also shown in these figures are the oxygen and sulfur partial pressures calculated from the gas mixtures used in different experiments; the environments are identified as 1, 2, and 3, which correspond to the same gas mixtures in Table XII. The thermochemical diagrams for the oxygen and sulfur partial pressures used in the experiments are such that the scale layers formed in Fe-Cr-8Ni alloys with 4 to 22 wt % Cr can be chromium oxide, a mixture of chromium and iron sulfides, or a combination of the three phases. The relative affinity of substitutional elements (e.g., Fe, Cr, and Ni) and reactive elements (e.g., O and S) as well as the relative growth rates of the reaction products (oxide versus sulfide) are important contributors to the establishmert of a specific phase in the scale layers of a given alloy. Based on the thermodynamic data for the Cr-Cr_2O_3 system, the chromium concentrations required for the formation of Cr_2O_3 are in the range from 0.003-0.2 wt %, since Cr_2O_3 is the only oxide phase in

equilibrium with an Fe-Cr-8Ni alloy at oxygen partial pressures between 7.6×10^{-20} and 2.8×10^{-22} atm at 875°C. The chromium concentrations that are needed at 750°C are 1-40 ppm for oxygen partial pressures (2.8×10^{-22} to 3.7×10^{-24} atm) used in the present experimental work. However, these chromium concentration values are insufficient to form a coherent film of Cr_2O_3. A similar calculation, based on $Cr\text{-}Cr_3S_4$ equilibrium, shows that chromium concentrations of $\sim$3 and 0.4 wt % are needed at 875 and 750°C, respectively, for the formation of Cr_3S_4 sulfide at the sulfur partial pressures used in the present experiments.

Thermodynamic considerations indicate that both Cr_2O_3 and Cr_3S_4 can form on all Fe-Cr-8Ni alloys used in the present investigation. The experimental results show that sulfide layers form in alloys containing 4 and 12 wt % Cr in all environments of the present study. In alloys with 22 wt % Cr, a thin oxide layer was observed on specimens exposed to mixture 1 at 750 and 875°C, and (Fe,Cr) sulfide layers were observed on specimens exposed to mixtures 2 and 3.

The preferential formation of *sulfide scales* in alloys that contained 4 and 12 wt % chromium can be explained on the basis of the *oxidation behavior* of these alloys. It is fairly well known that, in Fe-Cr and Ni-Cr alloys with $\lesssim$18 wt % Cr, the oxide layers which form are discontinuous, and the mode of interaction is internal oxidation.[41,42] In alloys with >20 wt % Cr, a continuous external layer of oxide has been observed. Wagner[43] and Rapp[44] examined the transition from internal to external oxidation of a less-noble element in an alloy. Wagner used the volume fraction of precipitated oxide as a parameter to determine whether the oxide will be formed as a continuous layer or as an internal precipitate and arrived at a critical volume fraction of oxide above which a continuous layer will be formed. The influence of low oxygen pressures (used in the present experiments) on the value of the critical volume fraction of oxide is not known, but a chromium concentration of 18 to 20 wt % will be required at temperatures of 750 and 875°C.

The present data show that an alloy with a composition of Fe-22Cr-8Ni produces oxide layers at higher P_{O_2} values (i.e., 7.6×10^{-20} atm at 875°C and 2.8×10^{-22} atm at 750°C) and forms (Fe,Cr) sulfide layers at lower P_{O_2} values (i.e., 3.6×10^{-21} and 2.8×10^{-22} atm at 875°C, and 1.6×10^{-23} and 3.7×10^{-24} atm at 750°C). This indicates an oxygen partial pressure in excess of that established by $Cr\text{-}Cr_2O_3$ equilibrium (at a given sulfur pressure) is required for the formation of a stable oxide layer. The ratios of oxygen partial pressures used in the experiments to those for $Cr_2O_3\text{-}Cr_3S_4$ equilibrium at the P_{S_2} values for different runs are listed in Table XIII. The experimental observations indicate that threshold oxygen partial pressure ratios for the formation of a continuous protective oxide layer on the Fe-22Cr-8Ni alloys at 875 and 750°C are $\sim 10^2$ and 10^3, respectively.

The kinetic data on the sulfidation of the alloys and the microstructural evaluation of the exposed specimens can be used to analyze the mechanisms of scale formation. In the Fe-4Cr-8Ni alloys, the scales

formed were predominantly iron sulfide and were independent of the composition of the gas environment. Since ferrous sulfide ($Fe_{1-x}S$) is a metal-deficient p-type semiconductor,[45] the migration of iron in the scale occurs via diffusion of cation vacancies and electron holes. The scale growth rate in these alloys is primarily controlled by the diffusion of ferrous ions. The chromium present in the alloy reacts with sulfur and forms either Cr sulfide or (Fe,Cr) sulfide spinel at the scale/alloy interface.

As the chromium concentration in an alloy increased to 12 or 22 wt %, the x-ray analyses of the exposed specimens showed the presence of Fe sulfide or (Fe,Cr) sulfide in the scale layers that depend on the gas composition. The scales in these specimens showed two or three zones (Figs. 32-37) and considerable porosity near the scale/alloy interface regions. The sulfidation behavior of the alloys in our experiments is in qualitative agreement with the results of earlier investigators.[35,46] The outer layer of scale grows by outward diffusion of iron ions and electrons from the substrate, and the transport of chromium in this layer is minimal. The formation of Cr-rich sulfides in the inner layer occurs via reduction of iron sulfide by chromium, which results in additional iron being transported to the outer layer for reaction with sulfur. Additional experimental work to determine the precise compositions of the phases formed as well as a knowledge of the diffusivities for different species is needed to establish the mechanisms of sulfidation in high-chromium alloys.

TABLE XI. Composition of Iron and Iron-Chromium-Nickel Alloys (Concentrations are in wt %)

Alloy	Cr	Ni	C	N	O	Fe
Fe	<0.004	0.012	0.002	0.001	<0.007	Bal[a,b]
Fe-4Cr-8Ni	3.89	7.86	0.004	<0.001	0.010	Bal[a]
Fe-12Cr-8Ni	11.96	7.96	0.003	<0.001	0.012	Bal[a]
Fe-22Cr-8Ni	21.86	7.92	0.003	0.002	0.009	Bal[a]

[a]Bal indicates balance; spectrographic analyses for Mn, Mo, Si, Nb, Ti, Zr, V, Co, and Cu indicated <0.01 wt %.

[b]Manganese concentration in high-purity iron was 0.05 wt %.

TABLE XII. Reaction Potentials Established in Different Experimental Runs

Temperature, °C	Gas Identification Number	Gas Composition, vol %					Reaction Potentials[a]		
		CO	CO_2	H_2	CH_4	H_2S	P_{O_2}, atm	P_{S_2}, atm	a_c
875	1	20.2	8.9	67.4	3.1	0.4	7.6×10^{-20}	2.8×10^{-8}	0.226
	2	3.4	1.5	94.1	0.5	0.56	3.6×10^{-21}	3.2×10^{-8}	0.181
	3	0.6	0.3	98.5	0.1	0.58	2.8×10^{-22}	3.2×10^{-8}	0.096
750	1	23.9	10.0	61.5	3.7	0.36	2.8×10^{-22}	3.2×10^{-9}	0.468
	2	1.9	0.8	96.4	0.3	0.57	1.6×10^{-23}	3.4×10^{-9}	0.180
	3	0.7	0.3	98.3	0.1	0.58	3.7×10^{-24}	3.2×10^{-9}	0.096

[a]The oxygen partial pressures for Fe/FeO equilibrium at 875 and 750°C are 1.2×10^{-17} and 6.7×10^{-21} atm, respectively. The sulfur partial pressures for Fe/FeS equilibrium at 875 and 750°C are 5.4×10^{-9} and 1.2×10^{-10} atm, respectively.

TABLE XIII. Ratios of Oxygen Partial Pressures Used in the Experiments to Those Calculated from $Cr-Cr_2O_3$ Equilibrium for an Fe-22Cr-8Ni Alloy

Temperature, °C	p_{S_2}, atm	$p_{O_2}^e$ at $Cr-Cr_2O_3$ Equilibrium, atm	Ratios of $p_{O_2}/p_{O_2}^e$		
			Mixture 1	Mixture 2	Mixture 3
875	$\sim 3 \times 10^{-8}$	3.2×10^{-22}	240 Oxide	11 Sulfide	0.9 Sulfide
750	$\sim 3.2 \times 10^{-9}$	1.6×10^{-25}	1800 Oxide	100 Sulfide	23 Sulfide

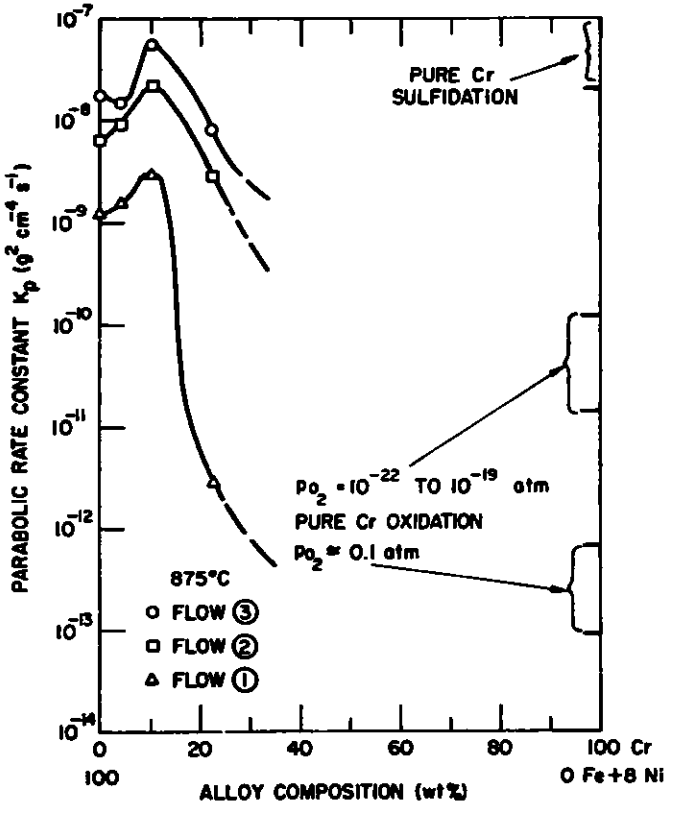

Fig. 28. Variation of Parabolic Rate Constant as a Function of Chromium Content in Fe-Cr-8Ni Alloys at 875°C. ANL Neg. No. 306-77-91 (Revised).

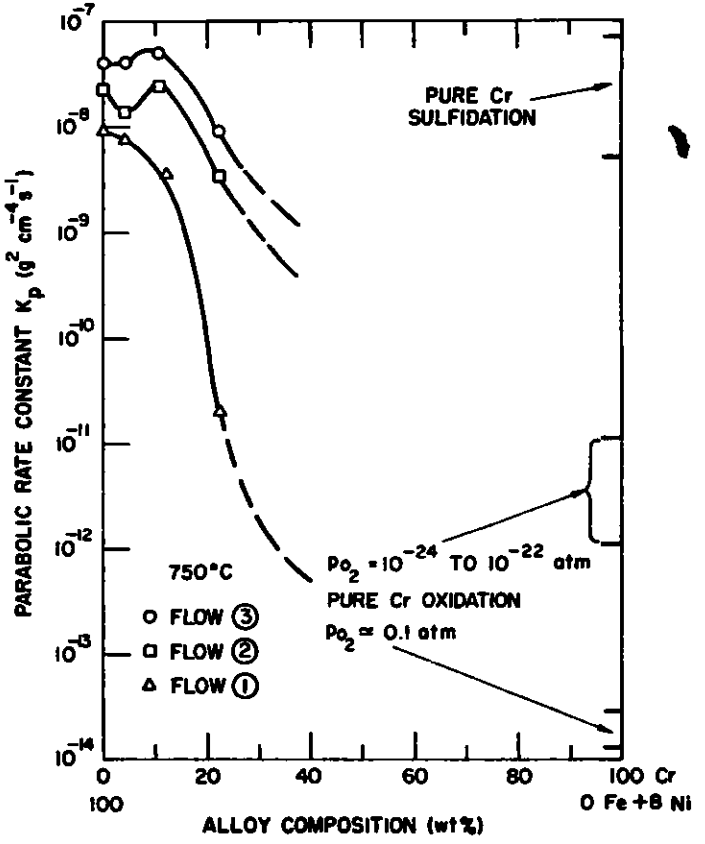

Fig. 29. Variation of Parabolic Rate Constant as a Function of Chromium Content in Fe-Cr-8Ni Alloys at 750°C. ANL Neg. No. 306-77-192 (Revised).

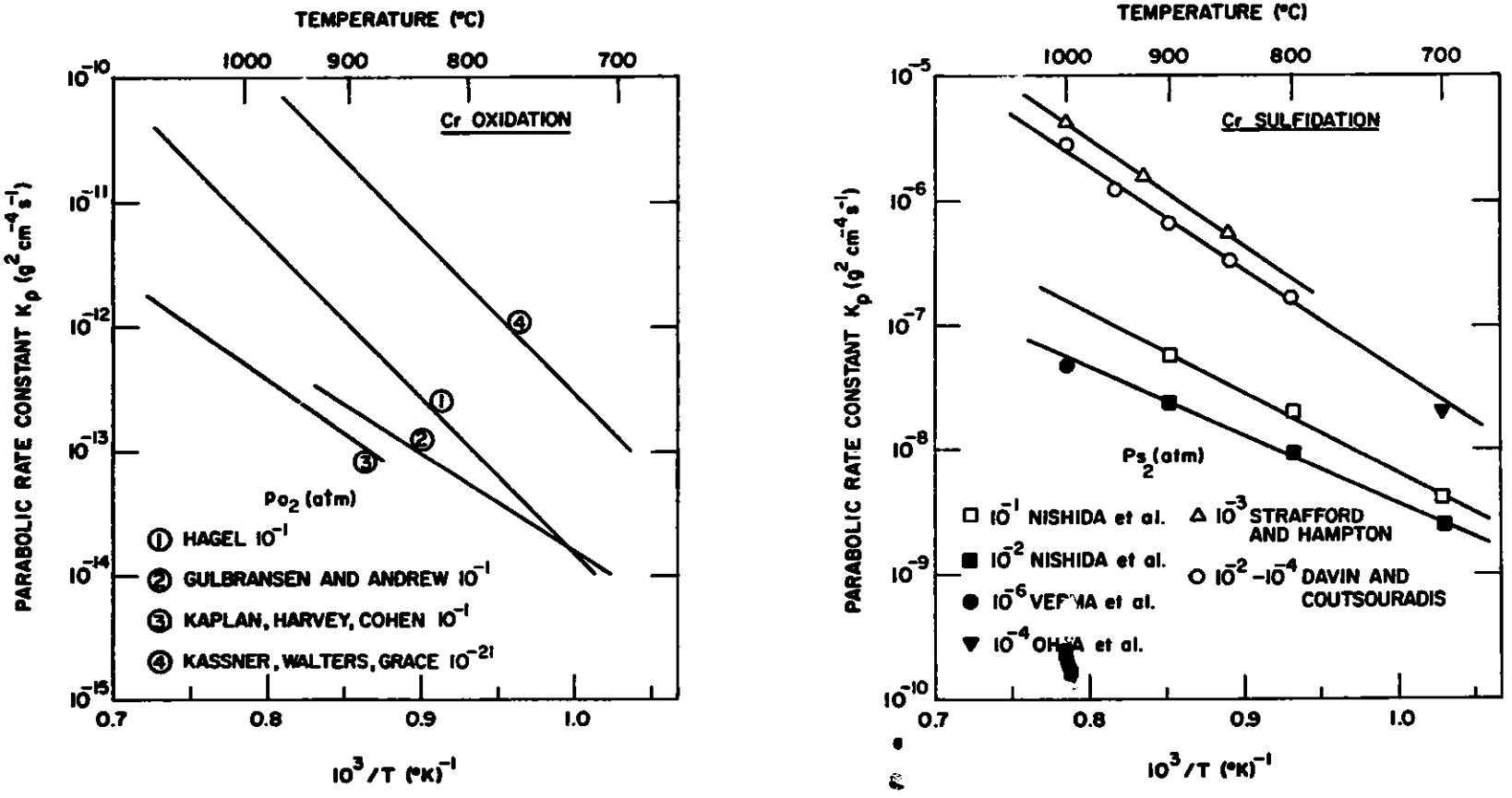

Fig. 30. Temperature Dependence of Parabolic Rate Constants for Oxidation and Sulfidation of "Pure" Chromium. ANL Neg. No. 306-77-195 (Revised).

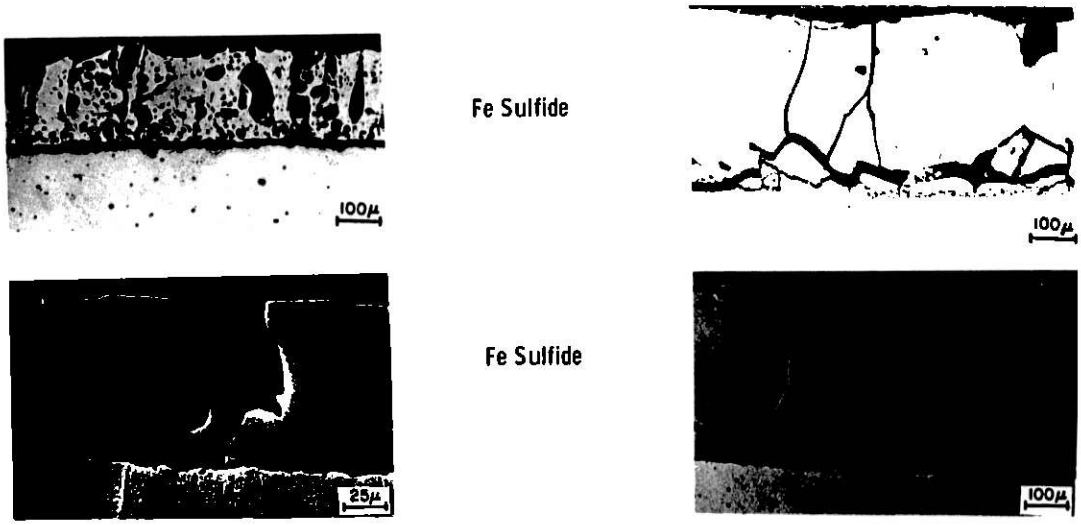

Fig. 31. SEM Photographs of Cross Sections of Iron Specimen after 25-h Exposure to Gas Mixtures 1 and 3 (Table XII). Neg. No. MSD-64095.

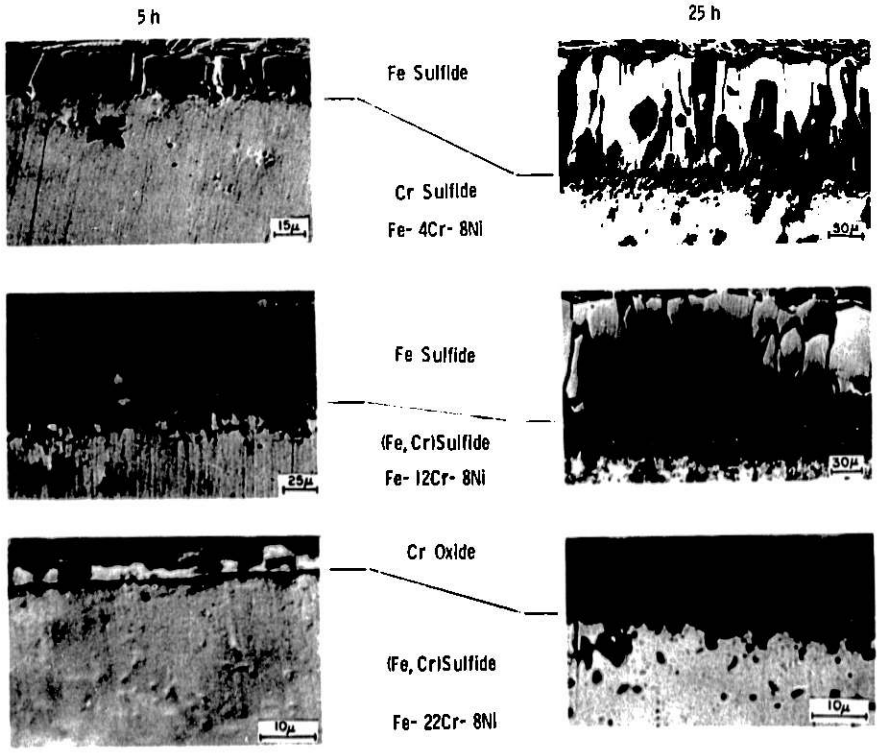

Fig. 32. SEM Photographs of Cross Sections of Fe-Cr-8Ni Alloys with 4, 12, and 22 wt % Cr after Exposure at 750°C to Gas Mixture 1. Left, 5 h; right, 25 h. Neg. No. MSD-64093.

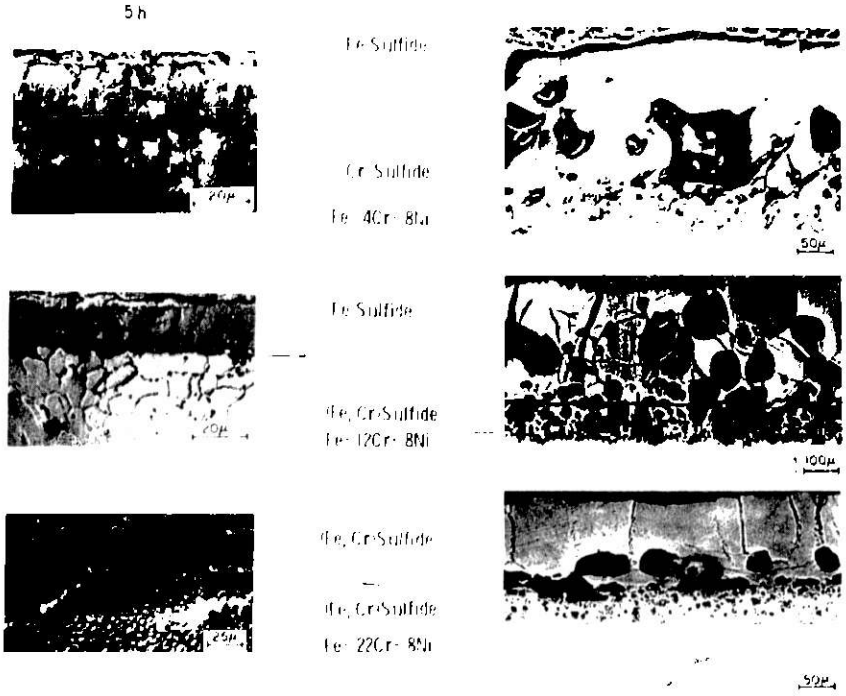

Fig. 33. SEM Photographs of Cross Sections of Fe-Cr-8Ni Alloys with 4, 12, and 22 wt % Cr after Exposure at 750°C to Gas Mixture 2. Left, 5 h; right, 25 h. Neg. No. MSD-64096.

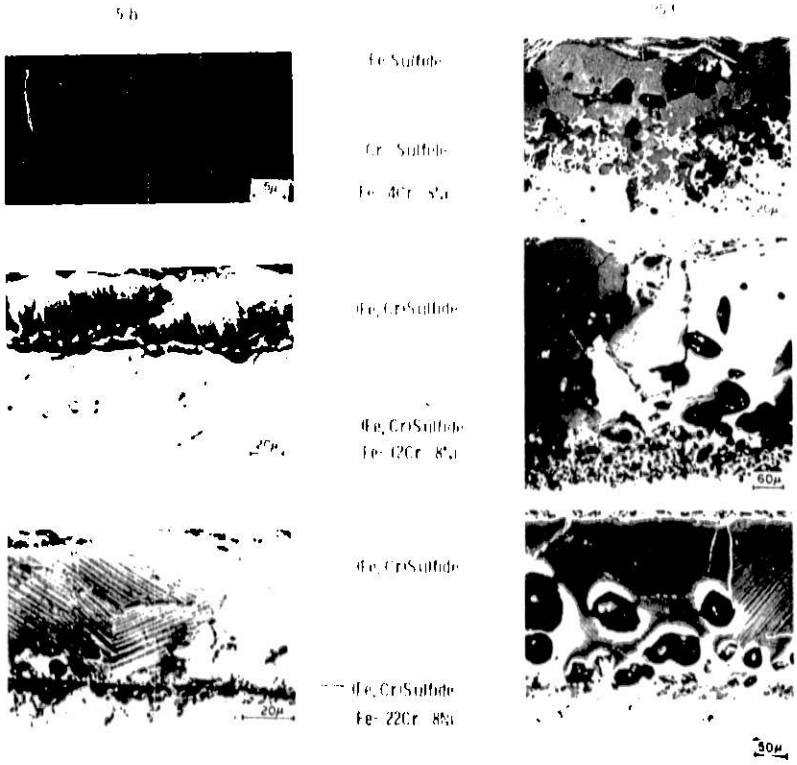

Fig. 34. SEM Photographs of Cross Sections of Fe-Cr-8Ni Alloys with 4, 12, and 22 wt % Cr after Exposure at 750°C to Gas Mixture 3. Left, 5 h; right, 25 h. Neg. No. MSD-64090.

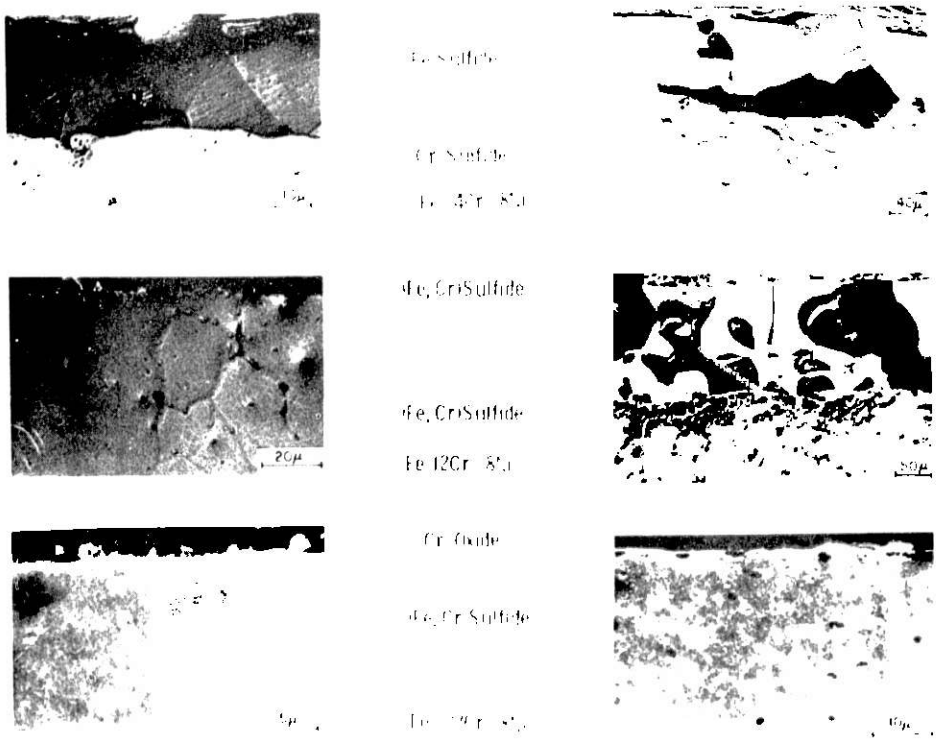

Fig. 35. SEM Photographs of Cross Sections of Fe-Cr-8Ni Alloys with 4, 12, and 22 wt % Cr after Exposure at 875°C to Gas Mixture 1. Left, 5 h; right, 25 h. Neg. No. MSD-64091.

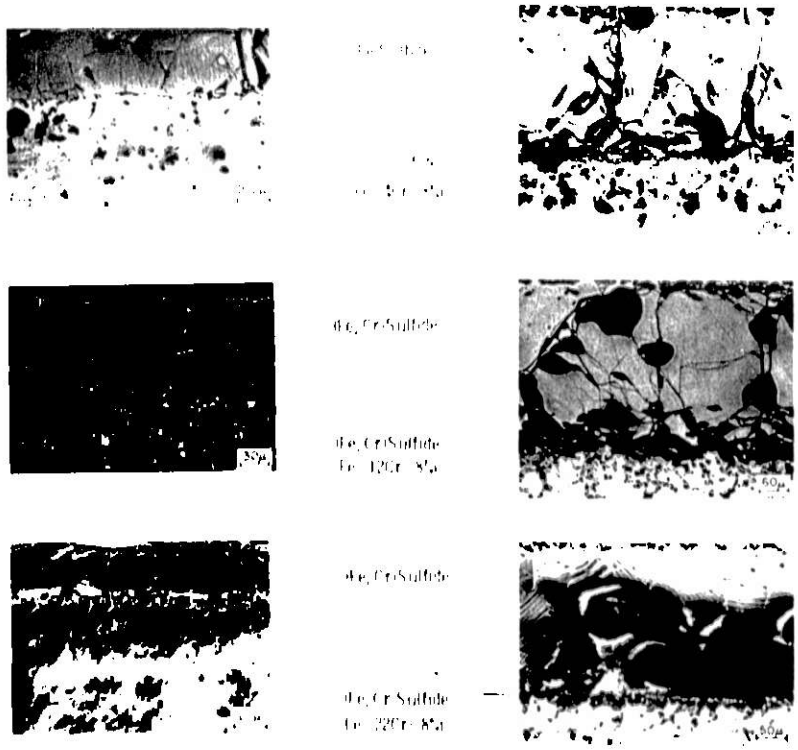

Fig. 36. SEM Photographs of Cross Sections of Fe-Cr-8Ni Alloys with 4, 12, and 22 wt % Cr after Exposure at 875°C to Gas Mixture 2. Left, 5 h; right, 25 h. Neg. No. MSD-64092.

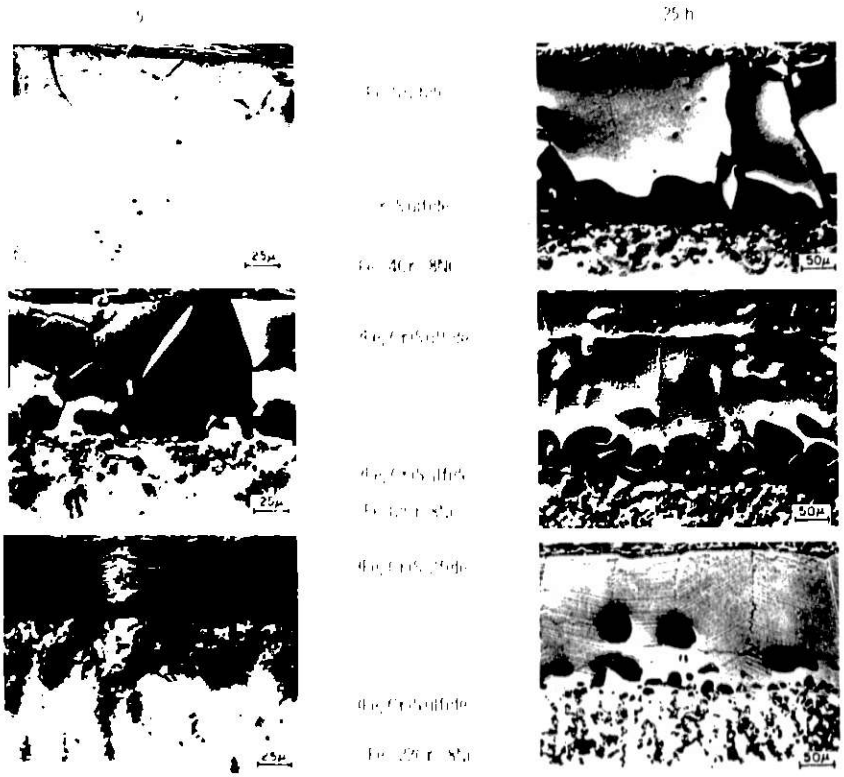

Fig. 37. SEM Photographs of Cross Sections of Fe-Cr-8Ni Alloys with 4, 12, and 22 wt % Cr after Exposure at 875°C to Gas Mixture 3. Left, 5 h; right, 25 h. Neg. No. MSD-64094.

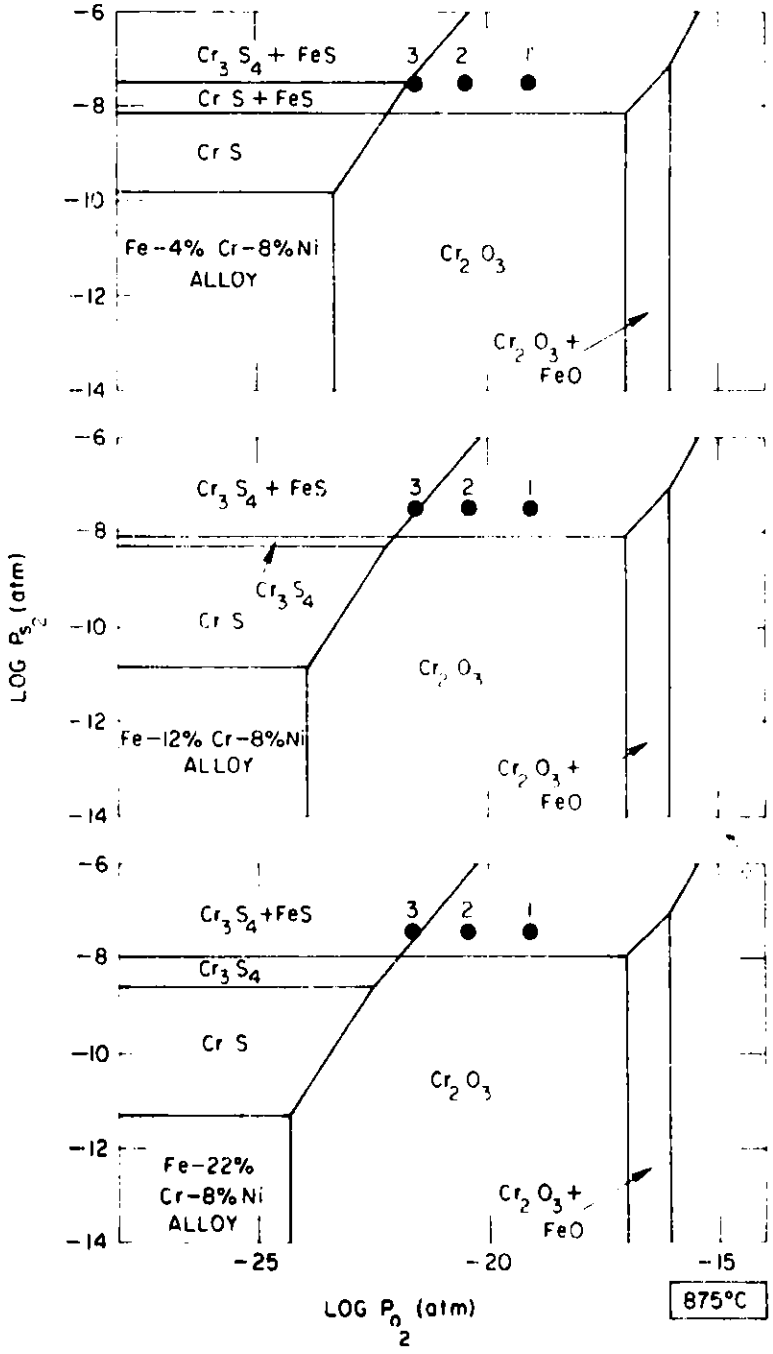

Fig. 38. Oxygen-Sulfur Thermochemical Diagram for Fe-Cr-8Ni Alloys with 4, 12, and 22 wt % Cr at 750°C. The gas environments used in the experimental program are indicated by 1, 2, and 3. Neg. No. ANL 306-77-193.

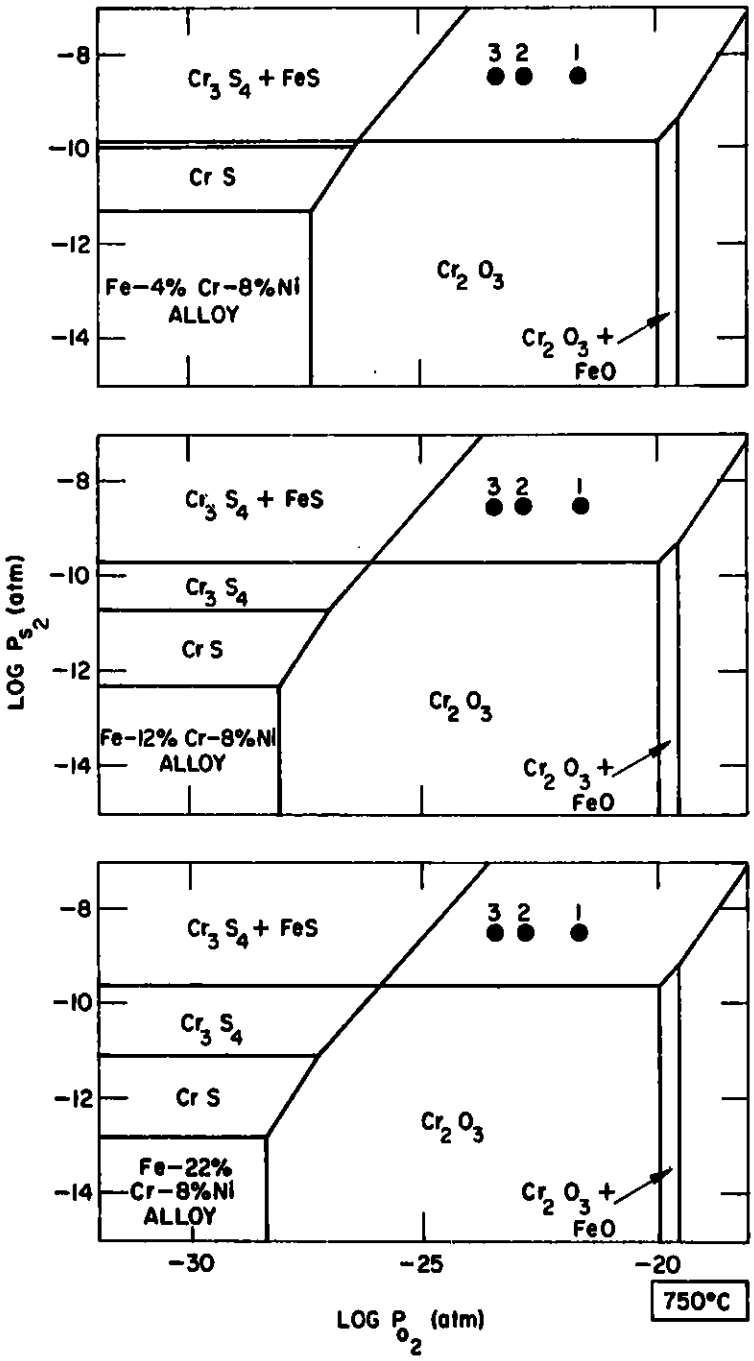

Fig. 39. Oxygen-Sulfur Thermochemical Diagram for Fe-Cr-8Ni Alloys with 4, 12, and 22 wt % Cr at 875°C. The gas environments used in the experimental program are indicated by 1, 2, and 3. Neg. No. ANL 306-77-194.

Task E -- Erosion Behavior of Materials in Coal-conversion Processes
(W. J. Shack and J. Y. Park)

The erosion-testing apparatus built by Solar Corporation under a subcontract from ANL was received. The apparatus consists of a motor-driven rotating slinger arm and a belt-feed mechanism in a sealed test chamber, which permits operation at elevated temperatures and controlled atmospheres. After examination, it was apparent that substantial repairs and modifications were necessary before a test program could be undertaken. To date, the following repairs have been made: the rotor shaft for the slinger arm was straightened, a cracked refractory liner was removed, and a new cooling coil was installed. To improve the reliability of the apparatus during long-term tests, the design of the bearing and the bearing seal of the slinger rotoshaft is also being modified. In the next quarter, additional repairs and modifications will be made, and the apparatus will be reassembled for initial checkout.

Task F -- Component Performance and Failure Analysis *(S. Danyluk and G. M. Dragel)*

The activity during this quarter involved the examination of components from the HYGAS Pilot Plant, the Institute of Gas Technology Steam-Iron System for Hydrogen Production Pilot Plant, and the Synthane Pilot Plant. The results of these analyses are summarized below.

1. Pump Shaft and Capscrew Failure (GA-207) (Synthane Pilot Plant)

A 3.18-cm (1.25-in.)-diam AISI Type 4140 steel shaft and an AISI Type 4037 steel capscrew from water pump GA-207 failed by complete separation after ∿500-800 h operation. The pump circulates high-temperature water between the Venturi scrubber and the scrubber surge tank at the Synthane Pilot Plant. A replacement capscrew, Type 4037 steel, also failed by shear after a shorter operating time (2.5-5 h). A schematic of the pump shaft, capscrew, impeller, and failure locations is shown in Fig. 40. Figure 41 shows the fracture and machined surface of the shaft and a fractured capscrew. Both failures are associated with fatigue. The probable failure sequence is as follows (this sequence is essentially unchanged from what was hypothesized by Synthane personnel):

(a) The capscrew fractured by fatigue and surface defects provided the initiation sites for the crack. Laboratory investigation confirmed the capscrew manufacturer's suspicions that the capscrews were improperly heat treated during production. Vickers hardness numbers of ∿490 kg/mm^2 were recorded, which are higher than the Vickers values of 220-310 kg/mm^2 specified after tempering from 200-650°C.

(b) The shaft, still engaged to the impeller through the keyway, began to slide after the capscrew failed and was subjected to a torsional load due to this slippage and carbon fine buildup on the impeller.

(c) A fatigue crack initiated at the keyway fillet radius (Fig. 42). The radius is smaller (0.021 cm) than what is normally recommended practice (0.067 cm),[47,48] and a stress riser is present. Although the increase in stress due to the radius of curvature of the fillet alone would not cause the failure, this stress would aggravate and intensify any existing overload condition and might be expected to lead to crack initiation at the keyway fillet.

(d) The fatigue crack propagated toward the center threaded hole and branching of the fillet crack occurred (Fig. 43). A catastrophic failure occurred shortly thereafter and the shaft broke in two.

Using the fatigue-striation-spacing measurement at the shaft fracture surface, the upper limits on the number of revolutions for complete separation to occur is 15,000-70,000 revolutions. Since the shaft rotates at 3600 rpm, the crack propagated through the shaft diameter within an hour. This estimate and the fact that the shaft fracture surface was shiny support the conclusion that the shaft failed a short time after the capscrew failed.

The recommendations were (a) the capscrew must be properly heat treated so that this component possesses the proper toughness, and (b) the fillet radius should be machined to a value prescribed by standard engineering practice. Byron Jackson, the pump manufacturer, has implemented a design change at the capscrew end of the shaft. The OD of the shaft will be threaded and attached to the impeller with a nut. This design change and proper heat treatment of the components should alleviate further problems.

A final report of this analysis will be distributed in the coming quarter.

2. Welded "Tee" Fitting from the Char Carrier Line (HYGAS Pilot Plant)

A welded Type 316 stainless steel "Tee" fitting from the char carrier line, developed cracks on the internal surfaces. The fitting was part of the original installation of the HYGAS Pilot plant, and the estimated time of service is ∿6 years. The char carrier line carries steam at a pressure of 6.8 MPa and a temperature of 260°C (1000 psig, 500°F), with occasional hot gas at 870°C (1600°F), from the steam-oxygen zone of the gasifier for relatively short periods of time <600s (<10 min). The preliminary failure analysis was carried out by the AMOCO Research Center, Naperville, Illinois, and it was deduced that thermal shock was the probable cause of crack initiation. The ANL analysis confirmed this diagnosis. The cracks were most probably caused by overheating to ∿760°C (∿1400°F) and rapid cooling to 260°C (500°F) with nitrogen.

3. Tubing from Line 322 in the Second-stage Gasifier Reactor (HYGAS Pilot Plant)

A 7.5-cm (3-in.) OD, Schedule 40 Incoloy 800 pipe that was part of line 322 in the second-stage gasifier reactor at the HYGAS Pilot Plant developed cracks at the ID after ∿1.5-2 years of service. A 67.5-kg (150-lb) AISI Type 316 stainless steel flange was welded to each end of the pipe. The pipe transports char and gas at 815°C (1500°F) with a nominal gas composition of 72% H_2O, 9% H_2, 9% CH_4, 4% CO, 3% CO_2, 3% N_2, <1% H_2S. A fracture and complete break of the pipe occurred immediately adjacent to the OD weld of the upper flange. This fracture was not examined.

The cracks at the ID surface were numerous, and a cross section of one of the cracks is shown in Fig. 44. As can be seen, this crack is initially intergranular and, as it progressed, the mode changed to transgranular. This change in mode may be due to an increase in the effective stress as the depth of the crack increases, chemical effects at the ID (carburization), or chemical changes at the crack tip.

4. Pit Formation at Thermowells (Synthane Pilot Plant)

Pits found at the OD of a Hastelloy C-276 thermowell located above the distributor cone in the Synthane gasifier were reported in a previous quarterly report.[1] The thermowell is constructed from a 47.5-mm-diam tube with a 5-mm wall thickness. An endplug is welded on the tube end that is inserted into the gasifier. Pitting was observed along the length of the thermowell but was considerably more severe in the weld region. Plant personnel suspected that clinker was in contact with the OD of the thermowell and therefore were concerned that the pitting might lead to premature failure of the thermowell. A photograph of the OD of the thermowell and a micrograph of a polished and etched section containing the tube and endcap are shown in Fig. 45. Severe pitting can be observed in the weld region. The micrograph shows the endplug, weld metal and tube, oxide scale, and pitted regions. The microstructure of the endplug appears different from the tube. The chemical analyses of the tube and endplug are shown in Table XIV. Some chemical differences are evident between these two materials, notably cobalt, vanadium, and silicon, although the concentrations fall within the manufacturer's specification. The conclusions of this investigation are that clinker deposition caused the pitting, and the more severe pitting at the endplug was caused by the difference in chemistry of the endplug and heavier clinker deposition.

It was recommended that the chemistry of the endplug be checked prior to replacement. The thermowell was recapped with a Hastelloy C-276 endplug and is now ∿51 cm shorter than the original length. Since the thermowell is shorter, the possibility for clinker formation has been decreased.

5. Internal Cyclone from the Ash-agglomerating Gasifier (HYGAS Pilot Plant)

A Type 310 stainless steel internal cyclone from the Ash-agglomerating Gasifier (AAG) of the HYGAS pilot plant developed a perforation at an angle of ∿20-30° relative to the inlet axis of the cyclone at the wall of the internal shell. The total service time was ∿20 days. The particle-size loading for the cyclone is 100-0 mesh, with an average gas inlet velocity of 120-160 ft/s. The system was operated with coke for three cycles (5-7 days/cycle) and coal for one cycle (3-5 days/cycle). A photograph of the cyclone with the perforation is shown in Fig. 46.

The failure is attributed to erosion due to solid-particle impingement. The recommendation, at present, is to fabricate an insert of Haynes Stellite Alloy 6B in the eroded section and/or to reduce the particulate velocity. Additional investigation will be conducted in the coming quarter to deduce the erosion rate and spacial variation. These data will provide input to Task E of this project.

6. Chloride-assisted Stress-corrosion Cracking in Type 316 Stainless Steel Tubing (HYGAS Pilot Plant and Steam-Iron Plant for Hydrogen Production)

Leaking cracks were observed in 1.27- and 0.64-cm Type 316 stainless steel tubes that were steam traced, insulated, weather stripped, and exposed to the weather. In two cases, 1.27-cm (0.5-in.) OD tubes (labeled LT-342 and LT-477) transport high-pressure city water and are in the vicinity of the main gasifier section of the HYGAS Pilot Plant. A third tube, 0.64-cm (0.25-in.) OD, was used as a gas-sample line and is attached to the upper reducer section of the Steam-Iron reactor. In all three cases, the tubes are pressurized and operate at specified nominal temperatures of 150-200°C. The cracks occurred predominantly near bends, and were branched and transgranular. The cracks originated at the OD in tubes LT-342 and No. 6411 and at the ID in tube LT-477. Figure 47 is a photograph of gas-sampling line No. 6411. Circumferential cracks are visible, and some expansion has occurred as a result of internal pressure. Figure 48 shows a typical cross section of tube No. 6411. The cracks are transgranular and branched and are due to chloride-assisted stress-corrosion cracking.

The chlorides were attributed to the asbestos insulation used in weather stripping tubes LT-342 and No. 6411. Chlorides were leached by occasional drenching in city water and exposure to the weather. City water was the most probable source of chlorides in the failure of tube LT-477. Stresses were provided by the internal pressure and residual stresses at bends in the tubes. The following recommendations were suggested:

(a) The replaced insulation should contain a lower soluble chloride content.

(b) The tube material should be changed to an alloy that is more resistant to chloride stress-corrosion cracking. Nonsensitized Incoloy 800 is a reasonable choice.

(c) The occasional drenching by city water should be avoided.

A final report on this analysis will be issued in the coming quarter.

TABLE XIV. Composition of Hastelloy C-276

Element	Manufacturer's Nominal Specification, wt %	Chemical Analysis (Wet Method),[a] wt %	
		Tube	Endplug
Silicon	0.05	0.02	0.09
Manganese	1.0	0.43	0.41
Total Carbon	0.02	0.008	0.007
Phosphorous	0.03	0.010	0.009
Sulfur	0.03	0.012	0.005
Nickel	Balance	58.16	58.60
Chromium	15.5	15.16	15.29
Molybdenum	16.0	14.50	14.30
Iron	4-7	5.80	5.60
Aluminum	-	0.13	0.18
Colbalt	2.5	0.48	1.02
Columbium/Tantallum	-	<0.05	<0.05
Titanium	-	<0.01	0.02
Tungsten	3.8	3.72	3.54
Vanadium	0.35	0.06	0.19

[a]Analysis performed by Charles A. Kawin Company, 2671 Gardner, Broadview, Illinois 60153.

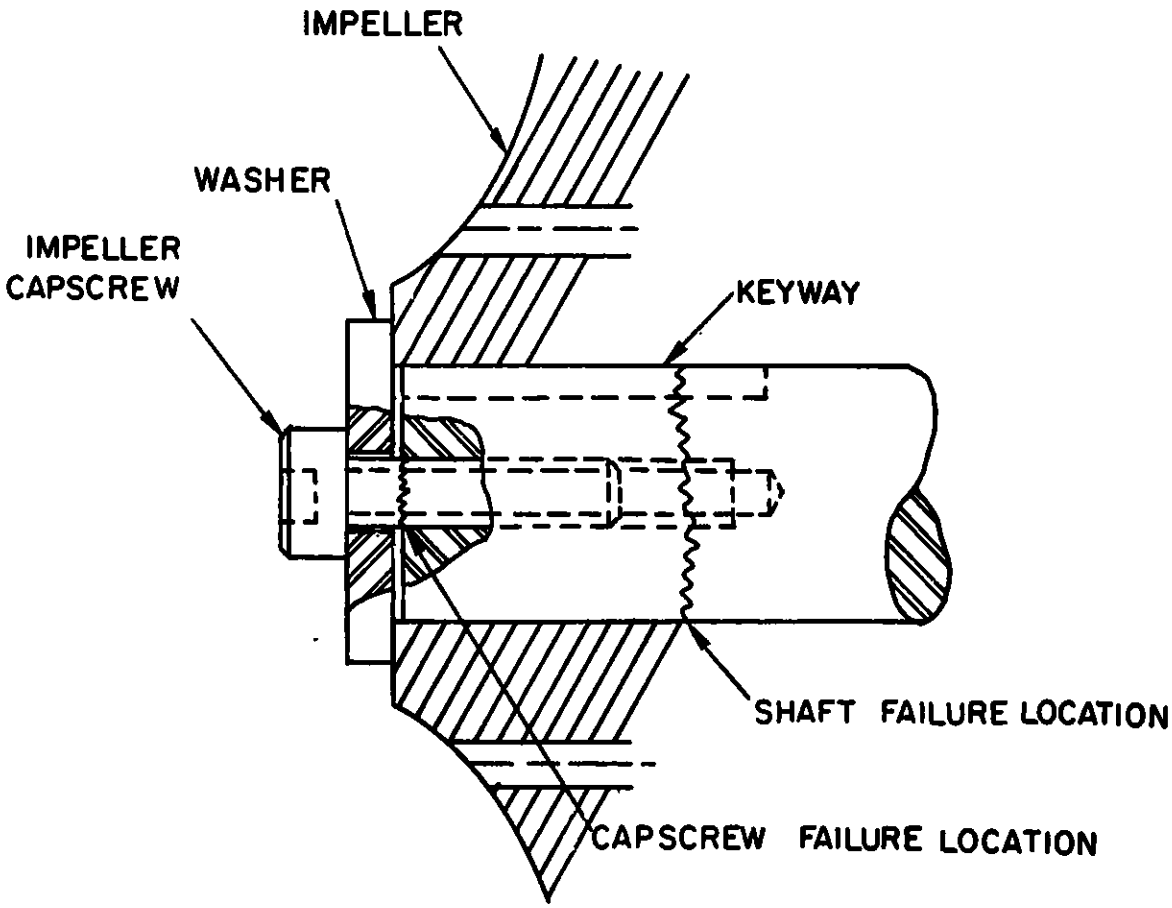

Fig. 40. Schematic of the Pump Shaft and Capscrew from the Venturi Scrubber Recycle Water Pump GA-207 at the Synthane Plant. ANL Neg. No. 306-77-406 (Revised).

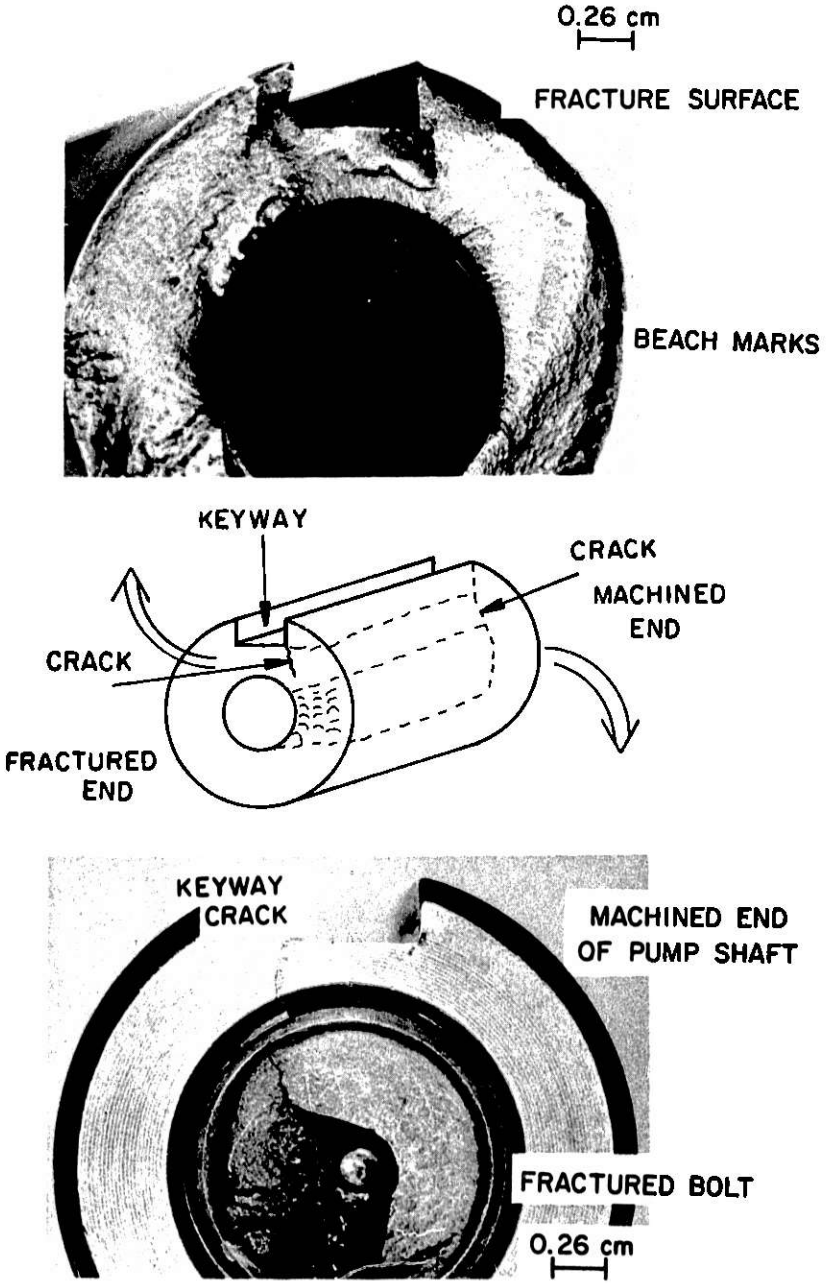

Fig. 41. The Fracture and Machined Surface of the Pump Shaft. The keyway crack is visible in the photographs. ANL Neg. No. 306-78-43.

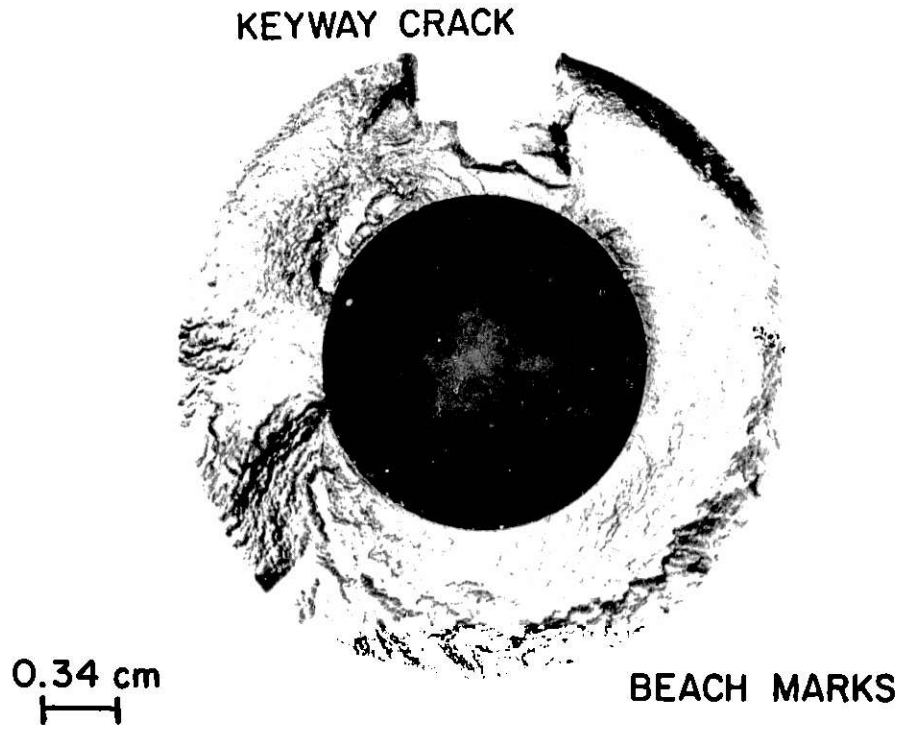

Fig. 42. Cross Section of the Shaft Showing the Morphology of the Fractured Surface and Crack in the Keyway. ANL Neg. No. 306-78-44.

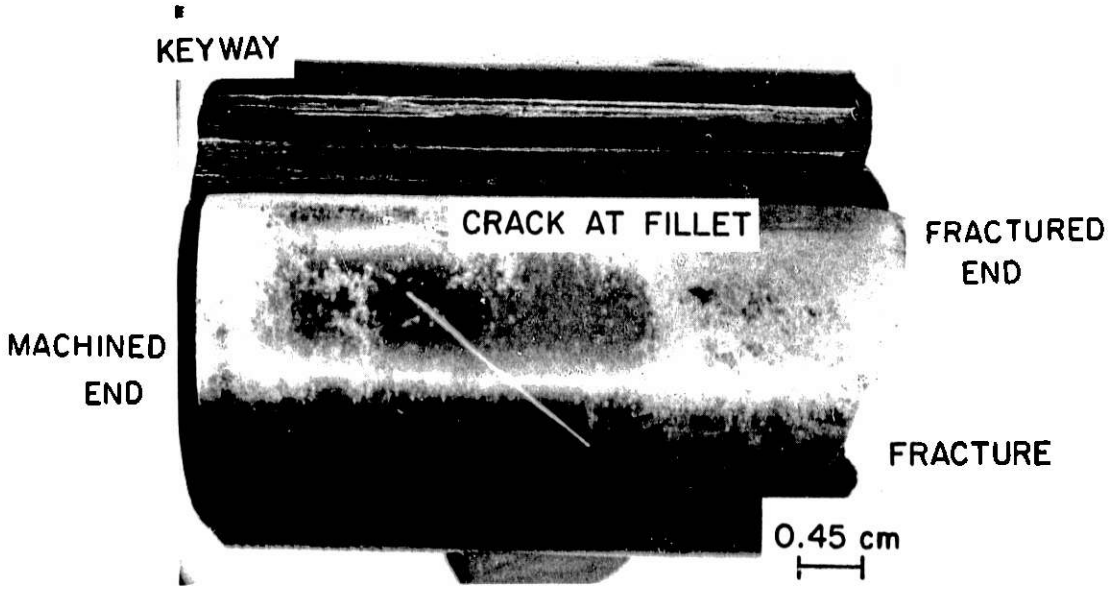

Fig. 43. Photograph of a Fillet in the Keyway Showing a Crack Extending along the Length of the Keyway. ANL Neg. No. 306-78-45.

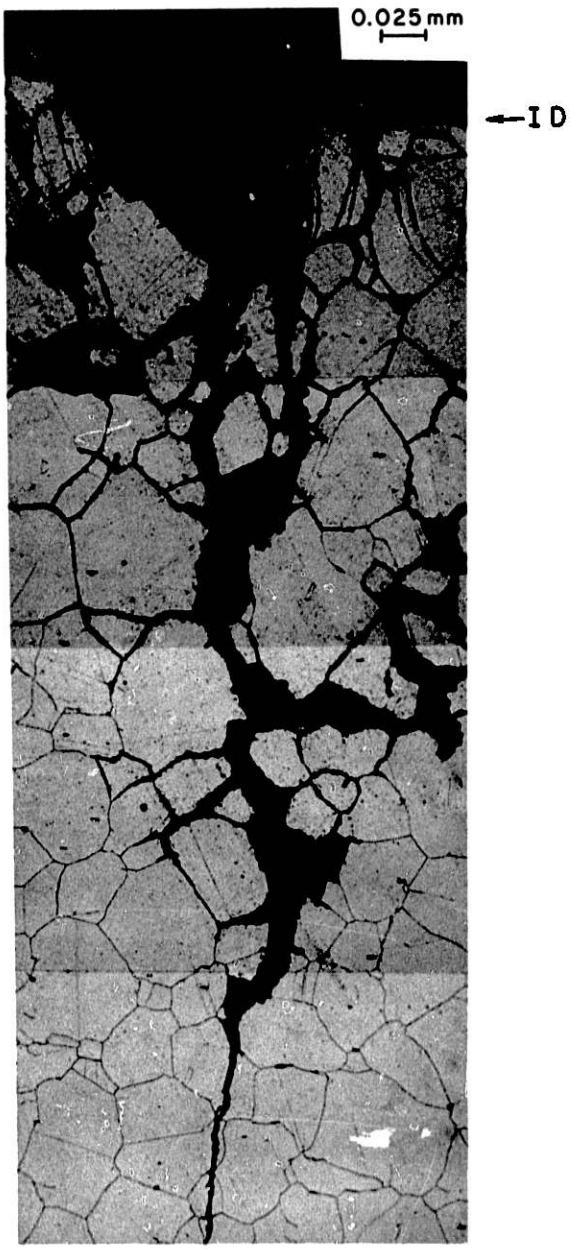

Fig. 44. Crack That Had Initiated at the ID of Line 322 in the Second-stage Gasifier Reactor from the HYGAS Pilot Plant. The material is Incoloy 800 and the crack mode changes from intergranular to transgranular. ANL Neg. No. 306-78-62.

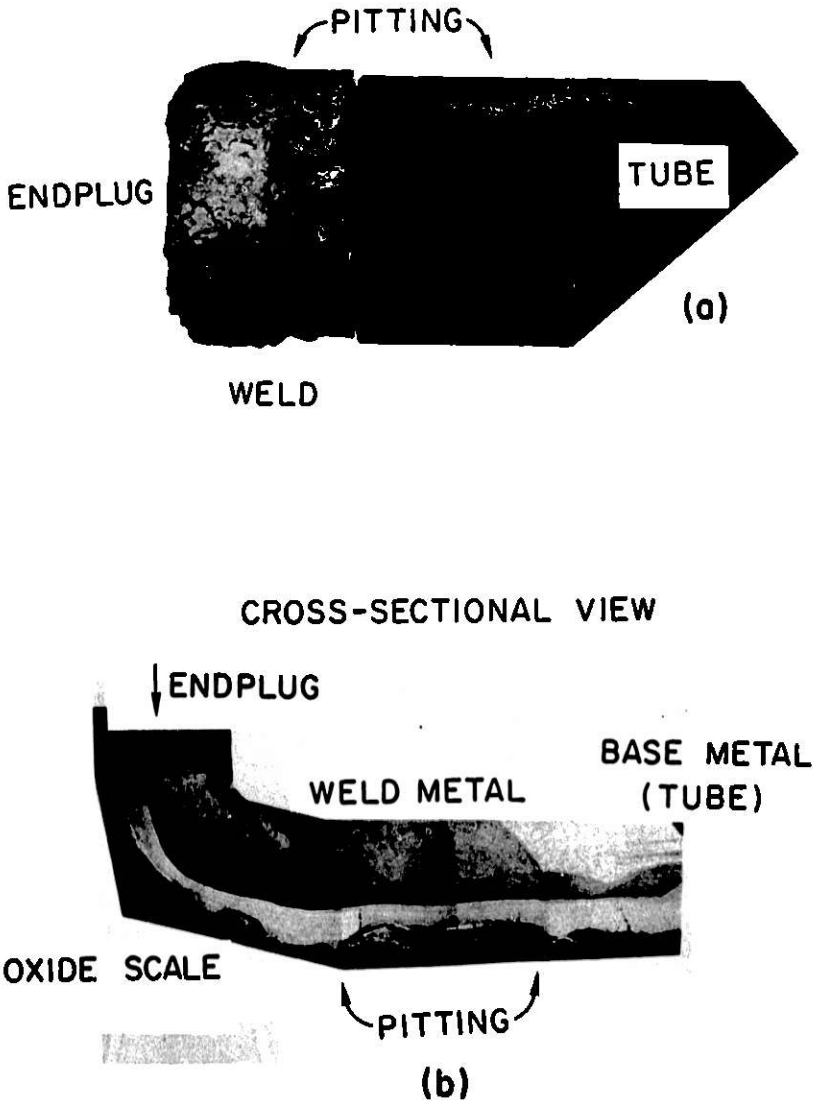

Fig. 45. Hastelloy C-276 Thermowell from the Synthane Pilot Plant. The OD (a) and etched cross section (b) containing the endplug, weld metal, and tube are shown. Neg. No. ANL 306-78-42.

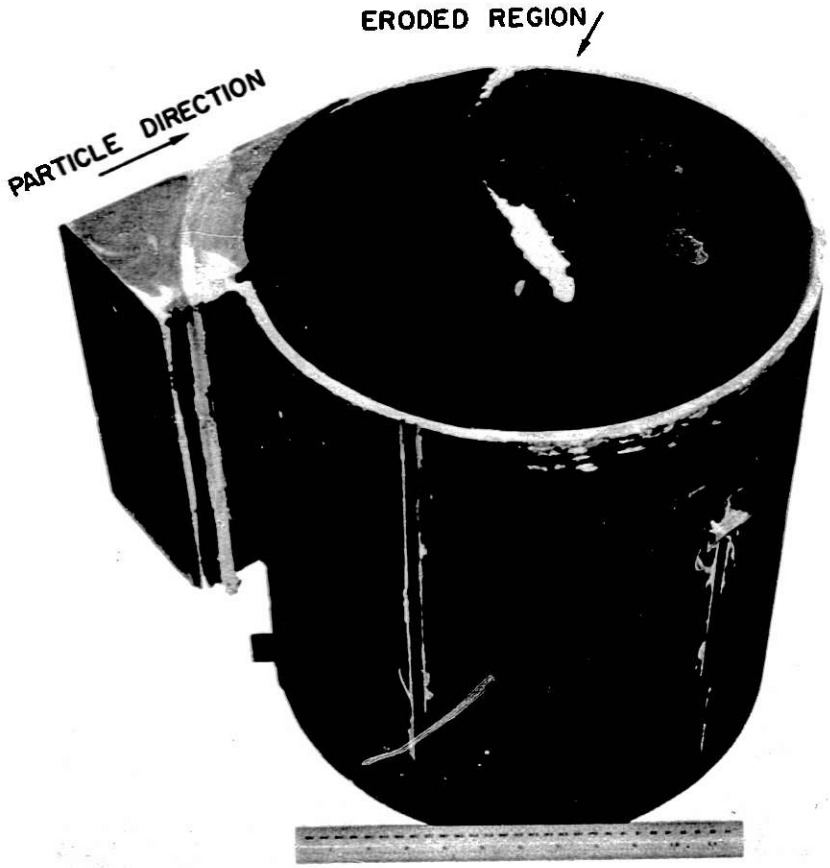

Fig. 46. Internal Cyclone from the Ash-agglomerating Gasifier of the HYGAS Pilot Plant. The internal shell and the perforation are visible. ANL Neg. No. 306-77-543 (Revised).

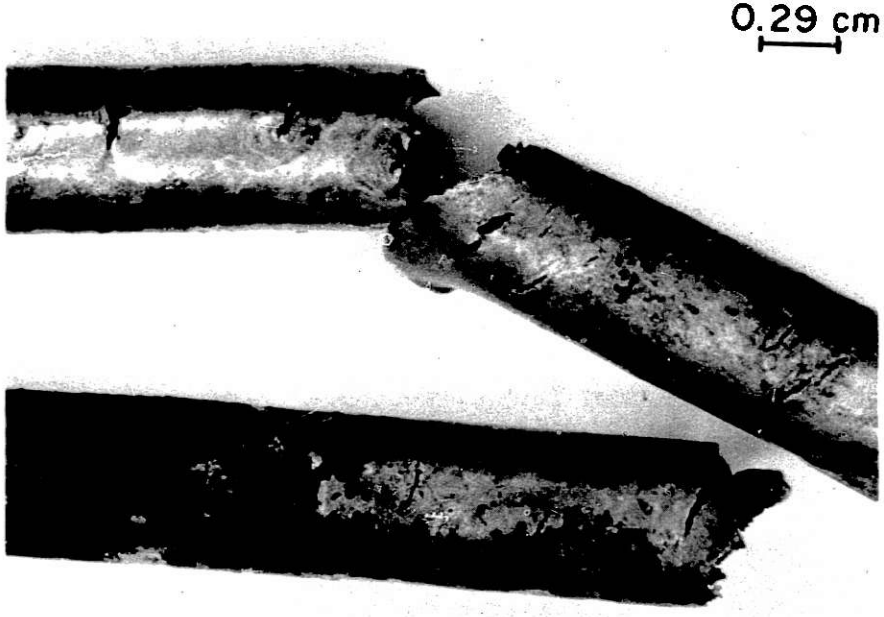

Fig. 47. Extensive Cracking at the OD of Line 6411. Circumferential cracks are seen. Some expansion of the cracks is seen. ANL Neg. No. 306-78-61.

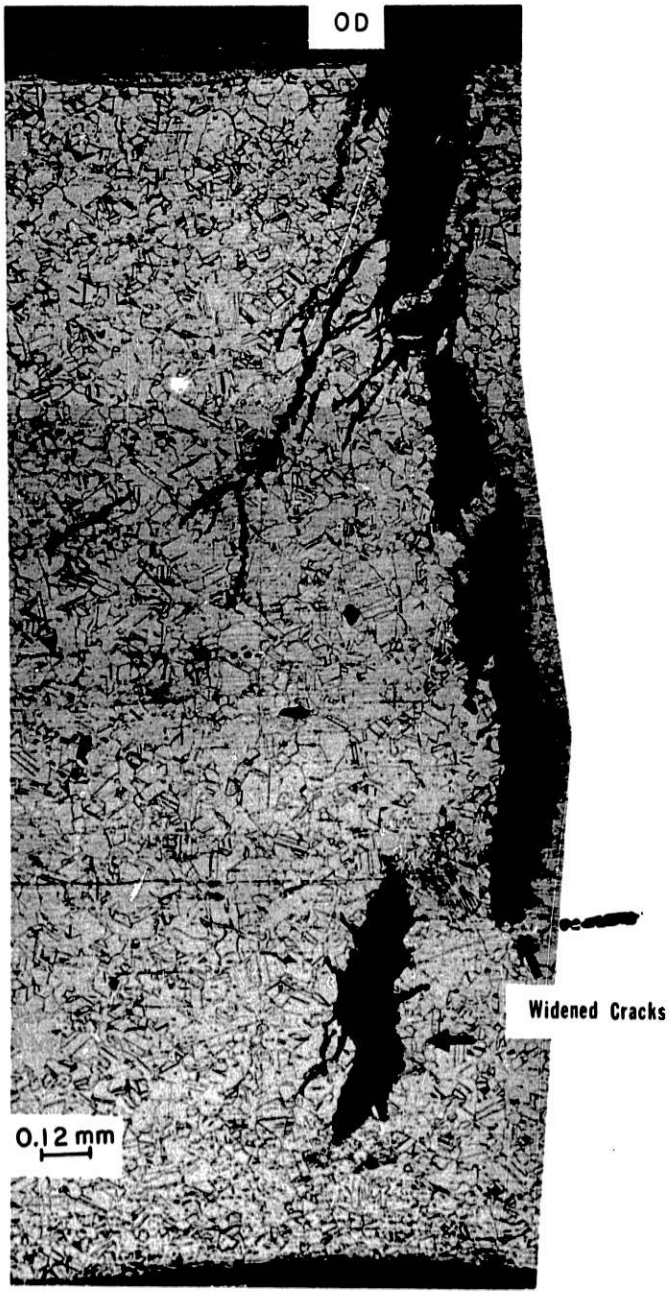

Fig. 48. Cross Section of 6411. Transgranular and branched cracks are visible. ANL Neg. No. 306-78-41.

REFERENCES

1. Materials Technology for Coal-conversion Processes Eleventh Quarterly Report, April-June, 1977, Argonne National Laboratory, ANL-77-62.

2. Materials Science Division Coal Technology Fifth Quarterly Report, October-December, 1975, Argonne National Laboratory, ANL-76-?2.

3. Materials Science Division Coal Technology Sixth Quarterly Report, January-March, 1976, Argonne National Laboratory, ANL-76-60.

4. Materials Science Division Coal Technology Seventh Quarterly Report, April-June, 1976, Argonne National Laboratory, ANL-76-111.

5. Materials Science Division Coal Technology Eighth Quarterly Report, July-September, 1976, Argonne National Laboratory, ANL-76-125.

6. Materials Science Division Coal Technology Ninth Quarterly Report, October-December, 1976, Argonne National Laboratory, ANL-77-5.

7. Private communication, DOE personnel at Synthane Pilot Plant, November 28, 1977.

8. Private communication, Phillips Petroleum personnel at Bi-Gas Pilot Plant, December 20, 1977.

9. J. J. Schuldies, "The Acoustic Emission Response of Mechanically Stressed Ceramics," Mater. Eval., XXXI(10), 209-213 (1973).

10. M. S. Crowley, Amoco Oil Research Center, private communication.

11. M. S. Crowley, "Initial Thermal Expansion Characteristics of Insulating Refractory Concretes," Am. Ceram. Bull, 25(12), 465-468 (1956).

12. "Study of Heat Transfer through Refractory Lined Gasifier Vessel Walls," Battelle-Columbus Quarterly Report for Period June-August 1977, ERDA Contract E(49-18)-2210.

13. "Improvement of the Mechanical Reliability of Monolithic Refractory Linings for Coal Gasification Process Vessels," Babcock and Wilcox Company Quarterly Report for Period October-December 1976, Contract E(49-18)-2218.

14. J. Selsing, "Internal Stresses in Ceramics," J. Am. Ceram. Soc., 44, 419 (1961).

15. A. G. Evans, "Residual Stress Measurement Using Acoustic Emission," J. Am. Ceram. Soc., 40(5-6), 239-243 (1975).

16. A. A. Pollock, "Acoustic Emission -- 2. Acoustic Emission Amplitudes," Nondestructive Testing 6(5), 223-286 (1973).

17. D. E. W. Stone and P. F. Dingwall, "Acoustic Emission Parameters and Their Interpretation," NDT International, April 1977, pp. 51-59.

18. M. J. Lighthill, "On Sound Generated Aerodynamically: General Theory," Proc. Roy. Soc. (London) A211, (1952) 564-587.

19. H. S. Ribner, "The Generation of Sound by Turbulent Jets," *Adv. in Applied Mechanics*, 8 (Academic Press, New York, 1964).

20. M. J. Lighthill, "Jet Noise," J. Am. Inst. of Aeronautics and Astronautics, 1, pp 1507-1517, 1963.

21. H. D. Baumann, "On the Prediction of Aerodynamically Created Sound Pressure Level of Control Valves," ASME Paper Wa/FE-28, 1970.

22. P. L. Jenvey, "Gas Pressure Reducing Valve Noise," J. Sound and Vibration, 41, 506-509 (1975).

23. D. J. Small, "Noise of High-pressure Gas Regulator Valves," Proc. 7th Intl. Conf. on Acoustics, Vol. 4, Academiai Kiado, Budapest, 1971.

24. A. H. Shapiro, *The Dynamics and Thermodynamics of Compressible Fluid Flow* Vol. I (Ronald Press, New York, [illegible]).

25. W. B. Hall and E. M. Orme, "Flow of a Compressible Fluid Through A Sudden Enlargement in a Pipe," Proc. of the Institution of Mech. Engineers, 169, 1007-1020 (1955).

26. Materials Science Division Coal Technology Tenth Quarterly Report, January-March, 1977, Argonne National Laboratory, ANL-77-41.

27. K. Natesan, Proceedings of the Conference on Prevention of Failures in Coal-conversion Systems, NBS Special Publication 468, 159 (1977).

28. K. Natesan and O. K. Chopra, Proceedings of Symposium on Properties of High Temperature Alloys, Z. A. Foroulis and F. S. Pettitt, eds., The Electrochemical Society, Princeton, NJ, 1976, p. 493.

29. W. C. Hagel, Trans. ASM, 56, 583 (1963).

30. E. A. Gulbransen and K. F. Andrew, J. Electrochem. Soc., 104, 334 (1957).

31. D. Kaplan, A. Harvey, and M. Cohen, J. Electrochem. Soc., 108, 134 (1961).

32. T. F. Kassner, L. C. Walters, and R. E. Grace, Thermodynamics, Vol. II, International Atomic Energy Agency, Vienna, 1966.

33. K. N. Strafford and A. F. Hampton, J. Less-Common Metals, 21, 305 (1970).

34. A. Davin and D. Coutsouradis, Cobalt, 17, 1 (1962).

35. T. Narita and K. Nishida, Oxidation of Metals, 6, 157 (1973).

36. K. Nishida, K. Nakayama, and T. Narita, Corrosion Science, 13, 759 (1973).

37. S. K. Verma, D. P. Whittle, and J. Stringer, Oxidation of Metals, 5, 169 (1972).

38. K. Ohta, T. Wada, K. Fuehi, and T. Mukaibo, Proceedings of the Fifth International Conference on Metallic Corrosion, Tokyo, Japan, 1972, p. 728.

39. Y. Jeannin, C. Mannerskantz, and F. D. Richardson, *Trans. Met. Soc. AIME*, 227, 300 (1963).

40. J. F. Elliott and M. Gleiser, *Thermochemistry for Steelmaking*, Vol. I (Addison-Wesley Publishing Company, Reading, PA, 1960).

41. G. C. Wood, T. Hodgkiess, and D. P. Whittle, Corrosion Science 6, 129 (1966).

42. G. C. Wood, I. G. Wright, T. Hodgkiess, and D. P. Whittle, Werkstoffe Korrosion, 21, 900 (1970).

43. C. Wagner, Z. Elektrochem., 63, 772 (1959).

44. R. A. Rapp, Corrosion, 21, 382 (1965).

45. K. Hauffe and A. Rahmel, Z. Physik. Chem. (leipzig), 199, 152 (1952).

46. S. Mrowec, T. Walec, and T. Werber, Oxidation of Metals, 1, 93 (1969).

47. Keys and Keyseats, USA Standard ANSI B17.1, ASME, New York, 1967.

48. R. E. Peterson, *Stress Concentration Factors* (John Wiley and Sons, New York, 1974).

Distribution of ANL-78-6

Internal:

E. G. Pewitt
R. G. Matlock
B. R. T. Frost
R. W. Weeks (6)
M. F. Adams
O. K. Chopra
S. Danyluk
D. R. Diercks
W. A. Ellingson (6)
J. Fischer
K. J. Reimann
C. A. Youngdahl
A. A. Jonke
T. F. Kassner
C. R. Kennedy
K. Natesan
J. L. Nivens
J. Y. Park
R. B. Poeppel
W. J. Shack
A. B. Krisciunas
ANL Contract Copy
ANL Libraries (5)
TIS Files (6)

External:

DOE-TIC, for distribution per UC-90c (276)
Manager, Chicago Operations Office
Chief, Chicago Patent Group
President, Argonne Universities Association
Materials Science Division Review Committee:
- G. S. Ansell, Rensselaer Polytechnic Inst.
- R. W. Balluffi, Cornell Univ.
- S. L. Cooper, Univ. Wisconsin
- S. Doniach, Stanford Univ.
- H. L. Falkenberry, Tennessee Valley Authority
- C. Laird, Univ. Pennsylvania
- D. Lazarus, Univ. Illinois
- M. T. Simnad, General Atomic
- A. R. C. Westwood, Martin Marietta Laboratories

R. R. Adams, Battelle Columbus Laboratories
E. M. Anderson, The Babcock & Wilcox Company
W. G. Bair, Inst. of Gas Technology
W. Bakker, USDOE/FE
S. Carson, CE Lummus Co., Bruceton, Pa.
A. Conn, Amoco Oil Co., Naperville, Ill.
W. C. Corder, Battelle Columbus Laboratories
M. Crowley, Standard Oil of Indiana, Naperville, Ill.
J. Flagg, Universal Oil Products Co., Des Plaines, Ill.
E. Fox, Stearns-Roger Corp., Homer City, Pa.
H. E. Frankel, USDOE/FE
S. M. Gaitonde, Commonwealth Edison Co., Maywood, Ill.
D. Glaser, Stearns-Roger Corp., Denver
H. Heysteck, Tuscaloosa Metallurgy Research Center, University, Ala.
V. Hill, IIT Research Inst.
D. Hull, Phillips Petroleum Co., Homer City, Pa.
R. I. Jaffee, Electric Power Research Institute
D. L. Keairns, Westinghouse Research Labs.
H. Leavenworth, Albany Metallurgy Research Center
A. V. Levey, Lawrence Berkeley Laboratory
R. Lewis Synthane Pilot Plant, USDOE/FE, Pittsburgh
G. Long, Northern Illinois Gas Co., Aurora
R. M. Lundberg, Commonwealth Edison Co., Chicago
J. M. O'Donnell, The Lummus Co., Bloomfield, N. J.
A. L. Plumley, Combustion Engineering Power Systems, Windsor

J. Pope, Science Applications, Inc.
F. A. Prange, Phillips Petroleum Corp. Bartlesville
A. Schaeffer, Metals Properties Council, New York
S. J. Schneider, National Bureau of Standards (2)
J. R. Schorr, Battelle Columbus Laboratories
J. Stevenson, Rolla Metallurgy Research Center
J. Sudbury, Consolidated Coal Co., Library, Pa.
C. Whitten, Peabody Coal Co., Columbia, Tenn.
F. Woods, Albany Metallurgy Research Center